

Technische Universität München
Fakultät für Physik
Max-Planck-Institut für Physik

Master's Thesis

Evaluation of Photomultiplier Tube Candidates for the CTA and Upgrade of the MAGIC LIDAR System

Dominik Martin Müller

Munich, 22nd January 2016

Supervisor: Prof. Dr. Elisa Resconi

Abstract

The Cherenkov Telescope Array (CTA) is planned as the next generation Imaging Atmospheric Cherenkov Telescope (IACT) for very high energy gamma ray astrophysics. CTA will cover an energy range from a few tens of GeV to above 100 TeV. The goal of this project is to achieve a ten times better sensitivity than current major IACTs.

An important component of IACTs is the camera system which currently uses Photomultiplier Tubes (PMTs) as standard light sensors. A dedicated development program with the companies Hamamatsu Photonics K.K. and ET Enterprises for new PMTs for the CTA project was started six years ago. Finally, Hamamatsu finished their development during this thesis and ET Enterprises is close to a final version. After several iterations, PMTs with exceptional good parameters became available.

During this Master's thesis important parameters like quantum efficiency of the photocathode, gain, pulse width, timing and afterpulse probability were measured. For this purpose, a low-noise setup sensitive for single photoelectrons (1ph.e) was optimized and the analysis software for the raw data was improved.

The second part of this Master's thesis is dedicated to upgrade the micro-power Light Detection and Ranging (LIDAR) system of the MAGIC (Major Atmospheric Gamma Ray Imaging Cherenkov) telescopes on La Palma. Since 2011 a single wavelength LIDAR system is operated alongside the observations of the MAGIC telescopes. It is used for real-time monitoring of the atmospheric transmission and for detecting cloud layers in the field of view of MAGIC. Light absorption and scattering losses in the atmosphere play an important role for IACTs and have a large influence on the data quality. The LIDAR observations are used to estimate the data quality of the MAGIC data and offer the possibility to correct energy spectra of data affected by adverse atmospheric conditions. The MAGIC telescopes LIDAR system uses a pulsed Nd:YAG laser with 532 nm wavelength and a pulse energy of 5 μ J as transmitter. The receiver is mounted to a 60 cm spherical single mirror telescope. To compensate for the low light intensities a sensitive detector with the capability of single photon detection as well as charge integration is needed. For this purpose, a hybrid photo diode is used in a custom designed detector module.

After five years of data taking the MAGIC LIDAR system has been upgraded with a new detector unit including a separate high voltage supply and new readout electronics during this thesis. Additionally, a stronger laser was tested for range extension. At the end of this thesis, the new hardware components were installed at the MAGIC site on La Palma and first test measurements have been started.

Zusammenfassung

Mit dem Cherenkov Telescope Array (CTA) beginnt eine neue Phase der Imaging Atmospheric Cherenkov Telescope (IACT) Technik für hochenergetische Gammastrahlung. Das CTA Projekt wird einen Energiebereich von einigen 10 GeV bis zu mehreren 100 TeV abdecken. Das Ziel des neuen Observatoriums ist eine Verbesserung der Sensitivität um einen Faktor zehn verglichen mit den aktuell im Betrieb befindlichen Teleskopen. Ein wichtiger Teil der IACT Technik ist das Kamerasystem der Teleskope, das in aktuellen Instrumenten aus Photomultipliern (PMTs) besteht.

Vor sechs Jahren wurde für das CTA Projekt ein spezielles Entwicklungsprogramm mit den Firmen Hamamatsu Photonics K.K. und ET Enterprises initiiert, um optimale PMTs für das Kamerasystem zu entwickeln. Im Laufe dieser Masterarbeit wurde die Entwicklung von Hamamatsu abgeschlossen und ET Enterprises ist kurz davor eine Endversion zu produzieren. Nach mehreren Entwicklungsschritten sind nun PMTs mit außergewöhnlich guten Eigenschaften verfügbar.

Im ersten Teil dieser Masterarbeit werden wichtige Eigenschaften wie Quanteneffizienz der Photokathode, Pulsbreite, Zeitauflösung und die Wahrscheinlichkeit von Nachpulsen (after-pulsing) untersucht. Zu diesem Zweck wurde ein rauscharmer Versuchsaufbau zur Messung einzelner Photoelektronen optimiert und die Software zur Analyse der Messdaten verbessert.

Der zweite Teil der Masterarbeit behandelt die Aufrüstung des Micro-Power-LIDAR (Light Detection and Ranging)-Systems der MAGIC (Major Atmospheric Gamma Ray Imaging Cherenkov) Teleskope auf La Palma. Seit 2011 wird ein LIDAR System parallel zu den Beobachtungen der MAGIC Teleskope betrieben. Es wird für eine Echtzeitüberwachung der Transmission der Erdatmosphäre und zur Erkennung von Wolkenschichten im Sichtfeld der MAGIC Teleskope verwendet. Lichtverluste auf Grund von Absorption und Streuung haben einen großen Einfluss auf die Datenqualität von IACT Systemen. Die LIDAR Messungen werden verwendet um die Qualität der MAGIC Daten zu beurteilen und bieten die Möglichkeit Energiespektren, die unter ungünstigen atmosphärischen Bedingungen aufgenommen wurden, zu korrigieren.

Das LIDAR System der MAGIC Teleskope nutzt einen Nd:YAG Laser mit einer Wellenlänge von 532 nm und einer Pulsenergie von 5 μ J als Lichtquelle. Der Detektor ist in einem Teleskop montiert, das mit einem einzelnen 60 cm großem sphärischem Spiegel ausgestattet ist. Um die geringe Lichtintensität auszugleichen, wird ein Detektor benötigt, der sowohl in der Lage ist einzelne Photonen zu zählen als auch größere Signale zu messen. Zu diesem Zweck wird eine Hybrid Photodiode in einem individuell gefertigtem Detektor verwendet. Nach fünf Jahren Betrieb wurde das MAGIC LIDAR System während dieser Masterarbeit mit einem neuen Detektor einschließlich einer separaten Hochspannungsversorgung und neuer Ausleseelektronik ausgestattet. Zusätzlich wird ein neuer Laser mit höherer Pulsenergie getestet um die Reichweite des LIDAR Systems zu verbessern. Am Ende dieser Arbeit wurden die neuen Komponenten am Standort der MAGIC Teleskope auf La Palma installiert und erste Testmessungen begonnen.

Contents

1. Introduction to Ground Based Gamma Ray Astronomy	1
1.1. Science with Very High Energy Gamma-rays	1
1.2. Cosmic Rays and Air Showers	4
1.3. Cherenkov Light	5
1.4. Imaging Air Cherenkov Telescopes	7
1.4.1. The MAGIC Telescopes	9
1.4.2. The Cherenkov Telescope Array	10
2. Evaluation of Photomultiplier Tubes	12
2.1. Working Principle of PMTs	13
2.2. Physical Effects and Basic Parameters	14
2.2.1. Photoelectric Effect and Quantum Efficiency	14
2.2.2. Secondary Electron Emission	16
2.2.3. PMT Noise Sources	16
2.2.4. CTA Requirements	17
2.3. Tested PMTs	18
2.4. Quantum Efficiency Measurement	19
2.4.1. Measurement Setup	19
2.4.2. Results	21
2.5. Single Photoelectron Measurement	23
2.5.1. Measurement Setup	23
2.5.2. Single Photoelectron Distribution and Gain Calculation	25
2.5.3. Excess Noise Factor	29
2.6. Pulse Width	31
2.7. Transit Time Spread	33
2.7.1. TTS Dependence on the Laser Intensity	34
2.7.2. TTS Dependence on the Illuminated Photocathode Area	36
2.8. Probability of Afterpulses	36
2.8.1. Cumulative Afterpulse Probability	37
2.8.2. Afterpulse Arrival Times	38
2.9. PMT Entrance Window Glow	41
2.10. Summary of the PMT Characterization	42
3. Upgrade of the LIDAR System for the MAGIC Telescopes	43
3.1. The LIDAR Technique and the Basic Equation	44
3.2. Characteristics of the Earth's Atmosphere	47
3.2.1. Atmospheric Attenuation of Light	49
3.2.2. Characteristics of the Atmosphere at the MAGIC Site	51

3.3.	The MAGIC telescope's LIDAR system	52
3.3.1.	LIDAR Mount and Telescope Frame	53
3.3.2.	LIDAR Detector Unit	54
3.3.3.	Data Readout and Analysis	55
3.4.	Goals of the LIDAR Upgrade	55
3.5.	Developing a new LIDAR Detector	56
3.5.1.	High Voltage Module	56
3.5.2.	Detector Optics	58
3.5.3.	Detector Module	60
3.5.4.	Transmitter Unit	63
3.5.5.	LIDAR Computer	66
3.5.6.	LIDAR Control Software and LabVIEW Programm	67
3.6.	Examining the Transmission of the Earth's Atmosphere	68
3.6.1.	Single Photoelectron Distribution	68
3.6.2.	LIDAR Detector Raw Data	69
3.6.3.	Typical LIDAR Return Signal	71
3.6.4.	Analyzing the Transmission of Clouds	72
4.	Conclusion and Outlook	75
A.	Appendix	77
A.1.	CCD Camera Calibration	77
A.2.	Source Code C++	79
A.2.1.	LIDAR Background	79
A.2.2.	High Voltage Control	85
A.2.3.	Voltage Monitoring	89
A.3.	Circuit Diagrams and Layouts	94
B.	Bibliography	97
C.	Acknowledgment	101

List of Figures

1.1. Differential Spectrum of Cosmic Rays	2
1.2. Crab Nebula	3
1.3. Extended Air Showers	5
1.4. Cherenkov Radiation	6
1.5. Imaging Air Cherenkov Telescope Technique	8
1.6. MAGIC Telescopes	9
1.7. Cherenkov Telescope Array	10
2.1. Different Applications of PMTs	12
2.2. Working Principle of a PMT	13
2.3. Photoeffect	15
2.4. Tested PMTs	18
2.5. Quantum Efficiency Measurement Device	20
2.6. QE measurement example	21
2.7. QE measurement results	22
2.8. Single photoelectron measurement	24
2.9. 1 ph.e background subtraction	26
2.10. Gain Versus Voltage Characteristic	28
2.11. Excess Noise Factor Versus Gain Results	30
2.12. Pulse Shape of a PMT Signal	31
2.13. Pulse Width Dependence on the Gain	32
2.14. Transit Time Spread Versus Gain	34
2.15. TTS Dependence on the Light Intensity	35
2.16. TTS Dependence on the Illuminated Photocathode Area	35
2.17. Mechanism for Afterpulsing	36
2.18. Cumulative Afterpulse Probability	37
2.19. Afterpulse Arrival Times	39
2.20. PMT glow measurement setup	41
2.21. PMT Entrance Window Glow	42
3.1. LIDAR Working Principle	44
3.2. Geometrical Factor of the LIDAR Equation	46
3.3. Characteristics of the Earth's atmosphere	48
3.4. Atmospheric Transmission	49
3.5. Rayleigh and Mie Scattering	50
3.6. Calima Weather Phenomenon	52
3.7. Drawing of the MAGIC Telescope's LIDAR System	53
3.8. Photograph of the LIDAR system at La Palma	54

List of Figures

3.9. LIDAR Geometry for Different Zenith Angles	56
3.10. Photograph of the HV Module	57
3.11. Signal Scheme of the SPI Protocol	58
3.12. Optical Path through the LIDAR Optics	59
3.13. Transmission Curve of the Interference Filter	60
3.14. Working Principle of a HPD	61
3.15. Photoelectron Resolution of HPD	62
3.16. LIDAR Detector Module	63
3.17. Transmitter Unit of the LIDAR System	64
3.18. Laser Beam Divergence	65
3.19. Laser Pulse Energy	66
3.20. LIDAR LabView Control Panel	68
3.21. 1ph.e Charge Distribution of the HPD	69
3.22. LIDAR Raw Data	70
3.23. Range Corrected LIDAR Return	71
3.24. Cloud Transmission	73

1. Introduction to Ground Based Gamma Ray Astronomy

Astronomy is one of the oldest sciences and dates back to ancient times when people observed the sky with bare eyes. However, the invention of the telescope was necessary before astronomy developed into a modern science. Since the middle of the 20th century, technical progress provided a variety of instruments which permitted an extension of the observations towards wavelengths invisible for the human eye. The wavelength bands are characterized by their energy, starting from the radio regime below some μeV , followed by infrared light ($O(0.1\text{ eV})$), the small band of visible light ($O(1\text{ eV})$), ultraviolet light ($O(10\text{ eV})$) and X-rays ($O(\text{keV})$). The spectrum finally ends with gamma radiation with energies above several 100 keV up to the PeV regime [1].

Beyond the electromagnetic radiation, Earth is exposed to a continuous flux of high energy particles from space. These so-called cosmic rays mainly consist of atomic nuclei and a small amount of electrons. They were first discovered by Victor Hess during his famous balloon experiment in 1912 by their ionizing nature. He discovered that the ionization rate increases with altitude and concluded that the ionizing radiation originates from space. At this time, he did not yet know that the ionization was caused by charged particles instead of electromagnetic radiation [2].

The differential spectrum of the cosmic ray flux is plotted in Fig. 1.1. It has two distinct features, the so-called knee at about $3 \cdot 10^{15}$ eV and the ankle at about $3 \cdot 10^{18}$ eV. Their origin is assumed to be due to changes in the production mechanism of cosmic rays and is still a topic of current research. The whole spectrum reaches from $3 \cdot 10^9$ eV up to $3 \cdot 10^{20}$ eV where it is supposed to show a cutoff. It is characterized by a broken power law $N(E) dE \sim E^\alpha dE$ with a spectral index α of -2.7 before the knee, about -3.0 between knee and ankle and again -2.7 for energies above 10^{18} eV [3].

At the beginning of this chapter the most important sources for gamma ray astrophysics are introduced. They are followed by Sec. 1.2, explaining the physics of air showers. Sec. 1.3 is dedicated to the production mechanism of Cherenkov light in air showers. Finally, the working principle of Imaging Air-shower Cherenkov telescopes is introduced in Sec. 1.4, including a brief introduction of the current MAGIC telescopes and the future Cherenkov Telescope Array project.

1.1. Science with Very High Energy Gamma-rays

Although gamma ray astronomy is still a quite young field of research, a multitude of interesting phenomena have been detected. Since the first gamma ray observation of the Crab Nebular by the Whipple Observatory in 1968, more than 130 sources have been detected. They can be roughly divided into two groups, galactic and extra galactic sources.

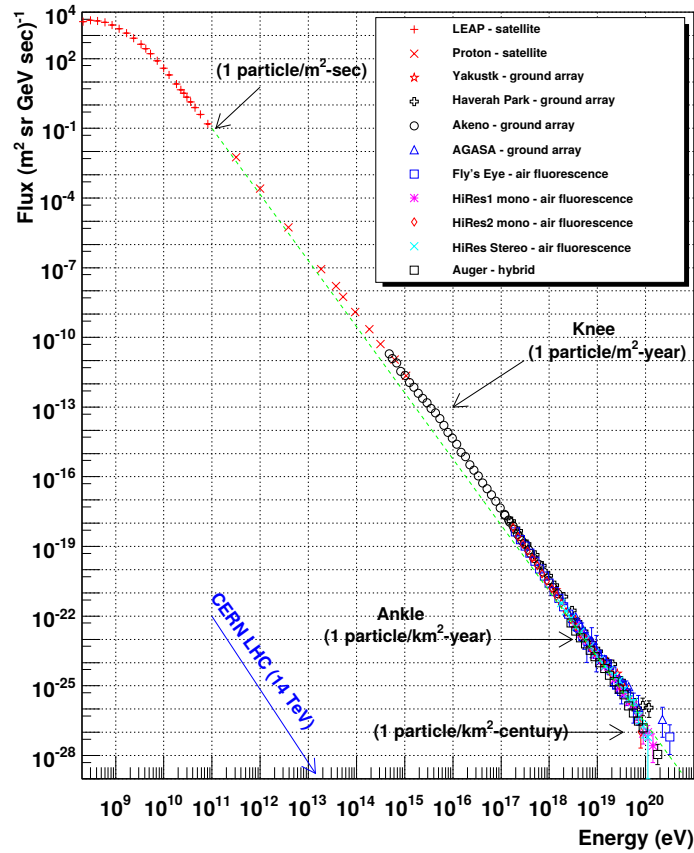


Figure 1.1.: Differential spectrum of cosmic rays measured with different instruments over twelve orders of magnitude in energy. The dashed green line indicates a power law with the spectral index of 2.7 which fits over a wide energy range. For comparison the maximum center of mass energy of the large hadron collider at CERN is marked (plot from [4]).

Galactic sources are located within our galaxy, the Milky Way. They are capable to produce gamma rays at very high energies.

Supernova Remnants (SNR) are results from massive star explosions. They consist of an expanding gaseous cloud interacting with the interstellar medium, which forms a shell like structure. The stellar material is accelerated to a speed greater than the speed of sound and causes a shock wave. The very high energy particles in the shock wave are thought to be the source of gamma ray production. One of the brightest SNRs is the Crab nebula depicted in Fig. 1.2. It is located in the Perseus Arm of the Milky Way and is used as a standard candle in gamma ray astronomy.

Pulsars consist of a fast spinning neutron star with a mass in the order of the solar mass and a radius of some ten kilometers. They are surrounded by very strong magnetic fields, which focus the emitted radiation. The radiation is only observable if the beam of emission points towards Earth. Hence, Earth based observations detect a pulsed signal

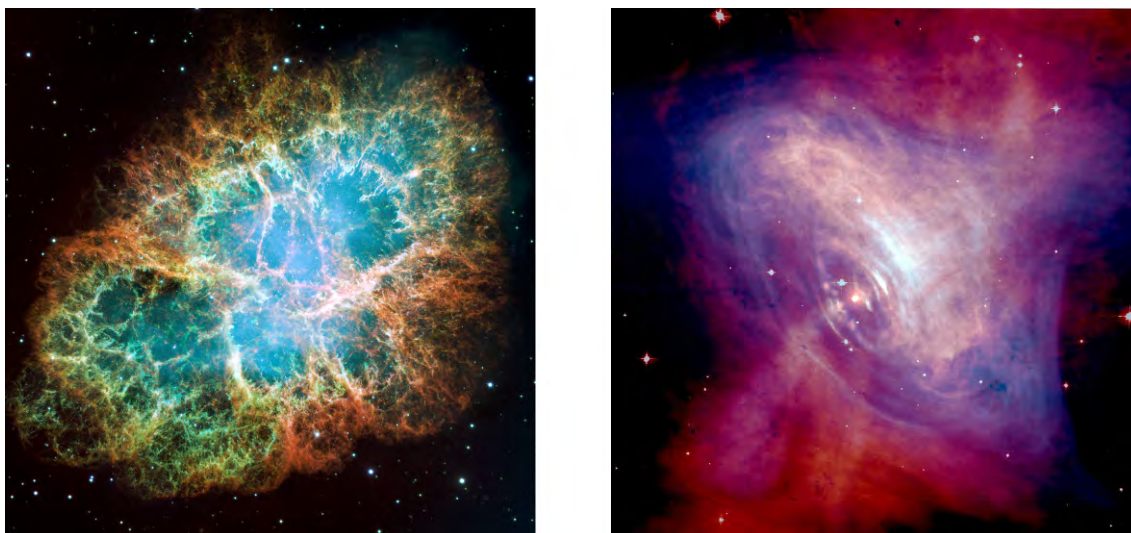


Figure 1.2.: Pictures of the Crab Nebula, one of the brightest supernova remnants located in the Perseus Arm of the Milky Way. It is the most important persistent calibration source for ground based gamma ray astronomy. The left picture shows the Crab Nebular in the optical regime observed by the Hubble Space Telescope. On the right, its center is shown as a combined optical (red) and X-ray image (blue). In the multi wavelength picture, the emanation from the Crab Pulsar in the center is becoming visible (images from [5] and [6]).

similar to the light of a lighthouse. The mechanism of gamma ray production in Pulsars is not completely understood, yet.

Pulsar Wind Nebula combine a SNR with a Pulsar in its center. The most famous one is again the Crab Nebula, which contains the Crab Pulsar in its center (see Fig. 1.2). In this configuration the pulsed emission from the pulsar can interact with the SNR gas and produce very high energy gamma rays.

Binaries are complex systems consisting of a compact object (e.g. neutron star) and a massive star rotating around each other. When both objects get close together, the compact object can accrete matter from the star. A complex particle accelerator is formed that can emit gamma rays.

Galactic Center is rich in massive stellar clusters and contains the nearest supermassive black hole as well as a variety of other objects emitting high-energy radiation including hypothetical dark-matter particles. It is one of the primary targets for the future Cherenkov Telescope Array.

Extragalactic sources are located far away from our galaxy. Thus, they have to be very bright to be observed from Earth.

Active Galactic Nuclei (AGN) are a class of galaxies that have a super massive black hole in their center. They are surrounded by an accretion disk of hot plasma which is

formed by matter falling into the black hole. Often AGNs are accompanied by collimated relativistic matter outflows, so called jets, which are perpendicular to the accretion disc. Most likely shock fronts in these jets accelerate particles to very high energies and cause radiation in the gamma ray band.

Gamma Ray Bursts (GRB) belong to the most energetic phenomena in the universe. It is assumed that a central object produces an ultrarelativistic outflow of plasma. GRBs occur randomly in the sky and have a short duration of milliseconds up to a few hundred seconds. So far, no gamma ray burst has been detected in the very high gamma ray band with ground based instruments. The Cherenkov Telescope Array is designed to provide a large discovery space for GRBs.

Starburst Galaxies are characterized by a high rate of star formation which is related to a high density of massive stars. Thus, also the number of super novae is high and the SNR density exceeds the average. These regions are expected to show a high photon emission in the gamma ray band.

1.2. Cosmic Rays and Air Showers

In the prior section we introduced several sources of cosmic rays and gamma rays. These particles can propagate through large areas of the cosmos without any interaction with other particles. The situation changes immediately as soon as they hit the Earth's atmosphere at a typical height between 20 km and 30 km above ground. During the first interaction with an air molecule they produce a pair of secondary particles and thereby initiate an air shower. The so-called daughter particles have still enough energy to produce particles by themselves. Thus, the process can repeat itself multiple times and initiate a cascade. The process is stopped either by the decrease of the particles energy or the particles hitting the ground. Such a cascade is called extensive air shower (EAS).

The high energy of the particles enables them to propagate through the Earth's atmosphere faster than the speed of light in the atmosphere. This causes a special light emission in the visible wavelength band called Cherenkov Light (for a more detailed explanation see Sec. 1.3). It is observed by ground based instruments.

Air showers are classified due to their electromagnetic or hadronic primary particle. They differ in their composition and profile. An initial gamma ray interacting with the atmosphere produces an electron-positron pair. The resulting electrons and positrons emit gamma rays due to Bremsstrahlung and initiate a cascade. The development stops when the particle energy is below a critical value. At this point the electrons mainly lose energy due to ionization. The typical shape of a simulated electromagnetic shower is depicted in Fig. 1.3 (a).

If the primary particle is a hadron, the situation is different. During the first interaction many high energy pions are created together with a small fraction of kaons, protons and nuclear fragments. The average transversal momentum is much higher compared to electromagnetic showers, causing a wider lateral distribution. Charged pions decay into muons and the corresponding neutrinos whereas neutral pions decay into two gammas and create an electromagnetic sub shower. An example for a hadronic air shower simulation of a proton is shown in Fig. 1.3 (b).

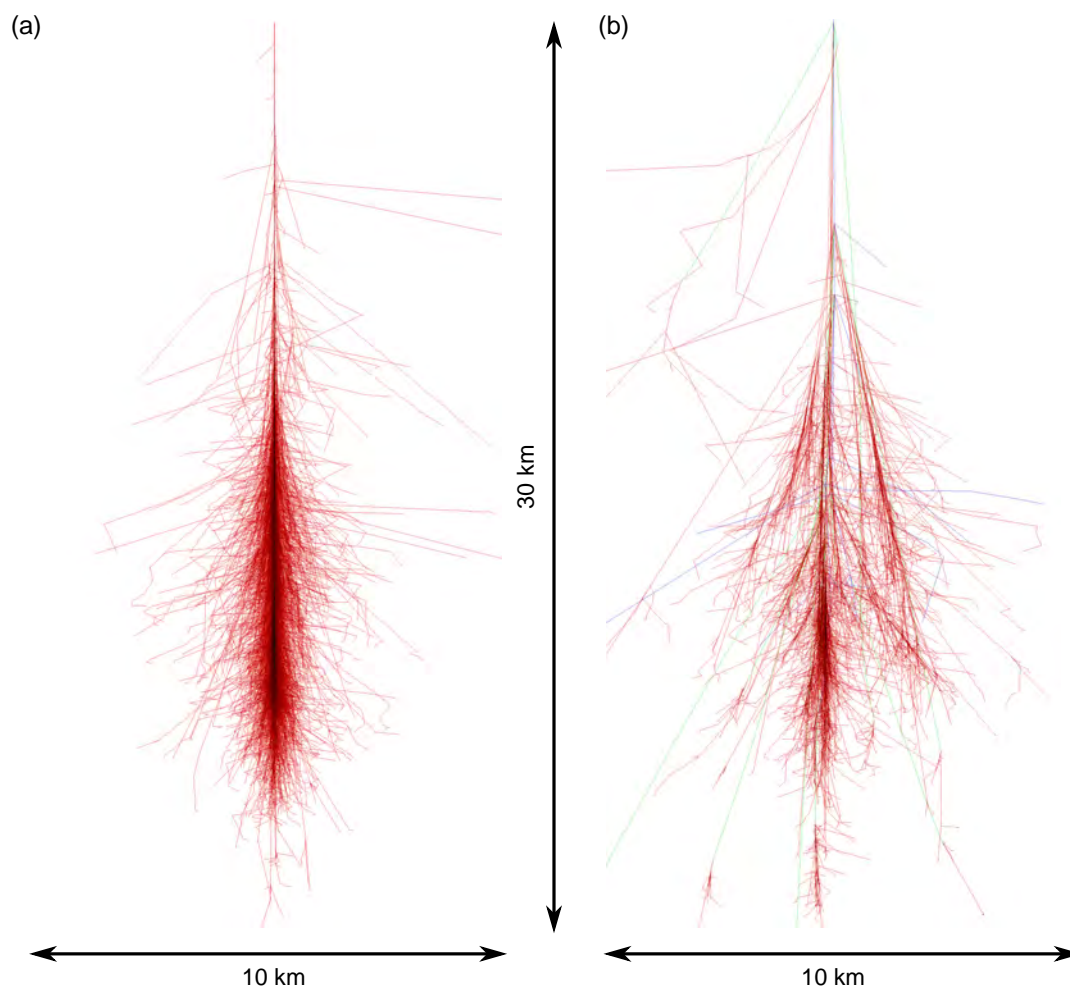


Figure 1.3.: Extended air shower simulations with CORSIKA. (a) Electromagnetic shower produced by a 10 GeV initial gamma ray. The shape is of a dense elliptical core. (b) Hadronic shower produced by a 100 GeV proton. The shape is more extensive compared to the electromagnetic shower. Hadronic interactions can transfer higher transverse momenta to their reaction products compared to electromagnetic processes. Thus, irregular sub showers occur and laterally expand the shower (simulation from [7]).

1.3. Cherenkov Light

Very high energy gamma rays do not reach Earth's surface directly as explained in the prior section. They interact with the atmosphere and create extensive air showers. The secondary particles of these shower still have huge energies and travel with ultra relativistic speed.

The speed of light in vacuum is a universal constant and an upper limit for every particle movement. In an optical medium the situation is different and light propagates with a

lower velocity. For a dielectric medium with a refractive index n the speed of light c_M reduces to:

$$c_M = \frac{c_0}{n} \quad (1.1)$$

with c_0 being the speed of light in vacuum. A charged particle produces an electric field polarizing the molecules in the medium. If the particle moves slower than the speed of light in the medium, the electrical dipoles align symmetrically along the axis of the particle movement. Hence, there is no overall dipole moment. The resulting dipole radiation causes spherical waves, which interfere destructively (see Fig. 1.4 (a)).

However, ultra relativistic particles can exceed the speed of light in a medium. In this case the dipoles can not align fast enough and the symmetry along the trajectory is broken. This results in a temporary dipole moment along the trajectory of the particle. After a short time the dipole moment will decay to equilibrium by emitting a spherical electrical wave. These waves can interfere constructively under a characteristic angle and produce light in the visible spectrum (see Fig. 1.4 (b)). This effect is referred to as Cherenkov radiation. It was discovered by the Russian physicist Pavel Alekseyevich Cherenkov in 1934. The production mechanism is limited by the transparency of the optical medium. In air and water for example mainly blue light is produced [8].

Cherenkov radiation is always emitted under a characteristic angle. When the charged particle propagates in the medium with the speed v_p above the speed of light in the medium,

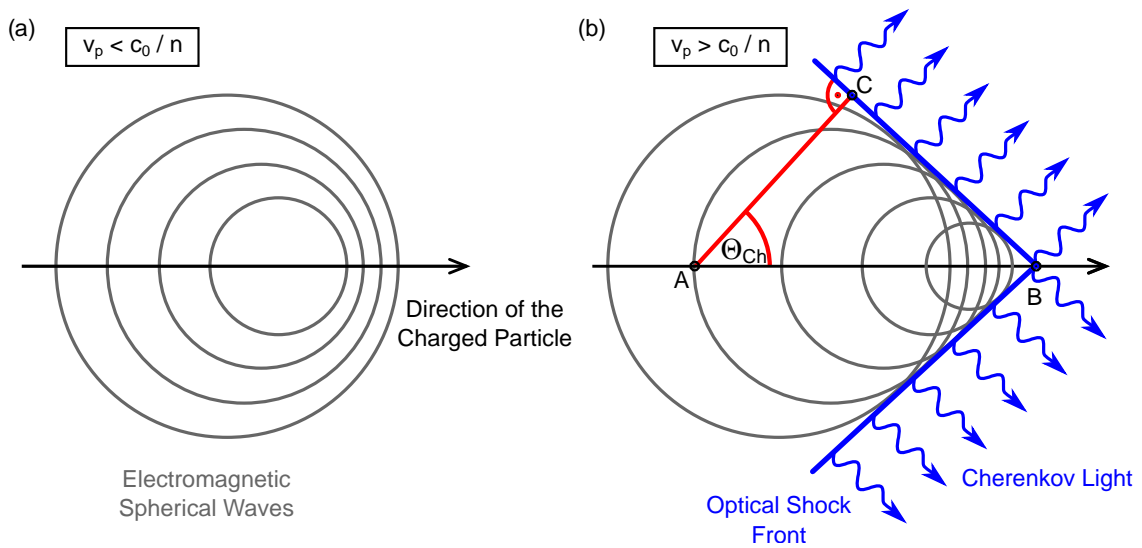


Figure 1.4.: Illustration of the Cherenkov light emission. (a) The charged particle moves slower than the speed of light in the medium. The resulting electromagnetic waves interfere destructively. No light emission is possible. (b) When the particle velocity exceeds the speed of light in the medium the electromagnetic fields interfere constructively and create a shock front. At the shock front, electromagnetic radiation in the optical blue band is emitted in a cone shape with a characteristic angle Θ_{Ch} . It is called Cherenkov light.

the following equation of motion is valid for the distance between the points A and B in Fig. 1.4 (b):

$$\overline{AB} = v_p \cdot \Delta t \quad c_M \leq v_p \leq v_0 \quad (1.2)$$

Similarly, we can set up the equation for the electromagnetic wavefront between the points A and C. In this case the waves propagate with the corresponding speed of light in matter:

$$\overline{AC} = \frac{c_0}{n} \cdot \Delta t \quad (1.3)$$

As depicted in Fig. 1.4 (b), the emission angle Θ_{Ch} is determined by both path lengths:

$$\cos(\Theta_{\text{Ch}}) = \frac{\overline{AC}}{\overline{AB}} = \frac{1}{n \cdot v_p / c_0} = \frac{1}{n \cdot \beta} \quad (1.4)$$

β is the ratio between the particle speed and the speed of light. In case of ultra relativistic particles $\beta \approx 1$ and the Cherenkov angle is only dependent on the refractive index.

1.4. Imaging Air Cherenkov Telescopes

Since cosmic rays and gamma rays are absorbed in the atmosphere they cannot be detected directly on Earth. Only satellite based experiments like the large area telescope (LAT) on board of the Fermi satellite mission or balloons can observe cosmic rays and gamma rays directly. Thus, on Earth a special technique was developed in the 1980s using the whole atmosphere as detector.

During the interaction of a cosmic particle with the Earth's atmosphere an extensive air shower is initiated. The relativistic charged secondary particles within the shower can emit Cherenkov light that reaches the ground. This light is observed with reflective telescopes called Imaging Air Cherenkov Telescopes (IACTs). Currently there are three major ground-based gamma ray observatories in operation which use the IACT technique: MAGIC (La Palma, Canary Islands, Spain), H.E.S.S. (Khomas Highland, Namibia) and VERITAS (Mount Hopkins, Arizona, USA).

The telescopes consist of a large reflector of several meters in diameter, focusing the Cherenkov light onto a camera. A typical IACT camera is of relatively low spatial resolution but has a high quantum efficiency and a good time resolution. The camera pixels of current IACTs are made of photomultiplier tubes. Several efforts are made to replace the photomultiplier tubes by silicon photomultipliers. This has been implemented for the FACT telescope (La Palma, Canary Islands, on the MAGIC site).

The operation principle of IACTs and the shower reconstruction is sketched in Fig. 1.5. For an introduction we constrain to a two telescope system like MAGIC, providing a stereoscopic view of the air shower. The shower image in each camera reflects the shape of the air shower. For gamma rays the image has an elliptical shape. Showers of hadronic origin show a more roundish shape due to their bigger lateral distribution. The distinct shape differences allow to distinguish between gamma and hadron events. This assures an efficient rejection of the hadronic background [9].

The image in the camera is a conformal projection of the shower shape. The main axis of the ellipse is pointing towards the shower axis. Using two telescopes in stereoscopic

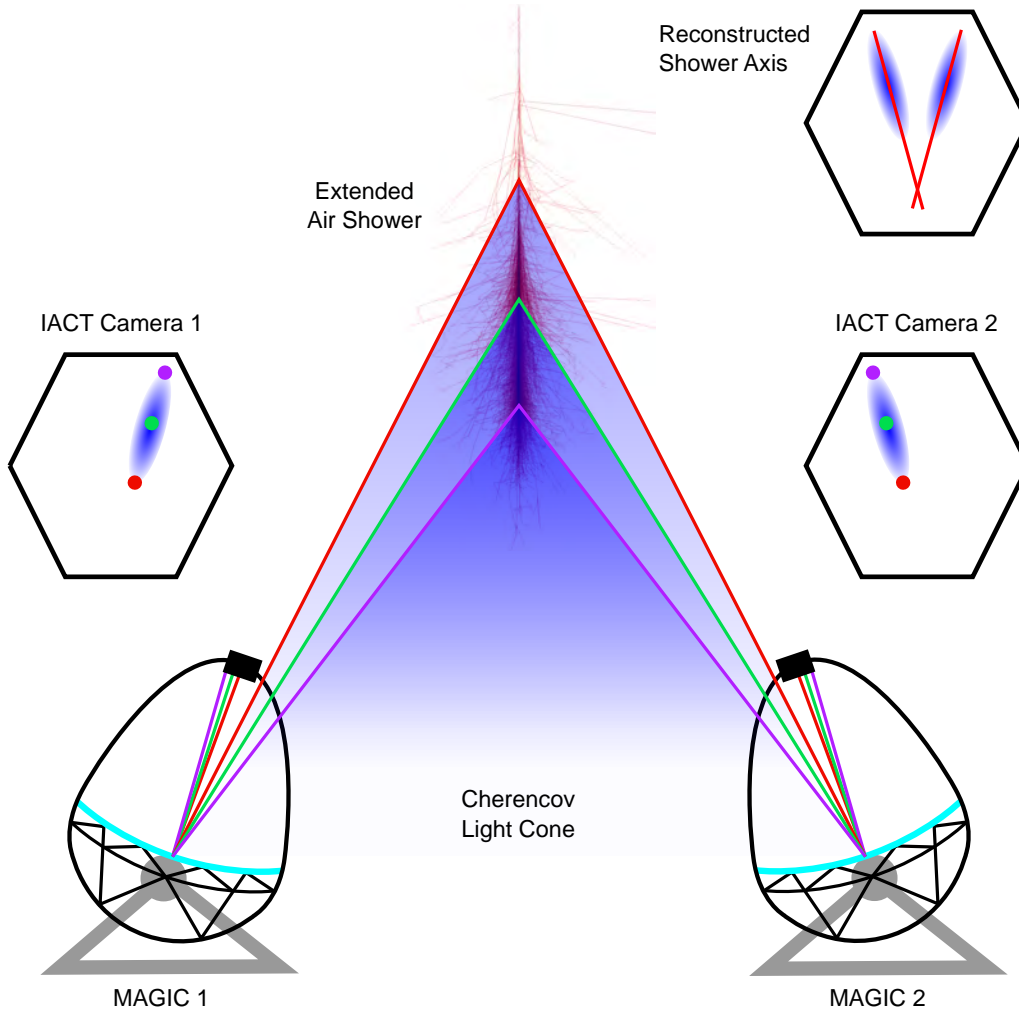


Figure 1.5.: Illustration of the operation principle of Imaging Air Cherenkov Telescopes in stereoscopic mode. The Cherenkov light of the air shower produces an elliptical image in the camera plane. Two images allow a three dimensional reconstruction of the shower axis.

mode allows to calculate a three dimensional image of the shower and to reconstruct the shower axis (see Fig. 1.5) as well as the height of the first interaction. Finally, it is possible to associate gamma rays with astrophysical objects in the sky and even to create full sky maps of extended sources.

The recorded light intensity of the image is proportional to the number of secondary particles in the shower and thus to the initial energy of the primary gamma ray. Typical IACTs cover an energy range between some 100 GeV up to several 100 TeV. This results in characteristic flux spectra of distinct astrophysical sources [9].

1.4.1. The MAGIC Telescopes

The MAGIC telescopes are two IACTs located on the Canary Island La Palma on the volcano Roque de los Muchachos at 2200 m above mean sea level. Construction of the first telescope finished in 2003. For stereoscopic observations a second telescope was built in 2009.

Both telescope structures are made of reinforced carbon fiber epoxy tubes. They were designed to be very stiff and light weight at the same time. Thus, a maximum slewing speed of $180^\circ/20\text{ s}$ is possible. This allows to react quickly on gamma ray burst alerts from the gamma ray coordinates network [11].

The telescopes are equipped with a parabolic segmented mirror dish of 17 m diameter and a focal length of 17 m. For the MAGIC2 telescope, in contrast to MAGIC1, the size of the mirror panels was increased from $0.5 \times 0.5\text{ m}^2$ to $1 \times 1\text{ m}^2$. Thereby, the number of mirrors was decreased from 964 panels in MAGIC1 to 247 in MAGIC2. The total mirror area of each telescope is around 247 m^2 . The mirror surfaces have a spherical shape. This conserves the time information of the optical signal in combination with the parabolic dish shape. The mirror panels are equipped with an active mirror control in order to correct small deformations from varying gravitational loads due to different pointing directions.

The cameras of the MAGIC telescopes consist of photomultiplier tube pixels. Since the camera upgrade in 2012, both cameras are equipped with 1039 photomultiplier tubes (PMTs) with a peak quantum efficiency around 32 %. On top of each PMT hexagonal light guides are installed to minimize the dead space between the pixels and to limit the field of view to the mirror dish. The pixels are grouped in 169 clusters to simplify mounting and exchange. Each cluster also contains electronics for high voltage control and signal



Figure 1.6.: Photograph of the two MAGIC Telescopes located on the Roque de los Muchachos on the Canary Island La Palma (image from [10]).

amplification [12].

Both MAGIC telescopes are operated and monitored from a counting house. There, the incoming data are continuously stored in a domino ring sampler. A trigger system decides on several levels if an air shower was detected. If an event passed all trigger levels, the data are digitized and stored on hard drive.

Currently, an additional test cluster equipped with 49 silicon photomultipliers (SiPMs) is attached to the camera edge. It is a first feasibility study and performance test for a possible MAGIC camera upgrade with SiPMs. The SiPM cluster is fully included into the MAGIC data taking and first samples were recorded successfully.

1.4.2. The Cherenkov Telescope Array

The Cherenkov Telescope Array (CTA) is the next generation IACT for very high energy ground based gamma ray physics. It was initialized by the MAGIC and H.E.S.S. collaborations as successor of their telescopes. In June 2015, the CTA consortium consists of more than 1200 members working in 200 institutes in 31 countries [14].

The science goals of CTA can be roughly grouped into three main topics. At first, the project wants to provide a better understanding of the origin of cosmic rays and their role in the universe. The second goal is to investigate the nature of particle acceleration especially around black holes. The third aim is the search for the nature of matter in the universe and physics beyond the standard model [15].

The observatory will consist of two arrays of IACTs one on the northern and one on the southern hemisphere to achieve a full sky coverage. The final site selection finished in July 2015. For the northern observatory a site on the Roque de los Muchachos on the Canary Islands next to the MAGIC telescopes was chosen. The southern array will be hosted on



Figure 1.7.: Design study of the Cherenkov Telescope Array. The core of the array will consist of four large size telescopes with a low energy threshold. They are supplemented by a large number of mid and small size telescopes to cover a large area and to increase the sensitivity (design study from [13]).

the European Southern Observatory Paranal grounds in Chile.

Each array will consist of several Cherenkov telescopes with different reflector sizes. The low energy instrumentation consists of four large size telescopes (LSTs) with a 24 m mirror dish to operate below energies of 60 GeV. A class of 12 m mid size telescopes (MSTs) will cover the medium range energies between 100 GeV up to 100 TeV. For the southern observatory, a large number of small size telescopes (SST) is planned to be spread over a huge area to detect showers above 10 TeV energies. Thus, CTA will be able to combine a low energy threshold with a ten times higher sensitivity than current instruments. Additionally, the large number of telescopes will provide an improved angular resolution compared to current instruments.

The overall performance of the instruments strongly depends on the photodetector performance. Each camera will consist of around 1000 to 2000 pixels. Together with the large number of telescopes, this results in a huge number of photomultiplier tubes. Thus, lots of effort was put into a development program for PMTs together with the companies Hamamatsu and ET Enterprises. In the first part of this thesis different PMTs are tested and characterized to obtain the best specifications for future CTA light sensors.

2. Evaluation of Photomultiplier Tubes

Photomultiplier Tubes (PMTs) are currently the most wide spread detectors for fast and faint light signals. They belong to the class of vacuum tubes using the photoelectric effect for light detection. The electrons produced by incoming photons are multiplied to a measurable electrical charge. PMTs are designed to detect light with very low intensities down to the level of single photons. They are sensitive for light in the ultraviolet, visible and near infrared spectrum. Their fast response, low noise and high gain results in a huge field of applications. In science PMTs are used from astroparticle physics, neutrino detection to nuclear physics as well as in chemistry, biology and medicine. Fig. 2.1 shows a variety of experiments base on detectors built of PMTs. Beyond science PMTs have several commercial applications, too. They are used for medical imaging as well as for radiation monitoring in combination with a scintillator crystal.

Currently the standard light sensors for IACTs are classical PMTs that are using a bialkali photocathode. A dedicated development program with the companies Hamamatsu Photonis K.K. (Japan) and Electron Tube Enterprises Ltd. (England) for novel PMTs for the CTA project was started about six years ago. As a result PMTs with outstanding good quantum efficiency, high photoelectron collection efficiency, short pulse width, very low afterpulse probability and low transit time spread became available. The goal of the following chapter is to present our measurement techniques and show the results of our PMT evaluation in order to provide basic data for future developments and decisions concerning the CTA camera system.

At the beginning of this chapter we will introduce the basic working principle of PMTs in Sec. 2.1. It is followed by Sec. 2.2 about the physical effects involved in the process of light detection including an overview of the requested parameters for the PMT candidates for the imaging cameras of the CTA telescopes. Finally, we introduce the sample PMTs

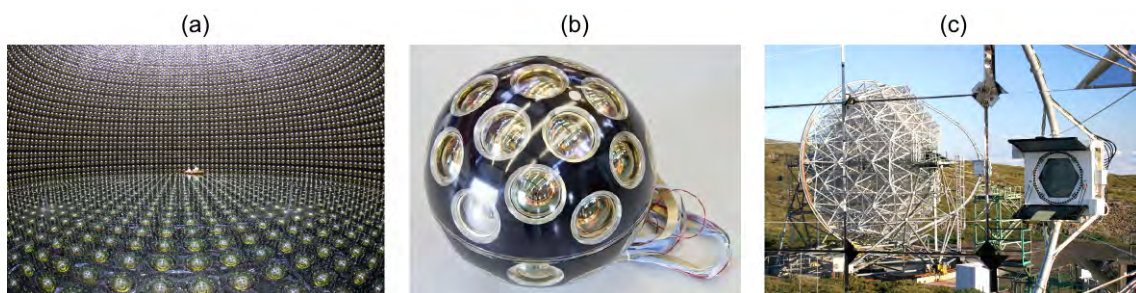


Figure 2.1.: Pictures of various PMT applications in science: (a) Neutrino observatory Super-Kamiokande in Japan (b) Digital optical test module of the KM3Net neutrino detector (c) PMT camera of the MAGIC telescope for gamma ray observations (pictures taken from [16], [17] and [18])

evaluated during this work in Sec. 2.3. The setup for the quantum efficiency measurement and the corresponding results are described in Sec. 2.4. Starting from Sec. 2.5 we introduce a special designed low noise setup for the precise evaluation of PMTs. It is followed by the detailed description of our evaluation of characteristic PMT parameters like gain, noise factor, pulse width, afterpulse probability and transit time spread which determine the performance of PMTs. In Sec. 2.9 we measure the entrance window glow using a ultra low noise CCD camera. At the end, we will summarize our results and show the final state of our evaluation.

2.1. Working Principle of PMTs

The prove of the working principle of PMTs dates in the year 1934. At that time, a typical PMT consisted of an evacuated galss housing containing a photocathode, a dynode and a collection anode. Incident photons release electrons from the photocathode via the photoelectric effect. The photoelectrons are accelerated towards the first dynode. At a sufficient high velocity the photoelectrons release a number of secondary electrons. This bunch of electrons is further amplified by a system of dynodes and collected on the anode where it causes a measurable electrical flux which is proportional to the number of initial photons [19].

In recent PMTs numerous additional components are introduced to increase the performance while the working principle stays the same. Fig. 2.2 shows a sketch of a PMT introducing the most important parts for an enhanced performance. PMTs still consist of a glass envelope with an entrance window at the front side and several pins at the back side. The incident light passes through the entrance window of the vacuum tube. The light is detected at the semi-transparent photo cathode which emits an electron by the photoelectric effect (see Sec. 2.2). To reduce backscattering there is an antireflection coating between the entrance window and the photocathode. The photoelectrons are electrostatically accelerated and

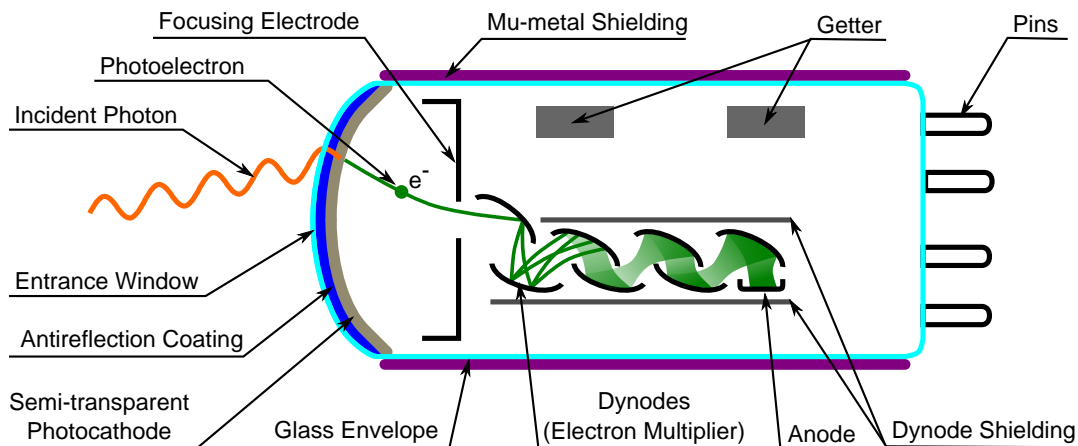


Figure 2.2.: Working Principle of a PMT. The scheme introduces the important components of a PMT. Furthermore, some additional components for noise reduction are shown.

guided to the first dynode by focusing electrodes. On the dynode the photoelectrons are multiplied by the means of secondary electron emission (see Sec. 2.2). The electron multiplier of a PMT consists of several dynodes, which repeat the process of secondary electron emission multiple times. The secondary electrons emitted from the last dynode are collected at the anode where they create a measurable electrical flux [20].

Latest PMTs are equipped with additional components in order to compensate for negative effects on the performance. The electron multiplier system is shielded with two metallic plates from the electric wires for the voltage supply. The side walls of the tube are coated with a so called Mu-metal shielding. This layer consists mainly of a nickel-iron soft magnetic alloy, which has a very high permeability. The goal of the Mu-metal layer is to shield the PMT against external magnetic fields, which influence the trajectories of the electrons and decrease the efficiency of the electron multiplication. To remove large atoms from the vacuum so called getters are installed in the PMT. They consist of a small crucible surrounded by a coil. After pumping the vacuum and closing the tube, the getters are heated via induction heating. Metal is evaporated onto the side walls of the tube and absorbs atoms of the residual gas via chemical bonding. This process increases the purity of the vacuum [21].

There are several additional techniques available to decrease the noise level and increase the time resolution. For example there are different dynode arrangements available to decrease the coupling to external electromagnetic noise. Furthermore, for increasing the the photon detection probability different entrance windows made from clear or mat glass are available, which can be additionally coated with antireflective layers [21].

2.2. Physical Effects and Basic Parameters

For a better understanding of the working principle this section will give an introduction into the photoelectric effect and the secondary electron emission. They are related to several parameters we evaluate in our measurements later in this thesis. In the third subsection characteristic noise sources of PMTs are introduced and finally, we give an overview over PMT specifications defined for the future CTA camera (adapted from [22]).

2.2.1. Photoelectric Effect and Quantum Efficiency

Light detection in PMTs is based on the photoelectric effect, which belongs to the processes describing light-matter interaction. In our case the external photoelectric effect is important which is also referred to in the literature as Hallwachs-Effect. It describes the emission of electrons from a material into the vacuum. Fig. 2.3 shows the electronic band structure of a typical alkali photocathode. In a semiconductor band model there is a band gap between the valance band and the conduction band that can not be occupied by electrons. The energy difference between the valence band energy E_V and the conduction band energy E_C is called band gap energy E_G . The energy difference between the conduction band and the vacuum level is called electron affinity E_{EA} . It describes the necessary energy to release an electron from the conduction band into the vacuum [22]. For an impinging photon with the energy $E_{h\nu}$ emitting a photoelectron the following energy balance equation is valid:

$$E_{h\nu} = E_G + E_{EA} + E_{Kin} \quad (2.1)$$

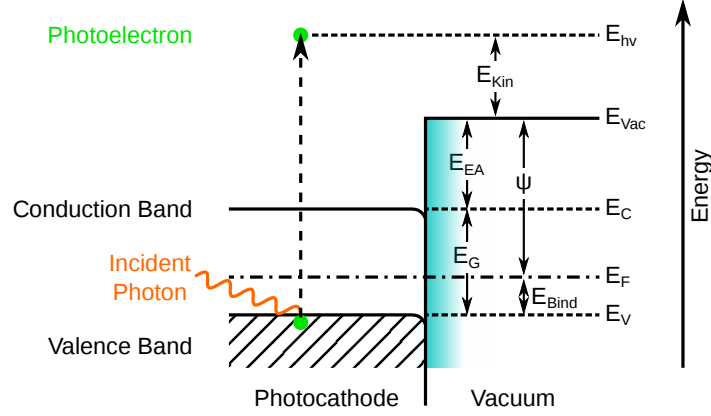


Figure 2.3.: Electronic band structure of an alkali photocathode and working principle of the photoelectric effect. An electron is ejected by a photon from the conduction band. If the incident photon has a sufficient high energy, the electron is emitted as a photoelectron to the vacuum.

In this equation E_{Kin} expresses the kinetic energy of the emitted electron. For PMTs the more common parameter to describe the thermodynamic energy to remove an electron from the photocathode to the vacuum is the work function. It is closely related to the electron affinity. The work function Φ refers to the energy difference between the Fermi level E_F and the vacuum. Now, the energy balance can be also written as:

$$E_{hv} = E_{Bind} + \Phi + E_{Kin} \quad (2.2)$$

Here, E_{Bind} is standing for the binding energy between the valence band and the Fermi level. The work function of a semiconductor can be easily changed by doping. Thereby, the sensitivity of the photocathode can be optimized. The sensitivity of the photocathode to different wavelengths is called quantum efficiency (QE). It is defined as the ratio between the number of released photoelectrons N_e and the number of incoming photons N_{photon} :

$$QE(\lambda) = \frac{N_e}{N_{photons}(\lambda)} \quad (2.3)$$

For the overall detection efficiency only electrons that produce a signal are of relevance. In order to produce a signal, the released photoelectron must hit the first dynode. The ratio between electrons reaching the first dynode $N_{e,dynode}$ and released photoelectrons is called collection efficiency (CE):

$$CE(\lambda) = \frac{N_{e,dynode}}{N_{photons}(\lambda)} \quad (2.4)$$

The collection efficiency is significantly increased by the introduction of special focusing electrodes (see Fig. 2.2). To optimize their performance dedicated simulations of electron trajectories are performed by the PMT manufacturers. The latest PMTs reach collection

efficiencies $\geq 95\%$ for wavelengths $\geq 400\text{ nm}$. The final photoelectron detection efficiency (PDE), which describes the sensitivity of the PMT for a characteristic wavelength range is composed of the quantum and collection efficiencies as follows:

$$\text{PDE}(\lambda) = \text{QE}(\lambda) \cdot \text{CE}(\lambda) \quad (2.5)$$

2.2.2. Secondary Electron Emission

Secondary electron emission is a physics phenomenon related to the interaction of electrons when hitting a surface. If a primary electron with an initial energy hits the surface of a dynode, it creates a bunch of secondary electrons. For a dynode system with n dynodes the secondary emission ratio δ_n is given by the fraction of the current produced from the n -th dynode I_n over the current of the previous dynode $I_{(n-1)}$. In total it is proportional to the interstage voltage U between the dynodes:

$$\delta_n = \frac{I_n}{I_{(n-1)}} \propto U^k \quad n \in \mathbb{N}, \quad I_0 = I_K \quad (2.6)$$

where k is determined by the material and design of the dynode and has typically a value between 0.7 and 0.8. In case of the first dynode, where $n = 1$, the initial current I_0 is produced from the photocathode and corresponds to the photocathode current I_K [21]. According to this equation, particles that are accelerated to higher energies by larger interstage voltages create a larger number of secondary electrons. For the operation of PMTs the electron emission from a single dynode is of minor interest. Instead, the total current measured at the anode I_A is an important parameter, which is given by the following equation:

$$I_A = I_K \cdot \underbrace{\text{CE}(\lambda) \cdot \delta_1 \cdot \delta_2 \cdot \dots \cdot \delta_n}_m \quad n \in \mathbb{N} \quad (2.7)$$

In this equation $\text{CE}(\lambda)$ is standing for the collection efficiency (see Eq. 2.4), δ_n is the secondary emission ratio of the n^{th} dynode and n the number of dynodes. Now, we can easily derive the current amplification of the photoelectrons produced at the photocathode, which is called gain m . Assuming a dynode system with equal interstage voltages, the secondary emission ratio is constant for all dynode stages. For this case, according to Eq. 2.6, the gain is proportional to the voltage:

$$m(U) = \text{CE}(\lambda) \cdot \delta^n \propto \text{CE}(\lambda) \cdot U^{kn} \quad (2.8)$$

Now it is quite obvious that the gain is proportional to the kn exponential power of the supply voltage of the dynodes. This motivates the gain versus voltage plots in double logarithmic scale presented in Sec. 2.5.2.

2.2.3. PMT Noise Sources

Besides the electronic noise which influences every measurement, PMTs themselves add additional noise to every measurement. This has a negative influence on the usage of PMTs in any detector system. The PMT noise is classified into two types.

The first kind of noise is caused by a small amount of current flowing in the tube even during operation in a completely dark environment. This current is called dark noise and has several different origins. A major contribution is coming from thermionic electron emission at the photocathode. The work function of the cathode material is designed to be very low. Thus, thermionic electron emission is possible even at room temperature. As PMTs are operated at high voltages small imperfections of the insulations also contribute to the dark noise. An additional contribution is coming from a small amount of ^{40}K contained in the glass envelope. It emits beta and gamma rays, which contribute to the dark current. The dark noise defines the lower limit for low-light-level detection [21].

The second type of noise is called afterpulsing. It occurs during the acceleration of electrons towards the first dynode. The electrons can ionize atoms and molecules in the residual gas or on the dynode surface. These ions fly back to the photocathode and create a second, time delayed pulse without any real incoming photon. This is an important effect directly influencing the threshold energy of IACTs. The different mechanism for afterpulsing and the corresponding measurements are explained in more detail in Sec. 2.8.

2.2.4. CTA Requirements

The CTA project requires PMTs with outstanding good characteristics to detect short Cherenkov light flashes in the order of a few ns. According to these requirements the specifications of the CTA photodetectors are defined. The main parameters are summarized in Tab. 2.1.

The most suitable detectors to fulfill these specifications with respect to the total costs are PMTs. Two companies joined a development program to manufacture PMTs according to these specifications. During this thesis we tested several prototype PMTs in order to evaluate their performance. We forwarded several measurement results to the companies ET Enterprises and Hamamatsu to help to improve their products.

Parameter	Specification
Photocathode Size	35 mm
Number of dynodes	7
Spectral Sensitivity Range	290 - 600 nm
Peak Quantum Efficiency	$\geq 35\%$
Collection Efficiency for $\lambda \geq 400$ nm	$\geq 95\%$
Average QE over Cherenkov Spectrum	$\geq 21\%$
Operational Gain	40 000
Pulse Width for 40 000 gain	≤ 3.0 ns
Transit Time Spread for 40 000 gain	≤ 1.5 ns
Afterpulse Probability for 4 ph.e threshold	$\leq 0.02\%$

Table 2.1.: PMT specification for the CTA camera system.

2.3. Tested PMTs

During this work we evaluated several types of PMTs from the companies Hamamatsu Photonis K.K. and ET Enterprises Ltd. All PMTs fulfill the size specifications. The external diameter is 38 mm and the photocathode area has a diameter of 35 mm. Also, the pin layout was adapted so that PMTs of both companies are interchangeable.

At the beginning of this work, Hamamatsu had just finished the development of their PMT candidate for CTA after several iterations. We tested three Hamamatsu prototype tubes of the version R-12992-100 (shown in Fig. 2.4 (a)) designed for the usage in the CTA camera. They use a 7 dynode electron multiplier to amplify the photoelectrons. The super-bialkali photocathode is designed to provide a quantum efficiency of 40%. This is supported by the introduction of a mat entrance window, which increases the mean free path length of the photon in the photocathode. Thus the probability for releasing a photoelectron increases. Additionally, a huge effort was made in order to decrease the afterpulse probability.

For our measurement we used the corresponding voltage divider provided by Hamamatsu. It uses a Zener diode in order to fix the cathode to first dynode voltage to 350 V. This stabilized first stage voltage is important to ensure a constant collection efficiency and single photoelectron distribution for a wide setting of bias voltages. It is necessary to vary the overall bias voltage in order to set all PMTs to a similar gain.

The PMTs from ET Enterprises are still under development during this thesis and represent the main object of investigation during this thesis. We started the evaluation with the 8 dynode PMT D569/3SA. It is based on a previous version and was modified with a new photocathode layer to reach higher quantum efficiencies. For the next iteration, the goal was to improve the time resolution in order to stick to the CTA specifications. Especially

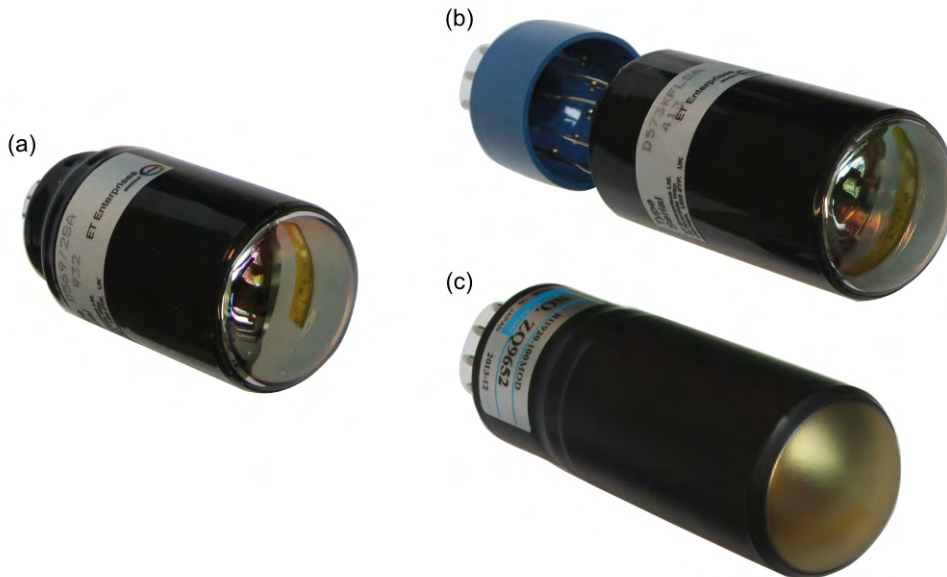


Figure 2.4.: Tested PMTs for the CTA camera. (a) ET Enterprises D569/3SA (b) ET Enterprises D573KFLSA (c) Hamamatsu R-12992-100

for low voltages corresponding to a gain of 40 000 the timing had to be improved. For this purpose, ET Enterprises decided to reduce the number of dynodes by one. As a result the 7 dynode PMT D573KFLSA was produced and showed the expected enhanced time resolution. Additionally, the pin layout was adapted to the Hamamatsu PMT layout, so both PMTs are easily interchangeable. Still, the afterpulse probability remained high compared to the Hamamatsu tubes.

To solve this issue a further version is under development. The goal for this iteration is to decrease the vacuum level in the tube and to improve the afterpulse probability. With the end of this thesis the development was not yet finished.

Manufacturer	Model Number	Serial-No.	# Dynodes	# Samples
Hamamatsu	R-129920-100	ZQ9652 ZQ9660 ZQ9662	7	3
ET Enterprises	D569/3SA	976 977 978 980 985 987	8	6
ET Enterprises	D573KFLSA	412 413	7	2

Table 2.2.: Table of all tested PMTs. The fourth column shows the number of dynodes in the electron multiplier chain. Column five shows the available number of samples for our measurements.

2.4. Quantum Efficiency Measurement

The quantum efficiency (QE) is a main parameter for PMTs, which determines the sensitivity of the sensor to a certain wavelength range. It defines the detection limit of faint light signals from air showers. The measurement is based on a light source with adjustable wavelength combined with a reference diode. The details of the measurement setup are explained in the following section. In the second part of this section we present our obtained results in QE curves.

2.4.1. Measurement Setup

All measurements are performed with a custom-made quantum efficiency measurement device (QEMD) [23]. A picture of the device with a corresponding block diagram is shown in Fig. 2.5. As light source, a hybrid halogen lamp hosting a deuterium and a tungsten lamp provides a spectral coverage from 180 nm to 2600 nm. Both lamps are attached to a spectrophotometer from Spectral Products including two different gratings. Spectral lines can be selected with a line width of 0.2 nm and an accuracy of 0.6 nm [24]. In order to remove second harmonics produced by the gratings a filter wheel is attached behind the spectrophotometer. The filter wheel includes four bandpass filters and changes the filter at 255 nm, 335 nm, 400 nm and 600 nm. The light is collimated onto the detector via an adjustable lens system. The detector under test is located in a dark box. We measure the

QE in reference to a calibrated PIN photodiode from Hamamatsu with a tabulated QE of 10 nm increments. The whole setup is controlled by a computer running a LabVIEW program.

Starting the measurement, the lamps have to warm up for approximately 20 min to reach a constant operating temperature in order to guarantee a stable light flux. Illuminating the PMT and the PIN photodiode with the wavelength range from 200 nm to 800 nm, we measure the output current of both sensors with a Keitley 6487 picoammeter [25]. For the QE measurement we record the current of the PMT between the photocathode and the first dynode, which is set to -300 V. All other dynodes as well as the focusing electrodes are shorted with the first dynode to avoid space charge effects. The output currents of both detectors are proportional to the QE and the light flux $L(\lambda)$:

$$I_{\text{Diode}}(\lambda) \propto \text{QE}_{\text{Diode}}(\lambda) \cdot L(\lambda) \quad (2.9)$$

$$I_{\text{PMT}}(\lambda) \propto \text{QE}_{\text{PMT}}(\lambda) \cdot L(\lambda) \quad (2.10)$$

Assuming a constant light flux $L(\lambda)$ we can calculate the QE of the PMT by comparing

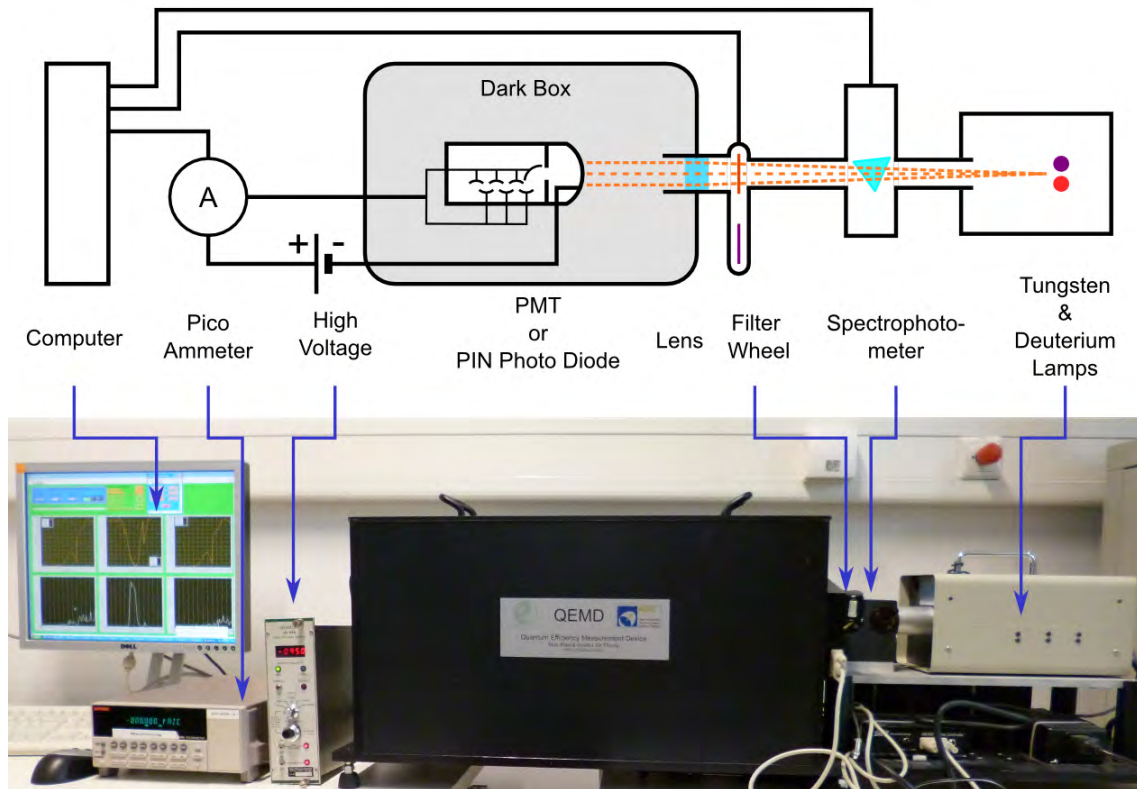


Figure 2.5.: Quantum Efficiency Measurement Device. Top: block diagram of the measurement setup introducing the components. Bottom: photograph of the setup in the laboratory.

the cathode current (Eq. 2.9) with the one of the reference PIN diode (Eq. 2.10):

$$QE_{\text{PMT}}(\lambda) = \frac{I_{\text{PMT}}(\lambda)}{I_{\text{Diode}}(\lambda)} \cdot QE_{\text{Diode}}(\lambda) \quad (2.11)$$

2.4.2. Results

All tested PMTs run through a QE evaluation in order to characterize their sensitivity. In Fig. 2.6 we show a typical result of a QE measurement. In the wavelength range between 200 nm and 400 nm the current measured on the PIN diode is very small, in the order of some pA. In this region the deuterium lamp is used as light source and produces a much smaller light flux compared to the tungsten lamp. The tungsten lamp covers the wavelength range beginning from about 350 nm and emits a much stronger light intensity. The current measured on the PIN diode is much higher in this range and peaks at 600 μA at 750 nm. The huge current range does not introduce large systematics in the measurement because the PIN diode has a working range in the order of eight magnitudes of current. Small jumps in the current at 260 nm, 340 nm, 400 nm and 600 nm can be explained by the change of filters. They become clearly visible after the calculation of the QE shown in Fig. 2.6 (b). They are artifacts introduced by the measurement setup and do not represent the real behavior of the QE. For the further analysis of the QE these peaks due to filter changes are removed from the QE curve.

The results of the QE measurements of all tested PMTs are shown in Fig. 2.7. In this plot the lines correspond to the average QE of the tested PMTs. The shaded area around shows the spread of the measurement among the number of tested samples. The Hamamatsu R12992-100 PMTs showed the best performance among the samples. They reach a peak QE of $(38.7 \pm 0.4)\%$ at a wavelength of 390 nm. The good performance is related to the combination of a mat entrance window and a super-bialkali photocathode. The QE curve of the Hamamatsu tubes shows an additional nice behavior at shorter wavelengths. Between

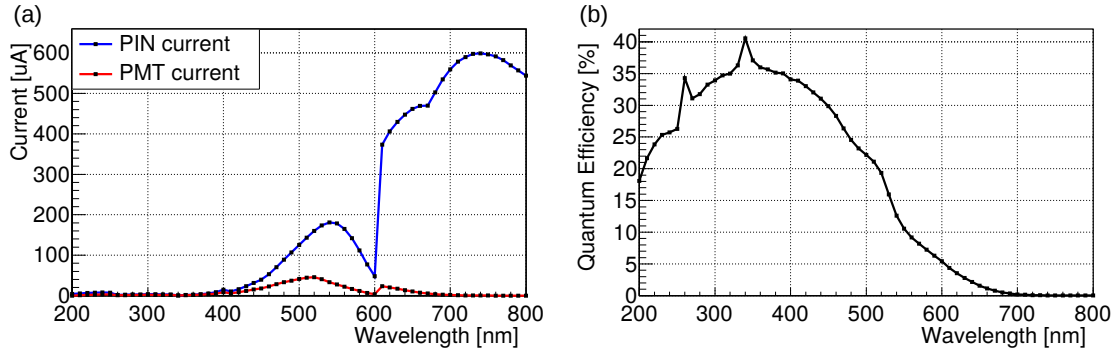


Figure 2.6.: Example results of a QE measurement performed with the ET Enterprises PMT D573KFLSA 412. (a) Current measurement on the PIN diode and the PMT with identical light intensities. The visible dips at 400 nm and 600 nm are due to filter changes. (b) Calculated QE curve for the photocathode sensitivity. The peaks at 260 nm and 340 nm are again caused by filters and are removed for further evaluation of the QE.

240 nm and 300 nm, there is a quite sharp cutoff visible. In comparison with the Cherenkov spectrum this is favorable to avoid noise from ultraviolet light. The ET Enterprises PMTs D569/3SA and D573KFLSA have the same photocathode design and material. The peak QE is $(34.2 \pm 1.7) \%$ and $(32.9 \pm 1.5) \%$ respectively at 390 nm. ET Enterprises is planning to improve the QE by introducing an antireflection coating between the entrance window and the photocathode. Thereby, they expect to increase the QE towards the same level as Hamamatsu avoiding to produce a mat entrance window.

Besides the peak QE there is another value which is even more important for the performance, the mean QE weighted with the Cherenkov spectrum $\Omega_{\text{Cherenkov}}$:

$$QE_{\text{mean}} = \frac{\sum_{\lambda} (QE(\lambda) \cdot \Omega_{\text{Cherenkov}}(\lambda))}{\sum_{\lambda} \Omega_{\text{Cherenkov}}(\lambda)} \quad (2.12)$$

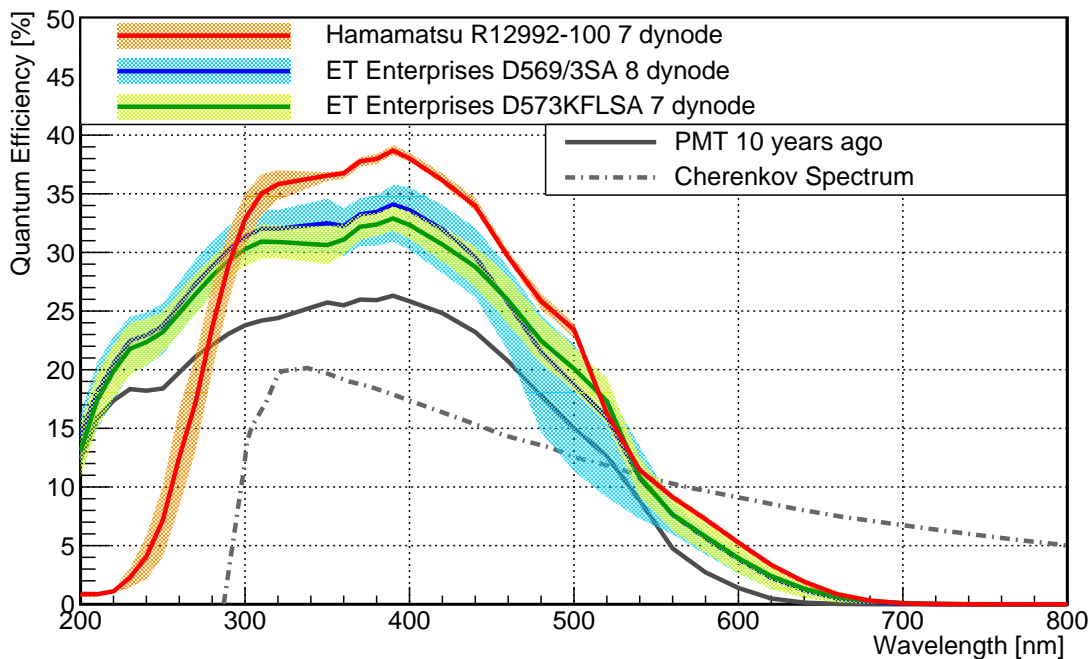


Figure 2.7.: The plot shows the QE of all measured PMTs for the wavelength range from 200 nm to 800 nm. The lines correspond to the average QE of the tested PMTs. The shaded area around indicates the spread of the measurement among the different tested samples. 10 years ago, bialkali PMTs showed a peak QE of approximately 25%. The latest generation of super-bialkali PMTs have been improved to reach a peak QE above 40%. The red curve shows the result of the final Hamamatsu PMTs. They show a sharp cutoff between 240 nm and 300 nm in order to decrease noise from ultraviolet light. The green and blue line show the QE of the ET Enterprises PMTs, which will be improved for the final version. The bottom dashed line is the Cherenkov spectrum of a 100 GeV γ -ray after absorption in the atmosphere, displayed as reference for the required sensitivity range.

For our calculation, the Cherenkov spectrum produced by a 100 GeV gamma ray coming from direct zenith direction is used. Additionally, it is assumed that the Cherenkov light is absorbed in the Earth's atmosphere and the detector is placed at a height of 2200 m above mean sea level. The corresponding spectrum is depicted in Fig. 2.7 as gray dashed line. In Tab. 2.3 we summarize the obtained results from the QE measurement showing the type of PMT, the corresponding peak QE as well as the mean QE convolved with the Cherenkov spectrum. Concerning the CTA requirements, the Hamamatsu PMTs fulfill all requested QE specifications. The current ET Enterprises D573KFLSA PMTs are slightly below the requested peak QE specification. This issue will be solved for the final version. Anyhow, they fulfill the requirements for the convolved mean QE.

PMT Type	QE _{peak} @ wavelength	QE _{mean}
R-129920-100	(38.7 ± 0.4) % @ 390 nm	(24.7 ± 0.4) %
D569/3SA	(34.2 ± 1.7) % @ 390 nm	(21.8 ± 1.2) %
D573KFLSA	(32.9 ± 1.5) % @ 390 nm	(21.3 ± 1.8) %

Table 2.3.: Results of the QE measurement. Column two shows the peak QE of the recorded curves and the corresponding wavelength. The third column shows the mean QE after convolution with the Cherenkov spectrum produced by a 100 GeV gamma ray from direct zenith direction.

2.5. Single Photoelectron Measurement

Sensitivity to single photoelectrons (1ph.e) is a real advantage for the evaluation of PMTs. This section is dedicated to a special low-noise setup designed for this purpose. The measurement of single photons is related to several important parameters for the PMT performance like gain, noise factor, pulse width and transit time spread discussed later in this thesis. At the beginning of this section the components of the measurement setup are introduced. It is followed by a theoretical discussion of the 1ph.e distribution leading to the calculation of the PMT gain. Finally, this section concludes with the evaluation of the noise factor of the tested PMTs.

2.5.1. Measurement Setup

The high sensitivity of PMTs requires a special low-noise setup which reduces pickup noise. A circuit diagram is shown in Fig. 2.8. The setup is placed in a Faraday cage of the type MPE Limited C 821 I Thomas to minimize electronic noise from the surrounding. Readout, trigger and laser are placed outside the Faraday cage to separate them from the signal production. The laser light is fed into the dark box inside the Faraday cage by an optical fiber. A picture of the setup introducing all components is depicted in Fig. 2.8.

The PMT is fixed in a copper tube of 2 mm wall thickness to shield the dynode system against electromagnetic noise. The detector under test is illuminated by a laser (PicoQuant PDL 800-D) with a pulse width of about 50 ps and a wavelength of 405 nm [26]. The laser light is fed into a 100 m long optical fiber, producing a time delay of 500 ns to separate the laser flash from the pickup noise of its own power supply [27].

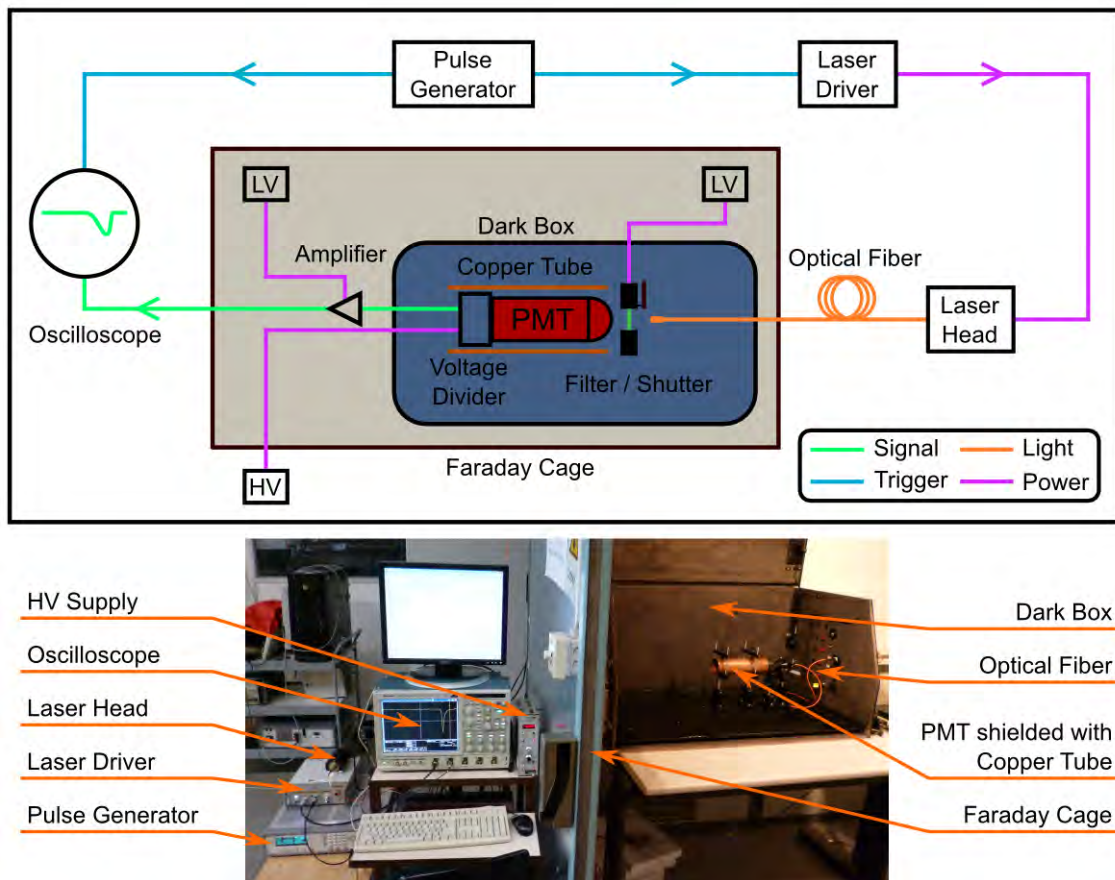


Figure 2.8.: Single photoelectron measurement setup. Top: Circuit diagram of the setup introducing all main components and the signal propagation. Bottom: Photograph of the setup showing the instrumentation in the laboratory and the open dark box in the Faraday cage.

The measurement requires to take data with and without light. At the beginning, the laser was switched on and off for this purpose. This caused small instabilities in the light flux compromising the measurement. To reduce this influence, a motorized filter flipper MFF102 from Thorlabs was mounted after the optical fiber output during this work. It consists of two filter mounts. For the purpose of light absorption, mount one is equipped with an absorptive neutral density filter (Thorlabs NE60B-A) with broad band antireflection coating for the wavelength range between 350 nm and 700 nm. The goal of the filter is to stop the light beam without switching off the laser. The transmission at 405 nm is less than 0.0001 % [28].

Additionally, we recognized that the cable coating of the optical fiber (Thorlabs FT030) is not completely light tight. Therefore, additional photons from the ambient light can enter the optical fiber and influence the measurement. It is necessary to remove these photons because they spoil the measurement. For this purpose, the second mount is equipped with a 10 nm bandpass filter with 405 nm central wavelength (Edmund Industrial Optics

#65-678).

The motorized filter flipper is delivered with a commercial power supply. After the first test runs, we recognized that this power supply causes quite a lot of high frequency noise. To solve this issue, it was replaced by a stabilized triple power supply from Systron Donner TL8-3 Series, which provides a stable DC power without influencing our measurement. The filter position can be changed by a switch from outside the Faraday cage.

The light flash hitting the photocathode of the PMT produces a signal in the range of a few ns. It is amplified by a fast amplifier of the type Femto HSA-Y-2-40 which provides a gain of 100. The amplifier is also delivered with a commercial power supply which is again replaced by a power supply from Systron Donner TL8-3 Series to decrease noise.

The amplified signal is measured by a fast oscilloscope with 2.5 GHz bandwidth and 40 GS/s sampling rate from Tektronix DPO 7254C Series. In order to create coincidence, we use a pulse generator (Agilent 81110A 165/330MHz) which triggers the laser and the oscilloscope simultaneously.

2.5.2. Single Photoelectron Distribution and Gain Calculation

For the single photoelectron measurement, the light intensity of the laser is set to a very low level. In this regime the photon flux follows a Poisson distribution:

$$P_{\lambda}(k) = \frac{\lambda^k}{k!} \cdot e^{-\lambda} \quad k \in \mathbb{N}, \quad \lambda \in [0, 1] \quad (2.13)$$

k is the number of photons and λ the average laser intensity. In order to avoid the detection of multiple photons we have to set a laser intensity as low as possible. With our laser we can reduce the intensity towards the order of 0.1ph.e per pulse. This corresponds to a probability of single photons of $P_{0.1}(1) = 9.0\%$. It is also possible to calculate the contribution of multiple photon pulses:

$$P_{0.1}(\geq 2) = 1 - P_{0.1}(0) - P_{0.1}(1) = 1 - 1.1e^{0.1} \leq 0.5\% \quad (2.14)$$

As a result, the contribution of two or more photon flashes can be neglected. On the other hand, the low light intensity leads to a high probability for pedestal events of $P_{0.1}(0) = 90.5\%$ where no photon is detected at all. Hence, we have to acquire a large number of shots in order to record a significant number of single photon events. For our setup the number of events is limited by the internal buffer of the oscilloscope which can record a maximum of 153942 shots. The oscilloscope screenshot in Fig. 2.9 (a) shows a typical single photon pulse of a PMT and the corresponding trigger.

For each shot we calculate the charge of the pulse by integrating the signal in a predefined window of 10 ns. For an estimated signal width of 3.0 ns FWHM, the integration window contains more than 99% of the charge produced by the PMT. Additionally, we use a region without signal as reference to remove a possible offset from the signal. As a result we obtain a charge histogram with a huge pedestal peak and a small 1ph.e peak depicted in Fig. 2.9 (c).

To receive a 1ph.e distribution, the pedestal events have to be removed. This can be done statistically by subtracting two charge histograms, one with signal and one without signal. However, a simple bin by bin subtraction leads to unphysical negative bins and does not

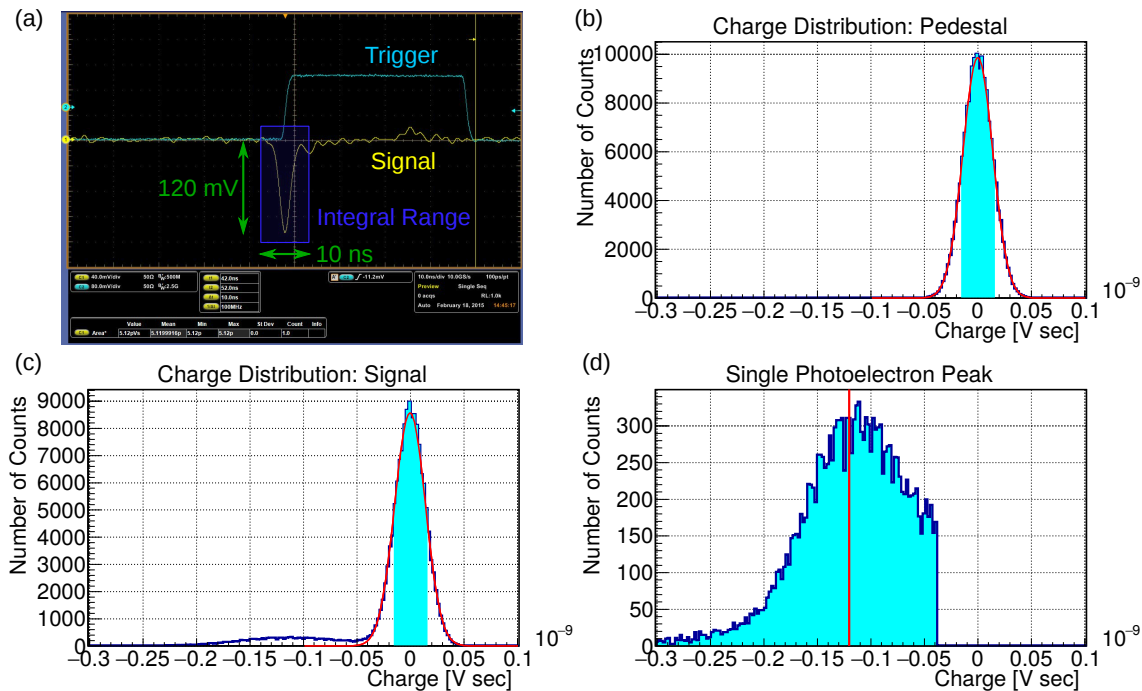


Figure 2.9.: Single photoelectron measurement result. (a) Screenshot of the oscilloscope with the trigger and the PMT signal introducing the integration window for the charge calculation. (b) Pedestal histogram without light for subtraction of the 0ph.e peak. (c) Charge histogram acquired with very low laser intensity. The 0ph.e peak in the origin is much larger than the peak due to 1ph.e. (d) Final result of the measurement after pedestal subtraction: charge distribution of the 1ph.e peak. The red line indicates the calculated mean charge.

consider shifts of the charge distribution. Therefore, a dedicated subtraction method is implemented in the data analysis for this thesis. To remove the 0ph.e peak we construct a function which is used for a background rejection using a five sigma subtraction criterion [29]. In the following we will give a short insight into this process. At the beginning, a Gaussian function is fit to the 0ph.e peak in both histograms with and without signal (see Fig. 2.9 (b) and (c)):

$$fit_i(C) = a_i \cdot \exp^{-0.5 \cdot \left(\frac{C-C_i}{\sigma_i}\right)^2} \quad i \in \{ped, sig\} \quad (2.15)$$

where C is the ph.e charge. Both histogram contain the same total number of events. Thereby, the 0ph.e peak in the pedestal histogram is roughly 10% higher compared to the signal histogram. To compensate this effect, we introduce a scaling factor α . It is defined via the ratio of events N in the signal and pedestal histograms within the $\pm 1 \sigma_{ped}$ range

(marked as blueish area in Fig. 2.9 (b) and (c)):

$$\alpha = \frac{N_{sig,0ph.e}}{N_{ped,0ph.e}} = \frac{\sum_{-\sigma_{ped}}^{-\sigma_{ped}} N_{sig}(C)}{\sum_{-\sigma_{ped}}^{-\sigma_{ped}} N_{ped}(C)} \quad (2.16)$$

Now we have all parameters to define a scaled subtraction function at the position of the 0ph.e peak in the signal histogram:

$$\text{sub}(C) = \alpha \cdot a_{ped} \cdot \exp^{-0.5 \cdot \left(\frac{C - C_{sig}}{\sigma_{ped}} \right)^2} \quad (2.17)$$

For the subtraction of the 0ph.e peak we define the following subtraction criterion in order to distinguish between 0ph.e events and 1ph.e. events:

$$N_{sig}(C) - \text{sub}(C) \geq n \cdot \sigma = n \cdot \sqrt{N_{sig}(C) + \text{sub}(C)} \quad n \in \mathbb{N} \quad (2.18)$$

For our evaluation we choose $n = 5$. This guarantees that only one out of one million 1ph.e events is due to no photon detection. This results in the following selection criterion for real 1ph.e events:

$$N_{\text{signal}}(C) - \text{sub}(C) \geq 5 \cdot \sigma \quad (2.19)$$

$$\Rightarrow N_{\text{result}}(C) = N_{\text{signal}}(C) - \text{sub}(C) \quad (2.20)$$

$$N_{\text{signal}}(C) - \text{sub}(C) \leq 5 \cdot \sigma \quad (2.21)$$

$$\Rightarrow N_{\text{result}}(C) = 0 \quad (2.22)$$

Finally, we obtain the charge distribution of the 1ph.e peak shown in Fig. 2.9 (d) with a sharp cut off on the right side. The width of the distribution is due to fluctuations, which are caused by two effects. First, the secondary electron emission on the dynodes can produce different numbers of electrons, which causes a certain variation of the detected charge. Second, inelastic backscattered electrons have less energy and deliver a smaller amount of charge to the anode [30]. For further calculations we determine the mean charge of the 1ph.e distribution:

$$\bar{Q}_{1ph.e} = \frac{\sum_{C_{min}}^{C_{max}} N_{\text{result}}(C) \cdot C}{\sum_{C_{min}}^{C_{max}} N_{\text{result}}(C)} \quad (2.23)$$

At the end, we calculate the gain of the PMT deriving Ohm's law:

$$\text{gain}_{\text{PMT}} = \frac{U \cdot t}{R \cdot e \cdot N_{\text{amp}}} = \frac{\bar{Q}_{1ph.e}}{R \cdot e \cdot N_{\text{amp}}} \quad (2.24)$$

U is the voltage, t the integration time, R the resistance of the oscilloscope which is set to 50Ω , N_{amp} is the gain of the amplifier which is 100 and e the elementary charge.

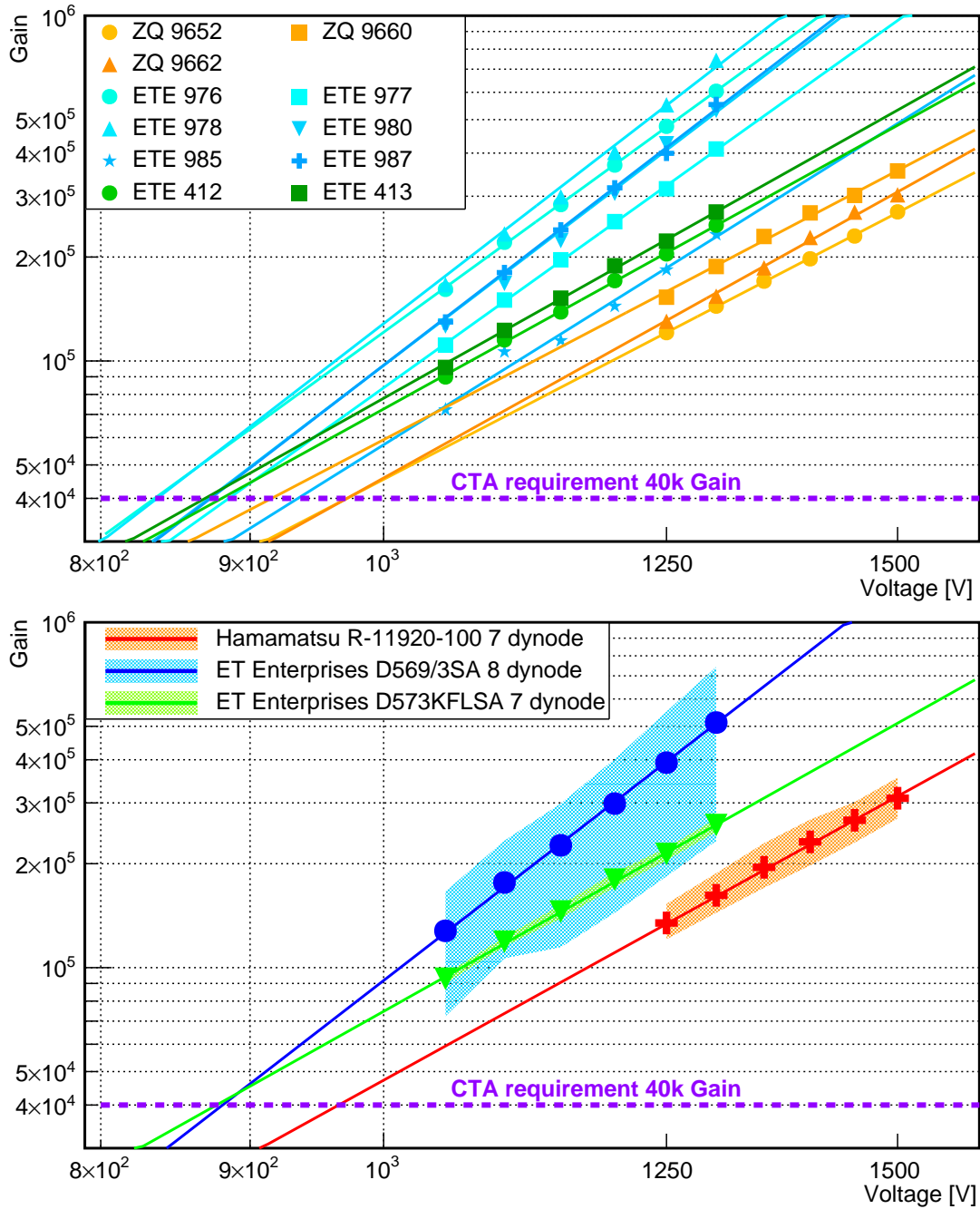


Figure 2.10.: Gain versus voltage characteristic with double logarithmic scale. Top: Individual measurements of all tested PMTs. The ET Enterprises PMTs are measured starting from a voltage of 1050 V. The Hamamatsu PMTs need a higher voltage of 1250 V in order to reach a comparable gain. Bottom: For a better readability, we calculate the mean value for each PMT type. The mean values are fitted with a power law in order to calculate the voltage corresponding to a gain of 40 000.

To calculate a proper gain voltage characteristic we record 1ph.e distributions every incremental 50 V. The voltage range of the measurement is dependent on the manufacturer. For the ET Enterprises PMTs we start the measurement at 1050 V. The Hamamatsu PMTs are measured beginning from 1250 V. We need to set these high voltages in order to guarantee a high electron multiplication through the dynode system. Otherwise the output signal of the PMT is too small to be detected. The results are depicted in Fig. 2.10 with a double logarithmic scale. To provide a better readability we compute the average values for each PMT type and show the spread of the measurement in shaded areas (see Fig. 2.10). One can see that reducing the number of dynodes from 8 in ETE D569/3SA to 7 in ETE D573KFLSA results in a lower gain for equal voltages. Additionally, it is visible that the gain versus voltage characteristic for the 7 dynode tubes ETE D573KFLSA and Hamamatsu R-129920-100 show a similar slope of the fitted power law. Only for the voltage offset, a difference of about 70 V occurs which is due to a different design of the first dynode stage of both PMTs.

In the CTA camera all PMTs are operated with an equal gain of 40 000. This low gain was selected to reduce the effect of aging for the detectors. In the camera system the PMTs will be operated under the presence of a steady background illumination from the light of night sky. Using Eq. 2.8 we can calculate the required voltage for the dynode system to provide this gain. For the tested PMTs the voltage to provide 40 000 gain varies between 836 V to 978 V. The results are gathered in Tab. 2.4.

PMT Type	Average Voltage for 40 000 Gain [V]
R-129920-100	958 ± 29
D569/3SA	885 ± 42
D573KFLSA	877 ± 6

Table 2.4.: Average voltage to provide a PMT gain of 40 000. The ET Enterprises PMTs need 70 V lower voltage compared to the Hamamatsu tubes.

2.5.3. Excess Noise Factor

A second parameter that can be derived from the 1ph.e charge distribution is the excess noise factor or short F-Factor. It describes the degradation of the signal-to-noise ratio (SNR) caused by the components of the PMT. In theory it is defined as the ration of the SNR of the light source (before) and the SNR of the PMT signal (after) [31]:

$$F = \frac{SNR_{\text{after}}}{SNR_{\text{before}}} \quad (2.25)$$

For a practical determination of the F-Factor in our measurement we use a dedicated 1ph.e data analysis method based on the following formula:

$$F = \sqrt{1 - \frac{\text{var}(Q_{1ph.e})}{\bar{Q}_{1ph.e}^2}} \quad (2.26)$$

where $\text{Var}(Q_{1ph.e})$ is the variance of the 1ph.e charge distribution and $\bar{Q}_{1ph.e}$ is the corresponding mean charge determined in Eq. 2.23. One can see that the noise factor is

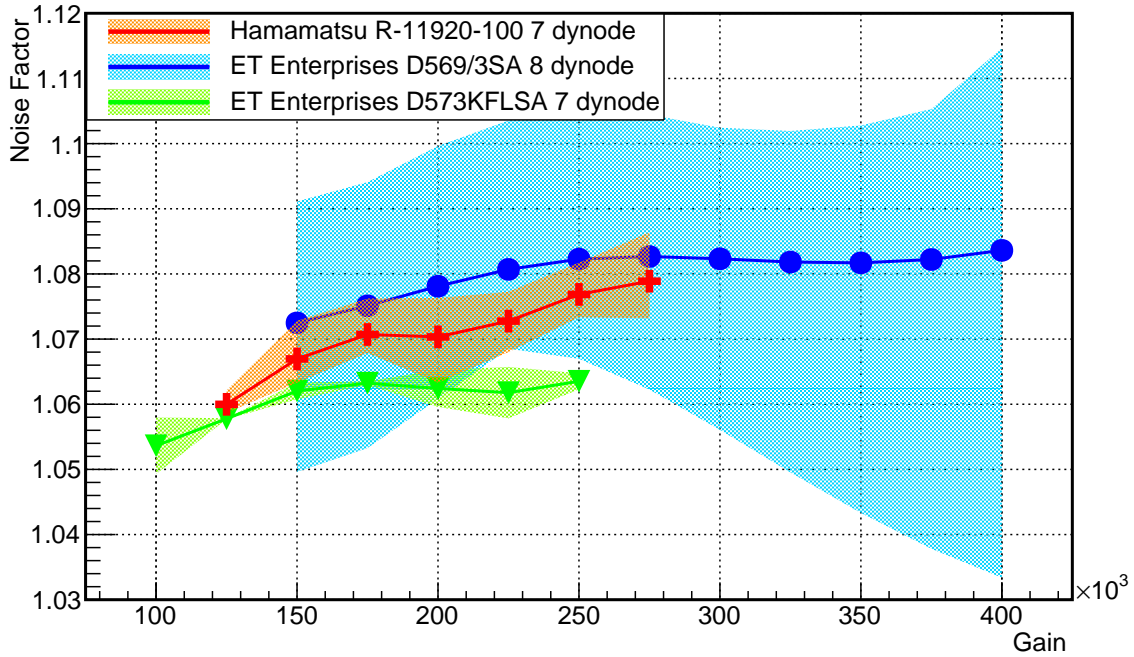


Figure 2.11.: Result of the excess noise measurement. It is an important specification for the additional noise due to electron multiplication added to the measurement by the PMT. In general, all tested PMTs show an extraordinary good noise performance below 1.11. Changing to a 7 dynode PMT ET Enterprises reduced the internal PMT noise to an average of 1.06.

related to the relative width of the charge distribution which is called pulse amplitude resolution. Therefore, the excess noise factor of the PMT is a measure for the decrease of its amplitude resolution. The amplitude resolution is mainly influenced by the electron multiplication process in the dynode chain. A larger number of dynodes increases the width of the distribution.

This effect is also visible in our measurement data depicted in Fig. 2.11. The reduction from 8 to 7 dynodes between ETE D569/3SA and ETE D573KFLSA leads to a corresponding decrease of the noise factor. All tested PMTs show an exceptional good noise performance around an average noise factor of 1.07. The detailed results are summarized in Tab. 2.5.

PMT Type	Average F-factor
R-129920-100	1.07 ± 0.01
D569/3SA	1.08 ± 0.02
D573KFLSA	1.06 ± 0.01

Table 2.5.: Results of the excess noise measurement. All tested PMTs show an extraordinary good noise performance concerning the SNR before and after the PMT, on average below 1.08.

2.6. Pulse Width

The pulse width of PMTs is a critical parameter concerning the time resolution of the future CTA camera. Following the CTA specifications the pulse width has to be less than 3.0 ns for an operational gain of 40 000. We evaluate the pulse width as FWHM (Full Width Half Maximum) of the initial PMT pulse. The measurement setup is similar to the 1ph.e setup described in Sec. 2.5.1. For the pulse width analysis, we set a higher laser intensity of 10ph.e. The increased light flux results in a higher signal rate and larger signal amplitude of the pulses without influencing the pulse width. We measure the pulse width every incremental 50 V, starting from a voltage corresponding to a gain of roughly 20 000. The FWHM is calculated after fitting a Gaussian function to the signal. We only take signals into account which have a charge between 80 % and 120 % of the expected 10ph.e charge to assure a proper intensity selection. Afterwards, we convert the voltage dependence into the corresponding gain using the fit parameters of the power law obtained from the 1ph.e measurement in Sec.2.5.2. A typical PMT signal of our measurement is shown in Fig. 2.12. Right after the PMT pulse up to 40 ns some additional ringing is visible, which is caused by the amplifier. The amplitude is about a factor of ten smaller than the initial signal, so it has no influence on our measurement. The dependence of



Figure 2.12.: Typical pulse shape of a Hamamatsu PMT at -1000 V supply voltage and the light intensity level set to 10ph.e. The screenshot of the oscilloscope shows the overlap of 13258 acquisitions. It is visible that the time jitter of the signal is very small. Due to a negative voltage applied to the cathode the signal has a negative sign. The second peak right behind the signal is an artifact caused by the input impedance of the amplifier and the cabling. Also the positive peak 30 ns behind the signal is due to some ringing of the amplifier.

the pulse width on the gain is shown in Fig. 2.13. The pulse width follows a $1/\sqrt{U}$ law which can be converted into a gain dependence. A higher applied voltage U produces a higher gain which corresponds to a smaller pulse width. Also, a smaller number of dynodes reduces the pulse width as the measurement results of the PMT series ETE D569/3SA and ETE D573KFLSA indicate. Both ET Enterprises PMTs fulfill the CTA requirement. The company managed to reduce the pulse width for a gain of 40 000 by 4 ns when switching to a 7 dynode PMT design. This is an expected result. The electron multiplier of our PMTs consist of identically constructed dynodes. We can assume that the contribution to the pulse width of each dynode is similar. For the ETE D569/3SA PMT we calculate a broadening of the pulse per dynode of approximately 0.5 ns. This rough estimate fits quite well to the measured value of 0.4 ns.

The Hamamatsu PMTs show a pulse width slightly above the requirements, around 3.2 ns. This might be due to the limited set of three tested samples for our measurements. For a larger set of samples the Hamamatsu PMTs are supposed to match with the CTA specifications. The important values for a gain of 40 000 are collected in Tab. 2.6.

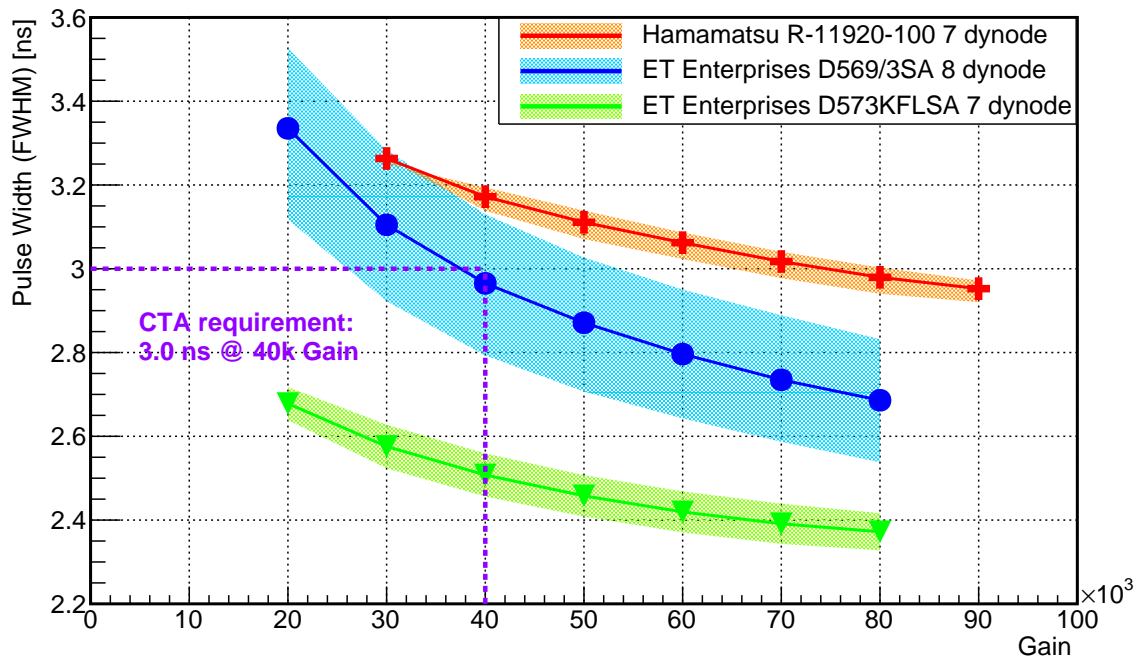


Figure 2.13.: Pulse width dependence on the gain of the PMT. The pulse width reduces with increasing gain. The markers indicate the mean value among the tested PMTs. The shaded area around shows the spread of the measurements among different samples. ET Enterprises reduced the pulse width by ~ 0.5 ns changing to a 7 dynode design. The Hamamatsu PMTs show a pulse width ~ 0.2 ns above the CTA requirement of 3.0 ns. This might be due to the limited set of three tested samples available for our measurements.

PMT Type	Average Pulse Width [ns]
R-129920-100	3.2 ± 0.1
D569/3SA	3.0 ± 0.1
D573KFLSA	2.5 ± 0.1

Table 2.6.: Results of the pulse width measurement. All ET Enterprises PMTs fulfill the CTA requirements for a gain of 40 000. The Hamamatsu PMTs have a pulse width 0.2 ns above the CTA requirement of 3.0 ns.

2.7. Transit Time Spread

The transit time is the time interval between a light pulse hitting the photocathode and the arrival of the output signal at the anode. The transit time spread (TTS) is an effect mostly caused by different trajectories of the photoelectrons between the photocathode and the first dynode. Different path lengths cause a time difference for the arrival time of the signal. This effect depends on the curvature of the entrance window, the focusing electrodes and also the size of the dynode. It must be small in order to assure a good time resolution for the CTA imaging camera. The TTS is optimized by the manufacturers with simulations of the ph.e trajectories. The measurement devices are again identical to the 1ph.e measurement described in section Sec. 2.5.1.

For the TTS measurement we have to ensure that the whole photocathode of the PMT is illuminated homogeneously. The numerical aperture of the used fiber output is specified from the manufacturer with 0.2. Assuming a refractive index in air of 1.0, we can calculate an opening angle of 11.5° for the light cone. To assure a homogeneous illumination of the PMT entrance window we only want to use the center of the light spot. Therefore, we increase the distance between the PMT and the optical fiber output to approximately 35 cm.

For a precise time resolution it is necessary to have a very stable light source. The laser head P-C-405 from PicoQuant LDH Series can guarantee a time jitter below 40 ps, which is much smaller than the expected TTS of around 1.5 ns [26]. Also the pulse generator has to provide a stable trigger signal for the laser and the oscilloscope to enable a precise time measurement. The time jitter of the trigger pulse is below 15 ps [32].

During the measurement the light intensity is set to a 1ph.e level to avoid multiple photon events. We start the measurement roughly at a voltage corresponding to a gain of 30 000. Afterwards, we measure four additional voltage steps with increments of 50 V. For each voltage we acquire 153942 laser shots. As a short reminder, we want to mention again that the recorded PMT signal has a negative sign due to a negative voltage applied to the cathode. This is important for the data analysis described in the following. To determine the TTS we search for the position of the minimum signal amplitude, which we define as arrival time of the signal. All arrival times of the signals are filled into a histogram. For the TTS analysis we only take PMT signals into account, which have between 80 % and 120 % of the 1ph.e charge. We calculate the TTS as FWHM of the distribution after fitting a Gaussian. Finally, we calculate the TTS dependence on the gain depicted in Fig. 2.14. Similar to the pulse width, the TTS reduces with increasing gain of the PMTs. Again, a decrease in TTS is visible for the ET Enterprises PMTs after changing to a 7 dynode

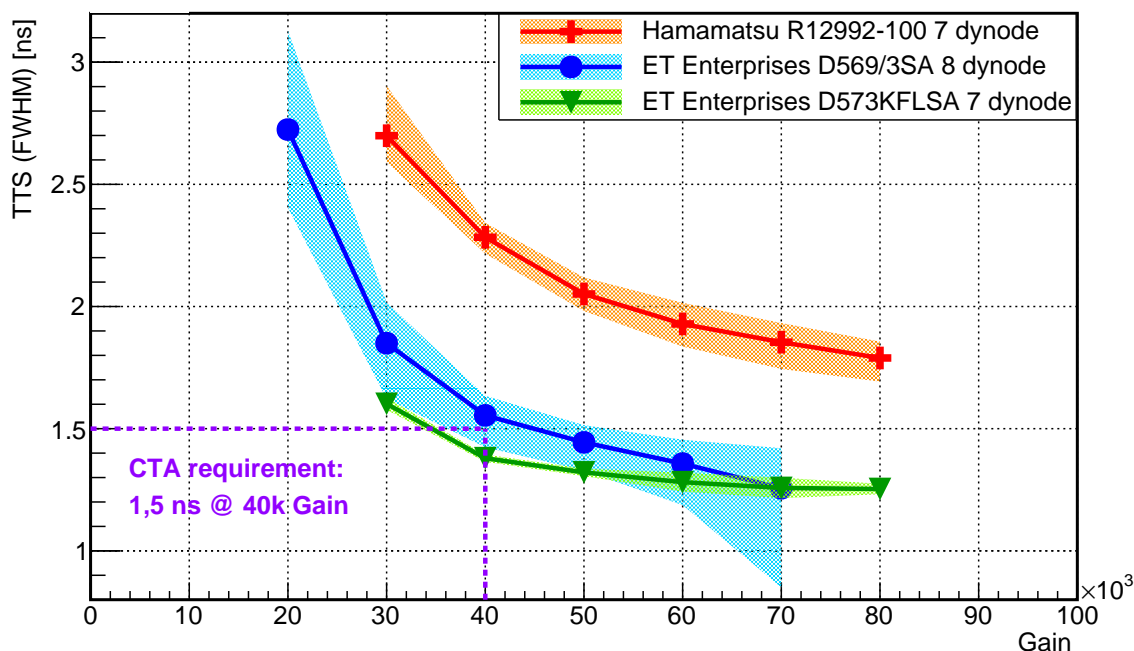


Figure 2.14.: Transit time spread dependence versus gain plot. For a higher gain the electrons are accelerated faster towards the dynode system. Thus, the TTS decreases. ET Enterprises reduced the TTS below the CTA requirements of 1.5 ns switching to a 7 dynode PMT. The time resolution of the Hamamatsu PMT is not as good and exceeds the CTA specifications by 0.7 ns, about 53 %.

version. The ET Enterprises PMT 573KFLSA fulfills the CTA requirements with a TTS slightly below 1.5 ns at a gain of 40 000. The Hamamatsu PMTs show a TTS at a gain of 40 000 of 2.3 ns which exceeds the CTA requirements for about 0.7 ns.

2.7.1. TTS Dependence on the Laser Intensity

Besides the gain dependence, we additionally evaluated the influence of the light intensity on the TTS. For this measurement we choose a set of eight light intensities between 1ph.e and 30ph.e. The test was performed with the Hamamatsu PMT R-1229920-100 Nr. ZQ952 which showed a good performance in the prior evaluation. The applied bias voltage at the PMT was increased in 50 V steps starting from 950 V. Again, we calculate the TTS as FWHM of a Gaussian function fitted to the distribution. This is important to know, because imaging cameras of IACTs are exposed to a continuous background illumination from the light of night sky.

The results are shown in a voltage versus TTS plot in Fig. 2.15. For increased light intensities a decrease of the TTS is visible. At the level of 10ph.e the TTS starts saturating. Above 20ph.e the TTS saturates at a level between 0.2 ns and 0.4 ns.

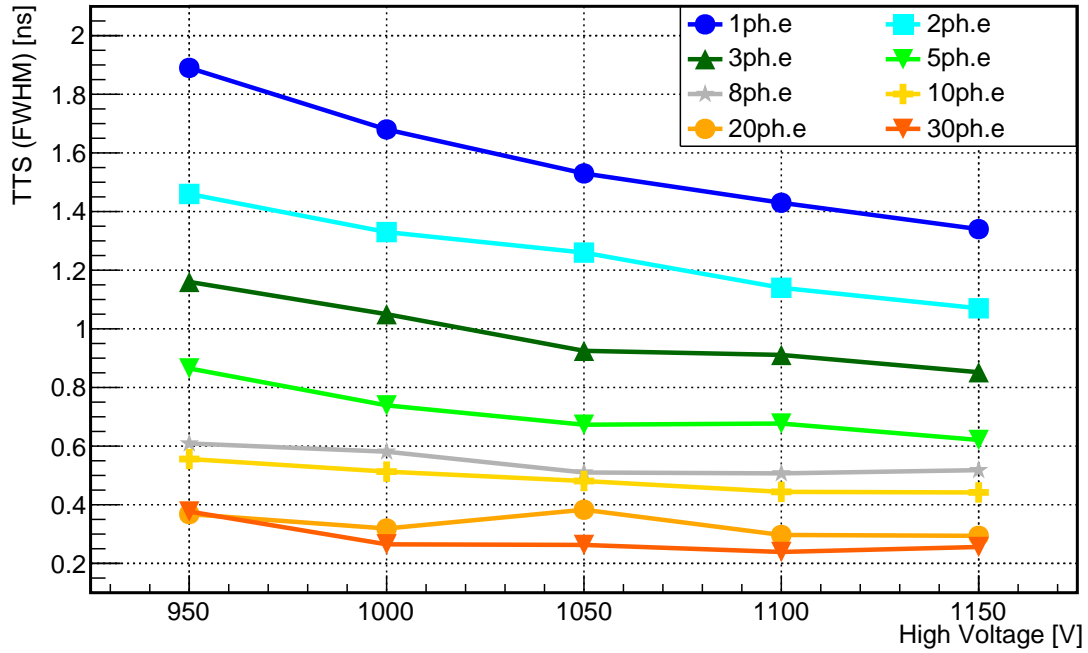


Figure 2.15.: TTS dependence on the high voltage and light intensity. The measurement points are connected with straight lines. For increasing light intensities the TTS decreases. At light intensities above 20ph.e the TTS saturates at a level between 0.2 ns and 0.4 ns.

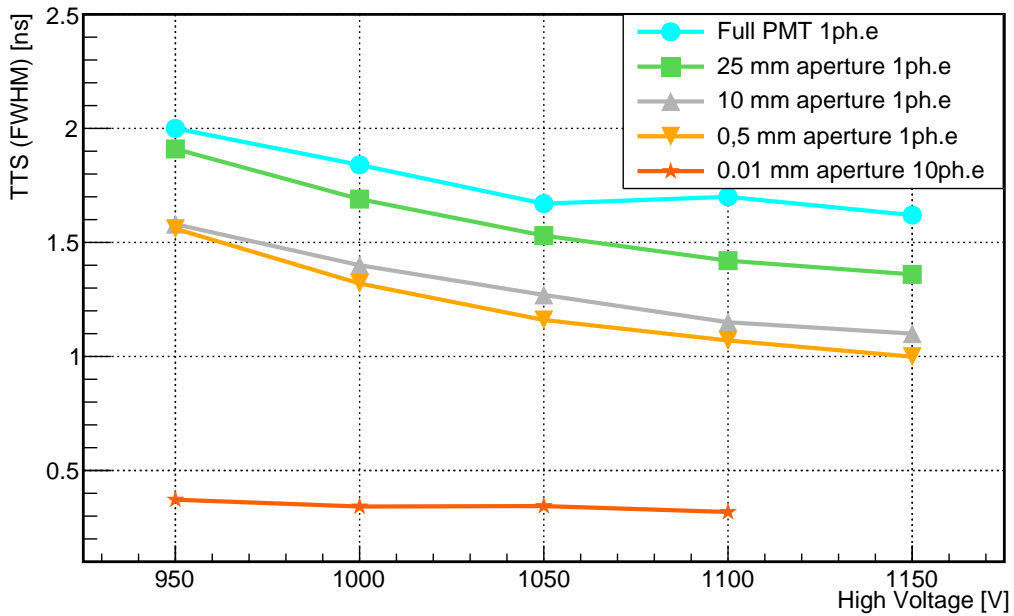


Figure 2.16.: TTS versus the high voltage and the illuminated photocathode area.

2.7.2. TTS Dependence on the Illuminated Photocathode Area

The TTS is dependent on the length of the trajectory between the photocathode and the first dynode. If we reduce the illuminated area at the photocathode, the possible bunch of trajectories becomes more homogeneous. Thus, the time jitter due to different path lengths decreases.

For this measurement, we produced five different apertures with a diameter between 0.01 mm and 30 mm. During the measurement, different apertures are mounted in front of the PMT entrance window in order to decrease the illuminated area of the photocathode. The results are shown in Fig. 2.16. As we expected, the TTS decreases with smaller aperture sizes. For the 0.001 mm aperture the light intensity had to be increased to 10ph.e in order to detect a signal and the TTS reduces towards 0.4 ns.

2.8. Probability of Afterpulses

Afterpulsing is an effect, that causes additional time delayed pulses after the initial signal in the absence of any real incoming photon. These pulses can have rather large amplitudes and might be interpreted as real signals [33]. This is one of the disadvantages using PMTs. One of the goals for the CTA camera is to reduce the trigger threshold. This requires PMTs with a low afterpulsing probability below 0.02 % for 4ph.e threshold.

Afterpulses are classified into two types. The first type is called optical or fast afterpulsing and has a typical time delay up to a few tens of ns after the initial signal [23]. The main reason for these fast afterpulses is due to photon emission by electron bunches within the dynode system of a PMT. These elastically scattered electrons can emit photons by relaxing into a lower energy state. The photons can propagate back to the photocathode and create a second time delayed pulse. This effect can be reduced by a special electrode next to the first dynode in order to prevent elastics scattering. In addition, the light propagation back to the cathode can be reduced by shielding the dynode chain.

The second class of afterpulses are so called charge induced afterpulses, that have a much longer time delay from several tens of ns up to some μ s [30]. Again, one can distinguish two main reasons based on the ionization of residual atoms and molecules within the tube. Despite the deep vacuum within the tube, photoelectrons can ionize residual atoms and

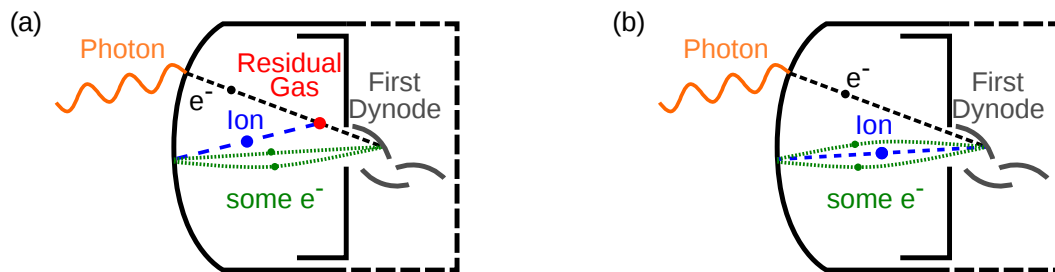


Figure 2.17.: Mechanisms for afterpulse production. (a) Ionization of residual atoms or molecules by photoelectrons on the way to the first dynode. (b) Ejection of positive charged ions from the first dynode due to photoelectron bombardment.

molecules on their way to the first dynode. These positive ions are accelerated in reverse direction back to the photocathode and release a second bunch of electrons without any real incoming light. These electrons are accelerated towards the first dynode and create a second, time delayed pulse after the initial signal. The process is depicted in Fig. 2.17 (a). To reduce the influence of the residual gas, the vacuum level in the tube can be increased. Furthermore, so called getters (see Fig. 2.2) are placed in the tube in order to absorb residual atoms and molecules. The second mechanism producing charge induced afterpulses is also based on ionization. In this case, the photoelectron hits the first dynode and creates a bunch of secondary electrons. Additionally, due to the presence of different chemical elements adsorbed on the dynode surface, it ejects a positively charged ion, which is back accelerated to the cathode and produces a second, time delayed pulse. A scheme of this mechanism is drawn in Fig. 2.17 (b).

2.8.1. Cumulative Afterpulse Probability

For measuring afterpulses, we use the default setup for 1ph.e (see Fig. 2.5.1). The afterpulse rate is independent from the light intensity [30]. To reduce the number of acquisitions we increase the laser intensity to about 10ph.e. The voltage of the PMT is set to provide a gain of 40 000 using the results of Sec. 2.5.2. To correct for the dark current we record pedestal data blocking the laser beam with a beam interrupter. For each acquisition we

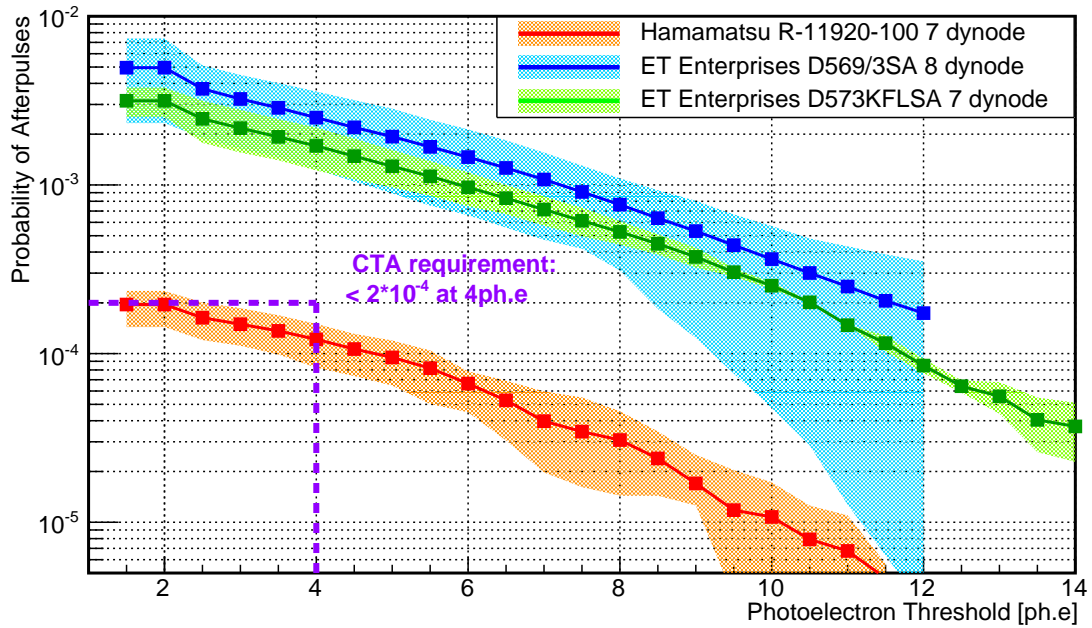


Figure 2.18.: The plot shows the threshold level in multiples of photoelectrons on the x-axis versus the cumulative afterpulse probability on the y-axis. The Hamamatsu PMTs fulfill the CTA requirements with an extraordinary low afterpulse probability below 0.02 %. The ET Enterprise managed to reduce the afterpulse probability slightly switching to a 7 dynode design. But still they exceed the specifications an order of magnitude.

record data for 5 μs , which limits the number of waveforms to 45955 by the internal buffer size of the oscilloscope.

To determine the afterpulse probability, we count all afterpulse events $N_{AP}(k)$ above a certain threshold k . The threshold is set to multiples of the photoelectron charge for a gain of 40 000. To correct the influence of the dark current we subtract the number of dark current events N_{DK} for the corresponding threshold of the pedestal run. To calculate the cumulative afterpulse probability, the number of afterpulse events is divided by the total number of events N_{tot} normalized to the number of photoelectrons of the incoming laser pulse I_{pulse} :

$$P_{AP}(k) = \frac{N_{AP}(k) - N_{DK}}{N_{\text{tot}} \cdot I_{\text{pulse}}} \quad (2.27)$$

As a result, we obtain a plot with the photoelectron threshold in multiples of photoelectrons on the x-axis versus the cumulative afterpulse probability on the y-axis shown in Fig. 2.18. The Hamamatsu R-12992-100 PMTs have the lowest afterpulse probability and fulfill the CTA requirements for a 4ph.e threshold. The ET Enterprises PMTs D569/3SA and D573KFLSA have an afterpulse probability one magnitude above the requirements. The higher afterpulse probability is partially due to a lower vacuum level. ET Enterprises explained that for the D573KFLSA series the focus was set to a fast timing. For the next iteration the company will try to improve the vacuum level within the tube. ET Enterprises showed with earlier PMTs, that they are also capable to reach the CTA specifications.

PMT Type	Afterpulse Probability at 4ph.e Threshold [%]
R-129920-100	0.012 ± 0.003
D569/3SA	0.25 ± 0.08
D573KFLSA	0.17 ± 0.06

Table 2.7.: Results of the cumulative afterpulse probability. The CTA specifications request an afterpulse probability below 0.02 %.

2.8.2. Afterpulse Arrival Times

In addition to the afterpulse probability we also evaluate the afterpulse arrival time. The arrival time of an afterpulse is determined as time difference between the initial signal and the arrival of the delayed pulse at the anode. Our measurement is not sensitive for optical afterpulses faster than 40 ns due to their very small amplitude. Thus, we record afterpulses between 40 ns and 5 μs at a threshold level of 1.5ph.e. Again, we correct for the dark counts by a pedestal subtraction. The results for one selected PMT of each type are shown in Fig. 2.19. One can see that afterpulses are not uniformly distributed in time. The bigger part of afterpulses arrives within 3.0 μs . Additionally, in each spectrum several peaks at specific time positions are visible, which are related to the primary ion causing the afterpulse.

To estimate the transit time one can use the concept of a parallel plate capacitor. The first plate corresponds to the photocathode of the PMT. The second one to the first dynode, which was identified as main source for ion ejection. Due to voltage stabilization by a

Zener Diode in the voltage divider the electrical field E is assumed to be constant. This results in an acceleration a of a charged particle of:

$$m \cdot a = q \cdot E = q \cdot \frac{U}{d} \quad (2.28)$$

where m is the mass of the charged ion and q the corresponding charge. The electrical field of a plate capacitor is determined by the applied potential U and the distance d between the plates, which for a PMT corresponds to the distance between the photocathode and the first dynode [30]. The corresponding time of flight is calculated assuming a constant acceleration a and zero initial velocity:

$$t = \sqrt{\frac{2 \cdot d}{a}} \quad (2.29)$$

This results in the following equation for the time of flight of an ion between the photocathode and the first dynode:

$$t = \sqrt{\frac{2 \cdot d^2 \cdot m}{q \cdot U}} \quad (2.30)$$

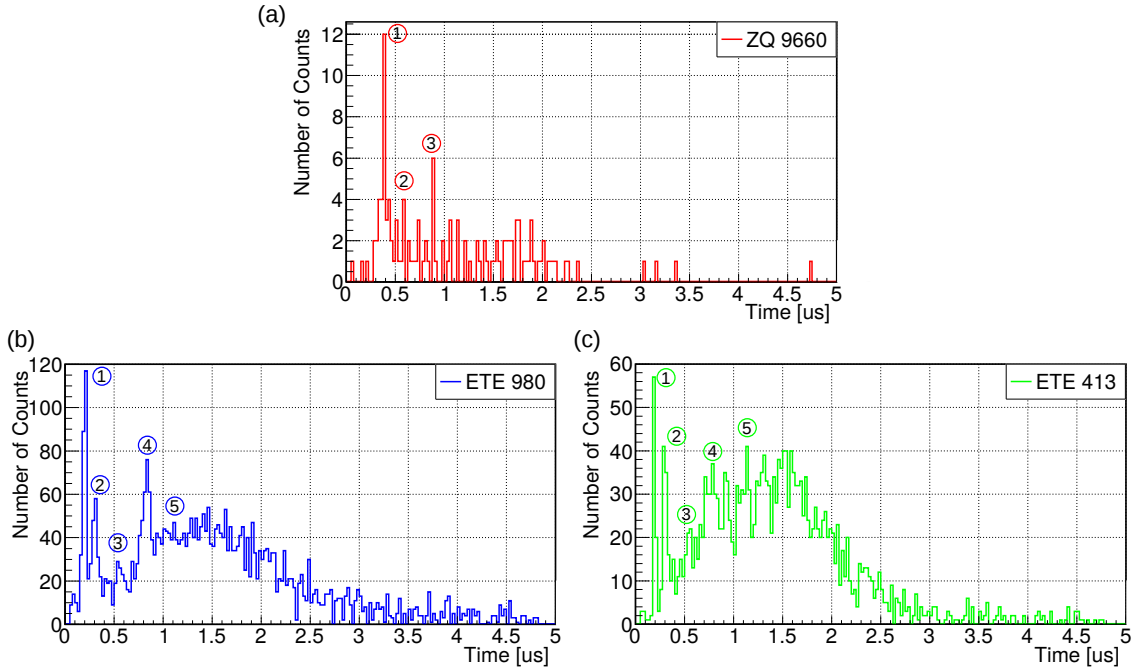


Figure 2.19.: Histograms of the afterpulse arrival times of selected PMTs (a) Hamamatsu R-129920-100 (b) ET Enterprises D569/3SA (c) ET Enterprises D573KFLSA. Most of the afterpulses arrive within $3 \mu\text{s}$. Each spectrum shows specific peaks that can be related to the charge and mass of the specific primary ion. Each peak identified as ion is marked with a number. The larger number of peaks in the histograms (b) and (c) is mainly caused by a higher content of residual gas.

Thus it appears that we can neglect the traveling time of the electron released by the ion at the photocathode. The contribution of the electron to the total delay time of the afterpulse is much smaller than the contribution of the ion due to the 1808 times smaller electron mass. Using the previously introduced Eq. 2.28 and Eq. 2.29 one can calculate the mass to charge ratio R :

$$R = \frac{m/m_p}{q/e} = \frac{t^2 \cdot e \cdot U}{2 \cdot d^2 \cdot m_p} \quad (2.31)$$

Knowing the peak position, the R ratio simplifies the ion identification. We can extract the arrival times of the peaks from the histograms in Fig. 2.19. The distance between the photocathode and the first dynode is 27 mm for the Hamamatsu PMTs and 25 mm for the PMTs from ET Enterprises.¹ The potential difference between the photocathode and the first dynode is 300 V stabilized by a Zener diode in the voltage divider [21].

For a proper error calculation, we have to estimate the uncertainties of the three main error sources: voltage, distance and arrival time. The error of the voltage is determined by the voltage divider and below 3 % of the applied voltage. The distance can vary quite a lot due to the curved shape of the entrance window and is estimated with 15 %. The time accuracy is smaller than the bin size of 25 ns. The error of the mass to charge ratio is derived from Eq. 2.31 as follows:

$$\Delta R = \sqrt{\left(\Delta U \cdot \frac{t^2 \cdot e}{2 \cdot d^2 \cdot m_p}\right)^2 + \left(\Delta d \cdot \frac{-t^2 \cdot e \cdot U}{d^3 \cdot m_p}\right)^2 + \left(\Delta t \cdot \frac{t \cdot e \cdot U}{d^2 \cdot m_p}\right)^2} \quad (2.32)$$

¹Both values were provided on our request by the manufacturers. They are not verified by own measurements but are in a good agreement with our measurements.

PMT	Peak Number	Time [ns]	R ratio	Possible Ion
Hamamatsu R-129920-100	1	388	3.0 ± 0.5	${}^3\text{He}^+$
	2	588	6.8 ± 1.1	N
	3	888	15.5 ± 2.4	$N_2 \quad O_2$
ET Enterprises D569/3SA	1	213	1.0 ± 0.3	H^+
	2	313	2.2 ± 0.5	${}^2\text{H}^+ \quad {}^2\text{He}$
	3	538	6.6 ± 1.1	N
	4	813	15.1 ± 2.6	$N_2 \quad O_2$
	5	1140	29.8 ± 5.0	larger ions
ET Enterprises D573KFLSA	1	188	0.8 ± 0.2	H^+
	2	288	1.9 ± 0.4	${}^2\text{H}^+ \quad {}^2\text{He}$
	3	713	11.8 ± 2.0	$H_2O \quad CH_4$
	4	788	14.3 ± 2.4	$N_2 \quad O_2$
	5	1140	29.8 ± 5.0	larger ions

Table 2.8.: Identification of the afterpulse ion sources. The arrival times of the afterpulse peaks are shown in column three, followed by the calculated mass to charge ratio R . The possible ion sources of the afterpulses are shown in column five.

The results of the mass to charge ratio calculation and the corresponding errors are shown in Tab. 2.8 together with the most probable ions. A ratio R of one corresponds to a hydrogen ion.

2.9. PMT Entrance Window Glow

One major difference between the tested PMTs is the entrance window. While Hamamatsu PMTs are using a mat window, the ET Enterprises PMTs have a clear one (see Fig. 2.4). It is well known, that the photocathode coating on the inner side of the entrance window causes a certain amount of back reflection due to the very high refractive index of around 3. Thus, a characteristic reflection pattern from the PMT entrance window is visible. The goal of this measurement is to evaluate the differences between a mat and a clear window. In order to measure the optical light emission, an ultra sensitive CCD camera from the Andor CLARA series is used [34]. The camera is equipped with a cooling to stabilize the temperature in order to reach a very low readout noise of typically $2.4 e^-$ at 1 MHz. During the measurement the CCD chip is cooled to $-45^\circ C$. A 405 nm laser produces pulsed light with a frequency of 31.25 kHz. The light is fed into an optical fiber and illuminates the PMT window with a spot size of roughly 1 mm diameter. The intensity is rather high at a level of several tens of photons per shot. Images are taken with an exposure time of 10 s of the CCD camera.

The CCD images are depicted in Fig. 2.21. The mat entrance window of the Hamamatsu tube shows a diffuse light scattering. The light emission is coming from a region with a diameter of 1 cm. The situation changes for the ET Enterprise tubes with the clear entrance window. Now a bright spot of the initial laser beam is visible. It is surrounded

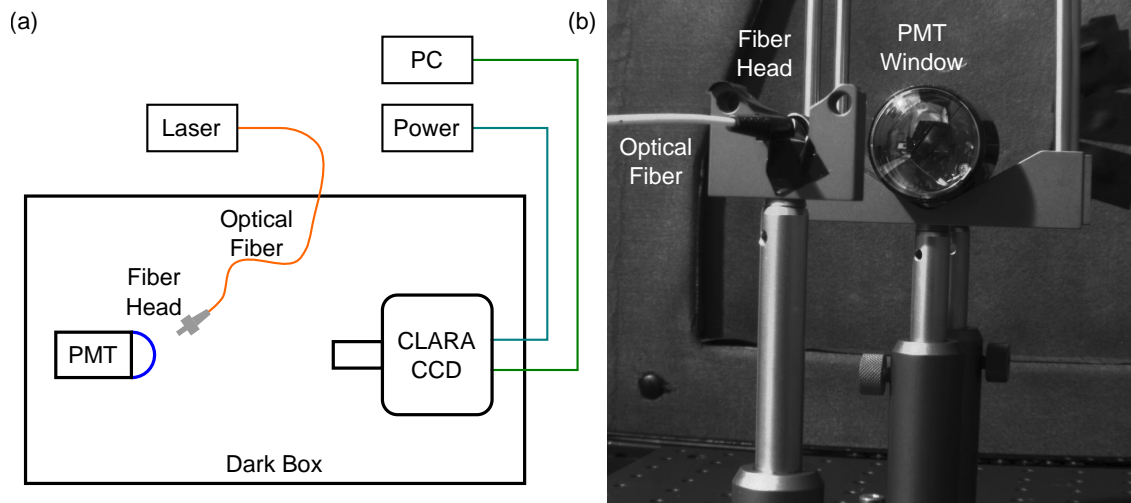


Figure 2.20.: (a) Schematics showing the structure of the PMT glow measurement setup. A 405 nm laser provides the pulsed light for the measurement which is fed into an optical fiber and illuminates the PMT window. For image taking a CLARA CCD camera is used. (b) Image taken by the CCD Camera during daylight showing the PMT and the optical fiber head.

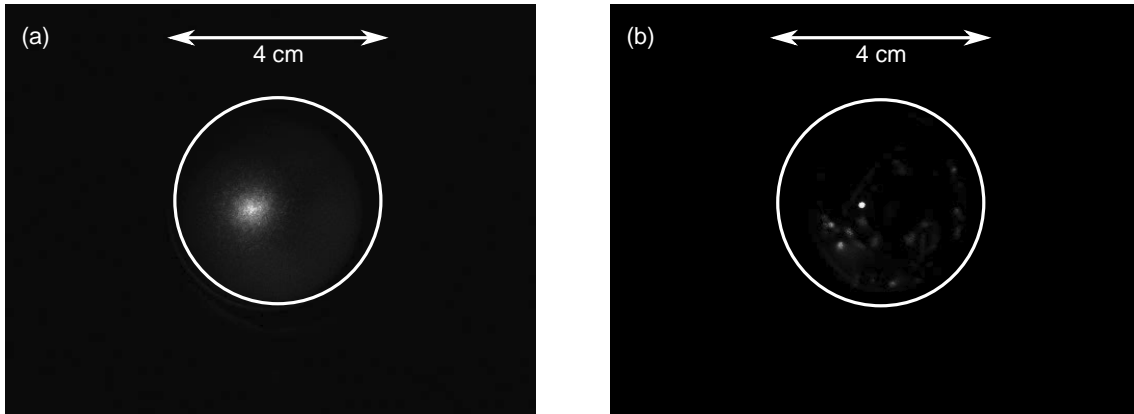


Figure 2.21.: PMT entrance window glow. The total size of the entrance window is indicated with a white circle. (a) Mat entrance window of the Hamamatsu PMT showing a diffuse scattering of the laser spot. (b) ET Enterprises PMT with a clear entrance window and the initial laser spot visible in the center. Several additional back reflections of the spot from the focusing electrodes can be seen in the window.

by several additional spots, back reflected from the focusing electrodes.

2.10. Summary of the PMT Characterization

Both companies Hamamatsu and ET Enterprises have developed in multiple iterations PMTs for the CTA project. The tested samples show a high QE between 34 - 39 %, which is an improvement of more than 10 % compared to the QE of ten year old PMTs. Additionally, the photoelectron collection efficiency was optimized to ≥ 95 % which is already at the very edge of technical feasibility. Meanwhile, the Hamamatsu PMTs became a commercial product that shows a very low afterpulsing ≤ 0.02 % at a threshold of 4ph.e. This is one of the lowest values achieved with PMTs worldwide. The latest ET Enterprise PMTs show a relatively high afterpulsing but have an exceptional good time resolution with a pulse width of 2.5 ns and a TTS of 1.5 ns. ET Enterprises will finalize their PMT development producing a PMT where all the best features of their development will be composed. As soon as they finish the production they will also have one of the best products.

3. Upgrade of the LIDAR System for the MAGIC Telescopes

Modern atmospheric research is hard to conceive without the use of remote-sensing techniques. Light detection and ranging (LIDAR) is the most frequently applied technique for nowadays research on profiling the atmosphere. The working principle of LIDAR dates back to pre-laser times and is based on the concept of RADAR (radio detection and ranging). The main difference is the source of the electromagnetic radiation as it is implied by the name. LIDAR requires the use of a strong light source for signal generation. Thus, the development of modern LIDAR technologies started with the invention of the laser in 1960 [35].

The first LIDAR measurement using a pulsed ruby laser was performed by G. Fiocco and G. Grams in 1963. At this time, the existence of an aerosol layer at an altitude of about 20 km was already proven by direct measurements from balloons and aircraft. The goal of G. Fiocco and G. Grams was to confirm this results by an optical measurement from ground. For this purpose they measured the light echoes of their laser in between 14 km to 25 km altitude using a PMT in a ground based telescope. The signal at around 20 km high was much stronger than expected from the molecular atmosphere and indicated the presence of a large aerosol layer [36]. This experiment was the beginning of modern atmospheric research using LIDAR as laser remote-sensing technique.

The high spatial and temporal resolution of the measurement, the possibility of a real time monitoring of the atmosphere under ambient conditions and the potential to cover a altitude range from ground to several tens of kilometers make up the merit of current LIDAR instruments. They are particularly useful for the investigation of highly variable parameters like atmospheric transmission and the altitude of cloud and aerosol layers. The LIDAR technique is able to observe processes on scales that extend from a few tens of meters and seconds to a full monitoring of the whole atmosphere over several years [37].

As the Earth's atmosphere is a part of the detection technique of the MAGIC telescopes, it can have a rather large impact on the measurement results. A precise knowledge about the current conditions of the atmosphere in the field of view of the MAGIC cameras can enhance the performance of the instrument as well as the quality of the recorded data. For this purpose a LIDAR system was reinstalled aside the telescopes and resumed normal operation in 2011 [38].

This chapter is dedicated to upgrade for the MAGIC telescope's LIDAR system, which was tested on site in November 2015. At the beginning of this chapter the working principle of LIDAR (Sec. 3.1) and the characteristics of the Earth's atmosphere (Sec. 3.2) are explained. Sec. 3.3 provides a short outline of the characteristics of the MAGIC telescope's LIDAR system and is followed by Sec. 3.4, which defines the goals of the LIDAR upgrade. The new design of the LIDAR detector, including a separate high voltage supply and new readout electronics is described in detail in Sec. 3.5. The results of first test runs with the new

system are shown in Sec. 3.6.

3.1. The LIDAR Technique and the Basic Equation

In principle a LIDAR system consists of a transmitter and a receiver unit. Short light pulses with a duration of a few nanoseconds and characteristic spectral properties are generated by a laser. To collimate the laser beam many systems add a beam expander to the transmitter unit to reduce the divergence of the light beam.

At the receiver side, a telescope collects the backscattered photons from the atmosphere and focuses the light to an optical light detection system. Depending on the application, specific wavelength or polarization states of the light are selected. In the simplest case, an interference filter is placed in the optical path. The filter transmits light in a certain band around a central wavelength of interest and strongly suppresses light outside the transmission band, e.g. the light of night sky. The selected radiation is directed onto a detector, sensitive for single photon counting, which converts the optical signal into an electrical current. Signal detection is very frequently realized using PMTs or hybrid photodiodes. The signal intensity is recorded depending on the time elapsed after triggering the laser, recorded with a computer and analyzed by a software algorithm [37].

The signal intensity is converted back into a number of photon counts per time interval Δt after the emission of the laser pulse. The resolved time interval corresponds to following

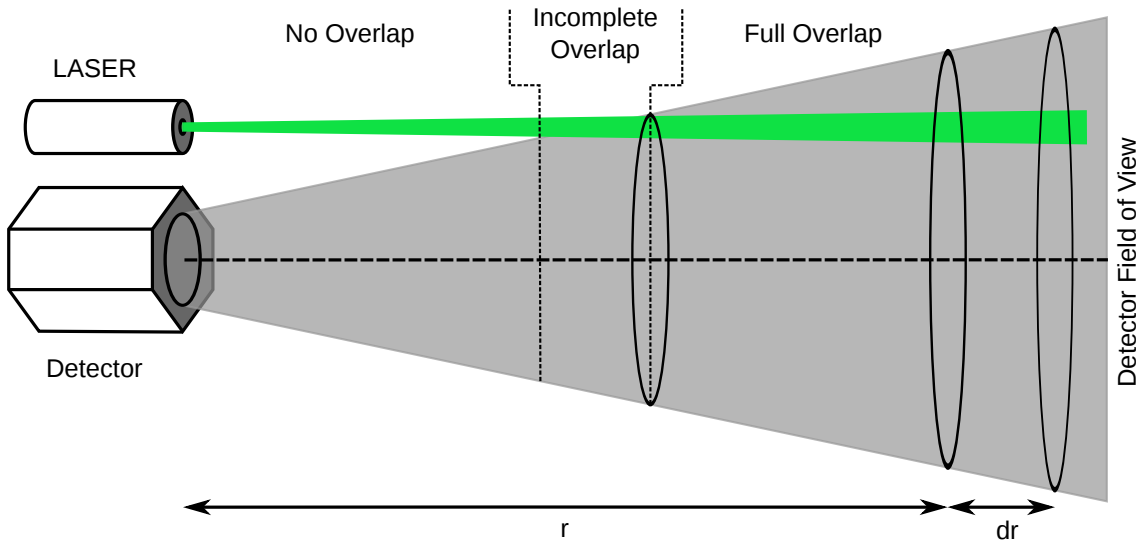


Figure 3.1.: Illustration of the LIDAR working principle. A pulsed laser emits light at a certain wavelength which is backscattered in the atmosphere at a distance r and received by a detector. The laser beam does not necessarily overlap with the field of view of the detector. The LIDAR range is divided into three different overlap region. This behavior is described by a geometrical factor in the LIDAR equation.

atmospheric height resolution Δr :

$$\Delta r = \frac{\Delta t \cdot c}{2} \quad (3.1)$$

where c is the speed of light. The factor $1/2$ is related to the fact that the light has to travel twice the distance, forth from the laser and back to the detector. Theoretically, the atmospheric resolution is limited by the length of the laser pulse. A 50 ns light pulse results in a resolution of 13 m. With nowadays ultra-short pulsed lasers this limit is vanishing and replaced by other hardware constraints.

For a better understanding of the LIDAR return signal a theoretical discussion of the LIDAR instrument is necessary. The backscattered light is recorded in form of a photon counting rate $N(t)/dt$. This number can be converted into a distance dependence $N(r)/dr$ using Eq. 3.1. In the simplest form, the detected signal can be estimated with the single scattering LIDAR equation:

$$\frac{dN(r)}{dr} = C \cdot G(r) \cdot \beta(r) \cdot \tau(R) \quad (3.2)$$

The number of photons per distance element $N(r)/dr$ counted on the detector from the distance r is made up of a product of four factors. The first factor C is a system constant summarizing the performance of the whole experimental setup. $G(r)$ is a term describing the range-dependent geometry and optical effects of the system. The first two factors C and $G(r)$ are completely determined by the measurement setup and can be optimized for the application.

The information about the atmosphere are contained in the last two factors. The ability of the atmosphere to scatter the light back to the original direction is described in the term $\beta(r)$ called backscattering coefficient. It is dependent on the distance r and can be estimated by several atmospheric models (see Sec. 3.2). The light getting lost on the way from the laser to the distance r and back to the detector is described by the factor $T(r)$. Both terms $\beta(r)$ and $T(r)$ contain all measurable quantities of the experiment.

In the following, we will have a closer look to the contribution of each component to the single scattering LIDAR equation. At the beginning, we consider the system constant which contains information about the instrument like the original number of photons N_0 and the photon collection efficiency η :

$$C = N_0 \cdot \eta \quad (3.3)$$

The photon collection efficiency summarizes several parameters like the mirror reflectivity, the transmission of filters, and the quantum efficiency of the hybrid photodiode. Going into more detail, Fig. 3.1 shows a simplified sketch of a typical LIDAR geometry in order to introduce the components of the geometrical factor:

$$G(r) = \frac{A}{r^2} \cdot O(r) \quad (3.4)$$

A is the collection area of the receiver optics, responsible for detecting the backscattered light. A/r^2 is the solid angle of the detector as seen from the point of scattering. The laser

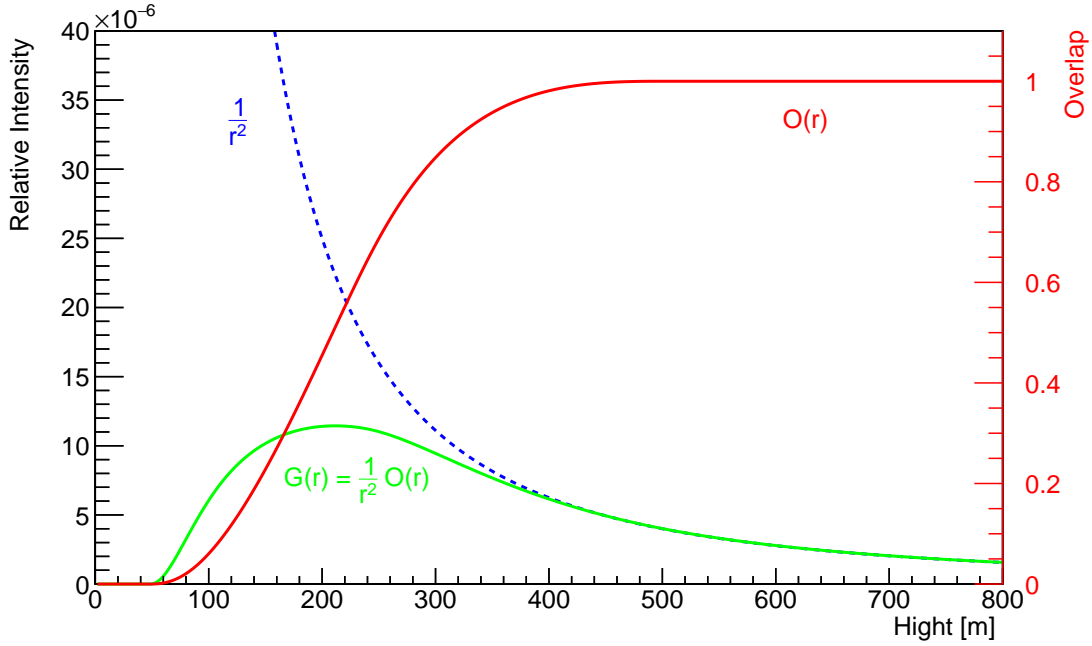


Figure 3.2.: Simulation of the geometric factor $G(r)$ of the MAGIC telescope's LIDAR system for an altitude up to 800 m above the instrument. The red curve shows the overlap function of the detector field of view with the laser beam. Complete overlap is reached 450 m above the telescope indicated by $O(r) = 1$. The blue line shows the $\frac{1}{r^2}$ term of the geometrical factor. The green curve shows the influence of the geometrical factor on the overall signal dynamics.

beam and the field of view of the receiver must not necessarily overlap over the whole range. This fact is compensated by the overlap function $O(r)$ which can adapt to values between 0 and 1. In Fig. 3.2 a simulation of the overlap function for the MAGIC telescope's LIDAR system is shown. Laser beam and field of view of the telescope completely overlap at an altitude of 450 m above the telescope. The geometric factor has a large impact on the expected shape of the LIDAR signal.

The backscattering coefficient is the specific term for the scattering angle of 180° . It is the sum over all types of scatterers which contribute to the process of backscattering:

$$\beta(r) = \sum_j^{max} \beta_j \quad (3.5)$$

In the atmosphere the two most important components are scattering by molecules β_{mol} and particulate matter like aerosols β_{aer} . Molecular scattering mainly occurs from nitrogen and oxygen and in the first order depends on the density of the atmosphere. Thus, in the case of a ground based observation scattering decreases with hight. Light scattering from aerosols is varying on large scales depending on the current state of the atmosphere. Possible particles can be from various origin and state. Starting from tiny water droplets which also might be frozen, there is a variety of organic compounds like pollen and biogenic

material. Finally, there is a huge set of solid state dust particles with a typical size between 100 nm and 100 μm .

The transmission term is restricted to values between 0 and 1 and can be written in the following from:

$$\tau(r) = \exp\left(-2 \int_0^r \alpha(r', \lambda) dr'\right) \quad (3.6)$$

The integral considers the path from the LIDAR to the distance r . The factor two in front, takes into account the two-way travel of the light along this path. All transmission losses are summarized in the extinction coefficient $\alpha(r, \lambda)$. Light extinction is based on scattering and absorption of photons by molecules and particles. Thus the extinction coefficient is also wavelength dependent.

Finally, putting Eq. 3.3- Eq. 3.6 together one ends up with the complete single scattering LIDAR equation:

$$\frac{dN(r)}{dr} = N_0 \cdot \eta \cdot \frac{A}{r^2} \cdot O(r) \cdot \beta(r) \cdot \exp\left(-2 \int_0^r \alpha(r') dr'\right) \quad (3.7)$$

3.2. Characteristics of the Earth's Atmosphere

This subsection gives a short overview over the characteristics of the Earth's atmosphere. In contrast to optical astronomy, the IACT technique is not only sensitive to the total light attenuation in the atmosphere but also on altitude dependent variations. Primarily, major changes in the atmosphere are caused by the chemical composition and the natural density of air molecules.

A reference for the principal sea-level constituents of air is stated in the atmospheric model of the U.S. Standard Atmosphere which was published in its final version in 1976. The main constituents of the U.S. Standard Atmosphere are listed in Tab. 3.1. The mixing ratio of the components can change with altitude. The most common example is ozone. It is mainly present in the lower stratosphere between approximately 20 km to 30 km in the so-called ozone layer. In polluted atmospheres and under adverse weather conditions the

Molecule	Formula	Fraction [%]
Nitrogen	N_2	78.084 %
Oxygen	O_2	20.946 %
Argon	Ar	0.934 %
Carbon Dioxide	CO_2	0.0397 %
Neon	Ne	0.001818 %
Helium	He	0.000524 %
Methane	CH_4	0.000179 %

Table 3.1.: Average composition of the U.S. Standard Atmosphere of 1976. Based on the assumption of dry perfect gas at sea-level (taken from [39]).

concentrations of ozone are often an order of magnitude greater than expected from the U.S. Standard Atmosphere [39].

Barometric Atmosphere: The natural density of air molecules is closely related to the air pressure and the temperature. Under the assumption of an isothermal atmosphere, which implies a constant temperature, the pressure profile of the atmosphere can be estimated with the barometric formula:

$$p(h) = p_0 \cdot \exp\left(-\frac{h}{\frac{RT}{Mg}}\right) = p_0 \cdot \exp\left(-\frac{h}{h_c}\right) \quad (3.8)$$

p_0 is the pressure at sea-level, R is the universal gas constant, T the absolute temperature, M the medial molar mass of the Earth's air and g the gravitational acceleration. One can summarize several constants in the factor h_c which is the characteristic altitude step where the pressure decreases by the factor of e . Inserting a temperature of 15°C the characteristic altitude corresponds to $h_c = 8300\text{ m}$.

U.S. Standard Atmosphere: The assumption of constant temperature is only a rough first order approximation for the real Earth's atmosphere. This fact was taken into account

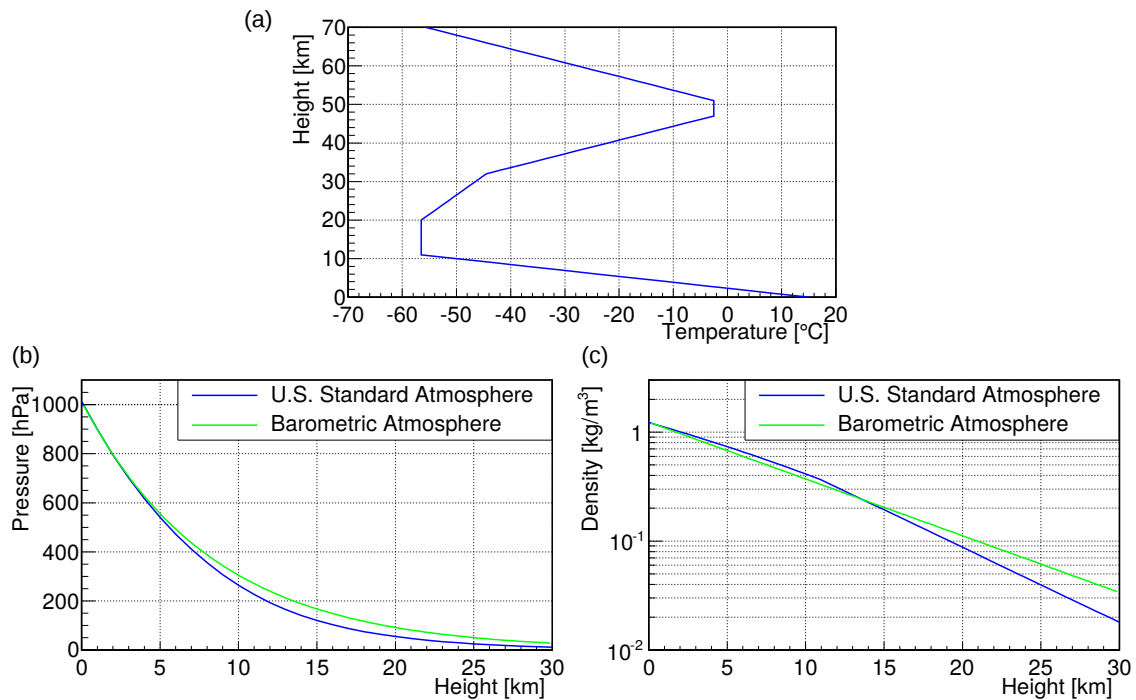


Figure 3.3.: Characteristics of the Earth's atmosphere (a) Temperature profile of the U.S. Standard Atmosphere of 1976 (tabulated values taken from [40]) (b) Pressure profile calculated with Eq. 3.8 assuming a barometric atmosphere with constant temperature in comparison with the U.S. Standard atmosphere model (tabulated values from [40]) (c) Density profile derived from the air pressure with logarithmic scale. The barometric formula is a good approximation below 12 km altitude.

for the model of the U.S. Standard Atmosphere of 1976, which defines a temperature profile. A plot of the altitude dependence of the temperature is shown in Fig. 3.3 (a). Beside the temperature the U.S. Standard Atmosphere also defines a characteristic pressure profile which is shown in Fig. 3.3 (b) in comparison with the barometric formula.

For determining the light attenuation of the Earth's atmosphere the major parameter is the density of air molecules. It can be directly derived from the air pressure using the ideal gas law in its molar form:

$$p = \rho \cdot \frac{R}{M} \cdot T \quad (3.9)$$

where ρ is standing for the air density. The density profile of the atmosphere is shown in Fig. 3.3 (c) it has a major impact on the Rayleigh scattering described in the next section.

3.2.1. Atmospheric Attenuation of Light

Theoretically, there are two possibilities for light attenuation in the atmosphere: the first one is absorption, the second one scattering. If a molecule absorbs an electromagnetic wave, the molecule is excited into an higher energy state. The molecule relaxes back into its original state releasing thermal energy by interactions with other molecules. In the case of scattering the initial electromagnetic wave is redirected into a different direction by interaction with a molecule. Fig. 3.4 gives an overview over different contributions to atmospheric attenuation. It shows, that for wavelength below 300 nm light is primarily attenuated by absorption due to the ozone layer. For wavelength above 300 nm, which are particular interesting for observations conducted by MAGIC, there are two main contributions to the atmospheric attenuation from molecular and aerosol scattering. In the following, we will have a closer look to both processes described by the Rayleigh respectively the Mie theory and their influence on in the Earth's atmosphere.

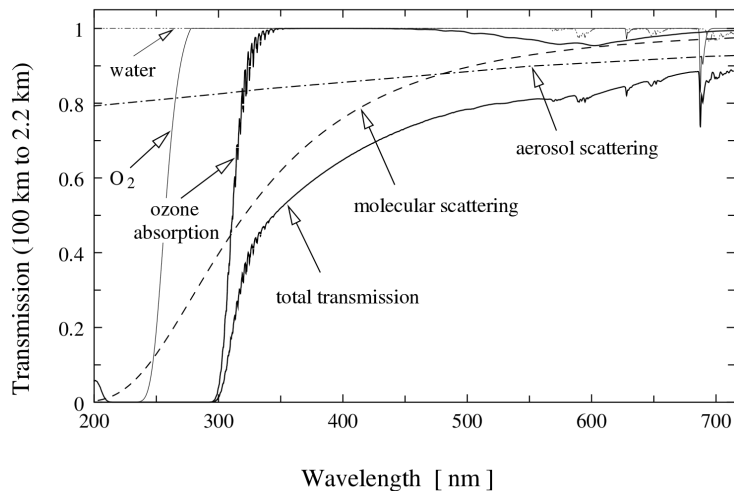


Figure 3.4.: Different contributions of absorption and scattering mechanisms to the atmospheric transmission between 2.2 km to 100 km (taken from [41]).

Rayleigh Scattering describes electromagnetic scattering on point-shaped particles of vanishing size, which are assumed to be much smaller than the incident light wave. It appears in polarizable media along the path of light where small dipole moments are induced. These dipoles emit dipole radiation in all directions. This effect was described by Lord Rayleigh's famous λ^{-4} law of molecular scattering:

$$I_{\text{scatt}} = I_0 \cdot \frac{8\pi^4\alpha^2}{\lambda^4} \frac{1 + \cos^2(\Theta)}{r^2} \quad (3.10)$$

here I_{scatt} is the scattered light intensity, Θ is the relative angle to the direction of initial light propagation, I_0 is the initial intensity, α is the polarization, λ is the wavelength of the light and r is the distance from the scattering center.

The scattered light intensity can be divided into two components. The first component I_1 in the plain perpendicular to the polarization axis of the induced dipoles is independent from the angle Θ . The second component I_2 is parallel to the dipole axis and shows the characteristic $\cos^2(\Theta)$ dependence. The sum of both components results in the $1 + \cos^2(\Theta)$ dependence of the Rayleigh formula in Eq. 3.10. A sketch illustrating this effect is shown in Fig. 3.5 (a).

Rayleigh scattering shows a λ^{-4} dependence on the wavelength of the scattered light. This explains why shorter wavelength in the blue light regime are scattered and deflected stronger. This effect is visible on the clear daytime sky, which shines in diffuse blue light.

Mie Scattering is a theory providing a insight into the processes of molecular scattering. In contrast to Rayleigh scattering, the Mie theory describes scattering on spherical particles and molecules of approximately the same size as the wavelength. This is the case for haze and dust particles in the atmosphere as well as for water droplets in cloud

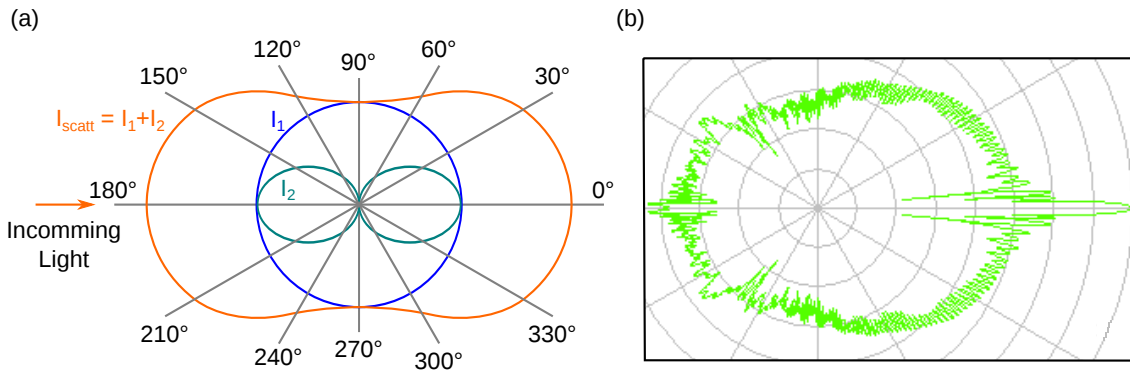


Figure 3.5.: Angular dependence of the scattering intensity. (a) For Rayleigh scattering the forward- and backscattering intensity is twice as high as for perpendicular directions towards the incident light (adapted from [42]). (b) For Mie scattering on a water droplet with the radius of 10 μm . The direction of the incident light is from left to right. The circular lines indicate a change of intensity by an order of magnitude. Compared to Rayleigh scattering a peak in forward direction is visible (plot made with the calculation software "MiePlot" [43]).

layers. Thus, the Mie theory is a very important tool for meteorology and atmospheric science where diameter to wavelength ratios in the same order of magnitude appear very frequently. Additionally, there are several applications for particle characterization by means of optical light scattering.

The Mie theory is based on an exact solution of the Maxwell's equations for an incident plane wave scattered on a spherical object of a given size and dielectric constant. It is possible to extend the calculations to a given volume element with a certain amount of particles by summing over all particles. This approximation can describe the situation of dust and cloud layers quite well. For very small particles Mie theory converges to Rayleigh scattering. In the opposite case, for very large spherical structures it matches with geometrical optics.

The most notable feature of the angular intensity distribution of Mie scattering is a huge peak in forward direction. Most of the intensity is scattered in directions close to the one of incident light. The angular intensity distribution of Mie scattering on a water droplet is shown in Fig. 3.5 (b). For our application in a LIDAR system the additional back scattering of the laser light from cloud layers is mainly based on Mie scattering and makes them detectable.

Apart from classical elastic scattering also inelastic electromagnetic scattering can occur. When light interacts with a molecular dipole, similar to Rayleigh scattering, it is possible to excite vibrational or rotational states of a molecule. This effect is called Raman scattering and represents a powerful tool for advanced LIDAR applications which can identify single constituents of the Earth's atmosphere.

3.2.2. Characteristics of the Atmosphere at the MAGIC Site

On the Canary Island La Palma the Instituto de Astrofísica de Canarias (IAC) operates one of the biggest astronomical infrastructures on the northern hemisphere, the Observatorio del Roque de los Muchachos [44]. It is protected by special laws against light pollution of outside lightning caused by street lamps for example. Together with the good weather conditions, the site is well suitable for IACT observations as performed with the MAGIC telescopes.

Clouds at the Roque de los Muchachos: Especially during the summer months, clouds are very rare at the Roque de los Muchachos. The influence of the trade wind prevents the accumulation of clouds above the observatory. During the winter months, the wind and weather situation changes. Westerlies can bring clouds at all altitudes from the Atlantic ocean to the Canaries, which degrade the observation conditions [45].

The Calima weather phenomena: The Canary Islands are influenced by a weather phenomena often referred to as Calima. It is characterized by hot and dry air transporting Sahara dust. These Sahara dust events are quite regular during the summer months from July till September while wind is blowing from eastern directions. The origin of Calima events is based in the Sahara desert of Northern Africa. Large thunderstorms in these regions result in vast dust and sand storms which can extend to several kilometers of altitude. These dust layers are blown out to the Atlantic Ocean (see satellite image



Figure 3.6.: Satellite image of the Calima weather phenomenon. Dust from the Sahara is blown to the Atlantic Ocean and covers the Canary Island with a dust layer (picture taken from [47]).

Fig. 3.6) and can even reach South America under certain conditions. At the MAGIC site on La Palma the Calima layers extend approximately from 3 km to 5 km above sea level [46]. This results in a decreased optical transmission of the atmosphere.

Light of night sky: Even during the night no place on earth is absolutely dark, especially not when the sky is clean. Also during night there are many natural and artificial light sources which cause a certain amount of diffuse light, called light of the night sky (LoNS). There are several natural contributions to the LoNS. The light emission of airglow in the upper layers of the atmosphere contributes about 40 % to the LoNS. The second contribution, in the same order of magnitude is caused by the diffuse starlight. Depending on the position on the Earth and the season, there are several additional contributions like discrete starlight, moonlight, zodiacal light and lightnings as well as fluorescence light from the upper atmosphere. In most places on the Earth the human contribution, caused by exterior light which is back reflected from the atmosphere, exceeds the influence of natural sources. On La Palma due to special laws, the amount of light pollution is strictly limited. This results in an excellent astronomical sky quality with one of the lowest LoNS world-wide[38].

3.3. The MAGIC telescope's LIDAR system

The MAGIC telescope's LIDAR system is installed inside a small dome on top of the MAGIC control building, about 70 m away from both telescopes (see Fig. 3.8 (a)). The system is operated since February 2011 and allows to monitor the differential atmospheric transmission in the field of view of the MAGIC telescopes. As described in the previous Sec. 3.1, LIDAR is an active measurement technique which has the potential to interfere with the operation of the MAGIC camera system and can even disturb other optical telescopes located on the Roque de los Muchachos. These basic conditions prohibit the

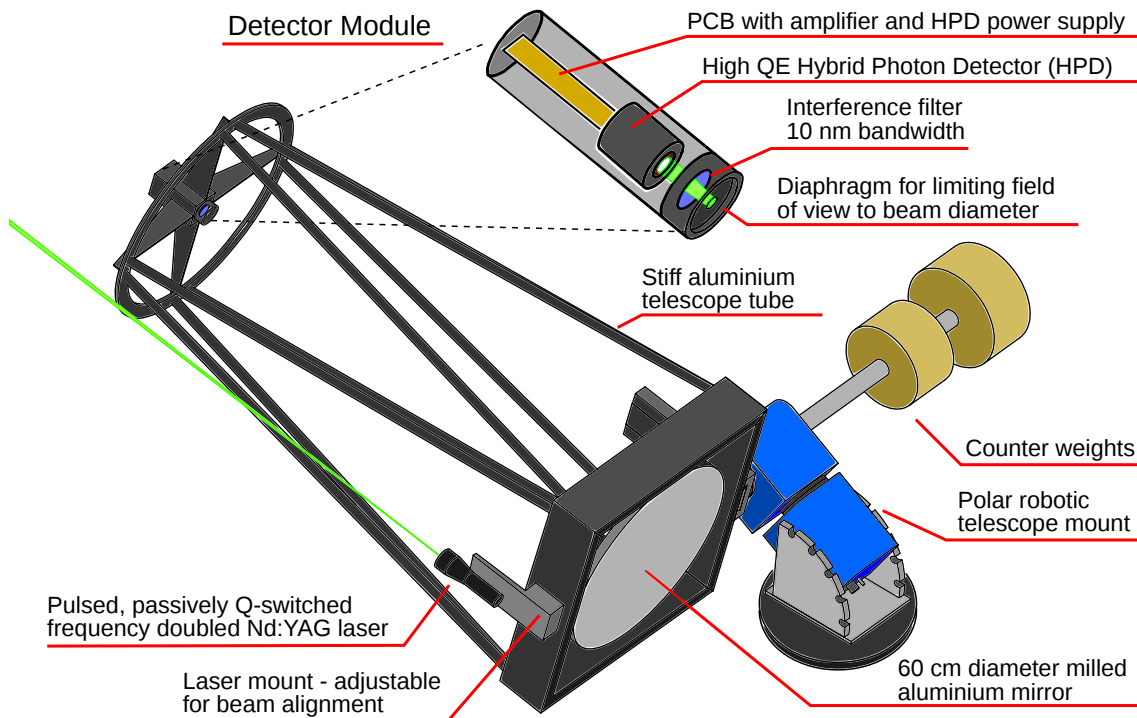


Figure 3.7.: Drawing of the MAGIC telescope's LIDAR system as it is operated since five years. The detector upgrade as it was developed in this thesis is sketched above separately (adapted from [45]).

use of commercial LIDAR systems which use powerful lasers to achieve a high accuracy. Instead, the MAGIC experiment uses a custom designed micro power LIDAR system equipped with a low power LASER with a pulse energy of $5 \mu\text{J}$. A drawing of the system is shown in Fig. 3.7 To compensate the low light intensity a sensitive detector, a hybrid photodiode, with the capability of single photon detection is used. This combination allows to measure the cloud and aerosol layer transmission with a reasonable precision while keeping the light pollution of the night sky to a minimum.

After five years of operation the LIDAR detector has proven to be a reliable system for monitoring the atmospheric conditions in the field of view of the MAGIC telescopes. Since 2014 the LIDAR data are even used to correct the MAGIC data recorded under adverse weather conditions. Thereby, the data analysis can be adapted to the current state of the atmosphere and the duty cycle of the telescopes is increased.

The following subsections introduce the most important hardware components of the MAGIC LIDAR system. They define the starting point of the LIDAR upgrade and set several limits to the specifications of a new detector.

3.3.1. LIDAR Mount and Telescope Frame

The LIDAR telescope drive system is based on the commercially available mount NTM-500 from ASTELCO [48]. It has an equatorial drive system equipped with gearless electrical

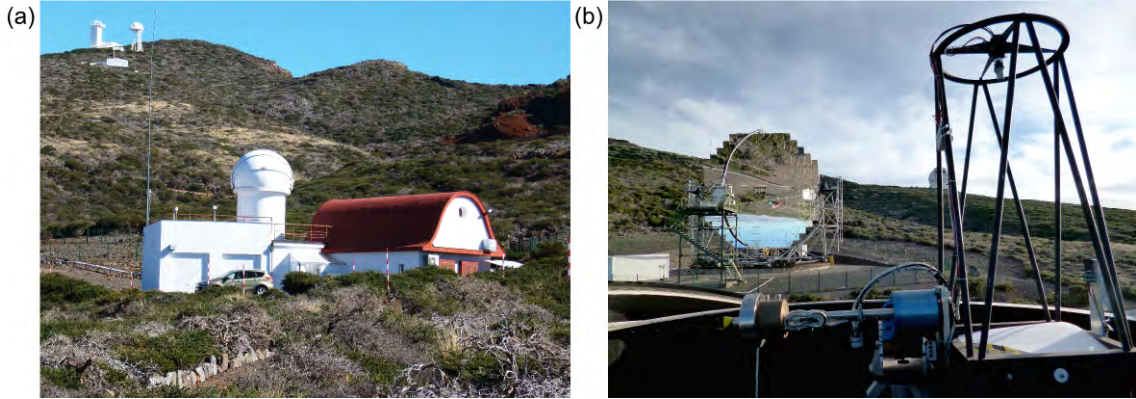


Figure 3.8.: Photograph of the LIDAR system at the MAGIC site on La Palma. (a) LIDAR tower and dome on top of the MAGIC control house. (b) LIDAR telescope frame in front of the MAGIC2 telescope. The mirror is covered to protect the detector from extensive daylight.

motors. The motor power was increased by a factor of two in order to assure a precise and fast pointing with a maximum acceleration of $20^\circ/sec^{-2}$. To ensure safety at high slewing speed and in case of power cuts, an internal pressurized brake system can stop the telescope abruptly.

The mount can carry a maximum weight of all components which is around 50 kg. Still, an accurate tracking with astronomical precision of 5" is possible. The mount is connected to an ASTELCO control unit, providing power and pressurized air for the braking system. The control unit is operated by a computer via Ethernet connection. This network interface allows to use an external computer with planetary programs to point the mount to different stars in order to adjust the pointing accuracy.

For collecting the back scattered light the LIDAR system uses an 60 cm spherical mirror with a focal length of 1.5 m. The mirror is made out of a single piece of milled aluminum, which is coated with a protective layer with a maximum reflectivity at the laser wavelength of 532 nm.

The mirror is fixed in the telescope frame with the holder for the detector module in the focus at 1.5 m. The F over d ratio of the system is 2.5 and allows a relatively compact size at a high light concentration. A photograph is shown in Fig. 3.8 (b). The laser with the beam expander optics is attached to the bottom frame of the telescope right next to the mirror.

3.3.2. LIDAR Detector Unit

The LIDAR detector is placed in an aluminum tube of 5 cm diameter which fits exactly into the support structure of the telescope frame. In front of the detector, there is an optical module, consisting of an aperture, optics for a parallel light alignment and an interference filter of 3 nm, reducing the background from the light of night sky.

The detector is installed right behind the optical module. The light detection is based on a hybrid photodiode capable of resolving 1ph.e events as well as charge integration in the

pile up region in the near field of the LIDAR. The electronic signal is amplified just behind the detector by a pre-amplifier in order to minimize the influence of possible pickup noise. The detector module hosts a DC/DC converter for the bias supply of the silicon avalanche diode inside the HPD. The high voltage for the HPD is powered by a NIM crate.

3.3.3. Data Readout and Analysis

The LIDAR control computer is a standard PC equipped with a fast analog to digital converter for data taking. It hosts additional hardware components like a TTL I/O card for communication and control of the subsystems. The whole LIDAR operation and data taking is automatized by a LabView program and runs alongside with the observations of the MAGIC telescopes [45].

3.4. Goals of the LIDAR Upgrade

During the last five years of operating the LIDAR system several problems appeared which limit the usage of the detector. At the beginning of the year 2015 the final decision for upgrading the MAGIC telescope's LIDAR system was made. The main goals of the detector upgrade are discussed in this section.

The main scientific aim of the LIDAR upgrade is to increase the measurement range of the detector, in order to extend the data corrections to large zenith angle observations above 60° . For large zenith angles the path length of the LIDAR in the Earth's atmosphere increases. The shower maximum of extended air showers is further away from the detector, like it is sketched in Fig. 3.9. To maintain the sensitivity for large zenith distance observations around the shower maximum, the range of the LIDAR needs to be extended.

Beyond the scientific upgrade, several improvements for the general operation of the system are planned. On the MAGIC site on the Roque de los Muchachos the system has to resist rather rough weather conditions. For example, the temperature can vary between -10°C during winter and around 20°C in summer. The temperature changes can be rather quick. Together with a high humidity this can cause problems for the electronics due to condensation. Therefore, all components have to be designed to be water tight. Also for the high voltage supply for the HPD of up to 8 kV special insulations and safety issues need to be considered.

The length of the detector module fixed in the focus of the mirror is desired to be shorter. This is done using a separate high voltage power supply outside the field of view of the LIDAR telescope.

On the readout side the sampling rate of the fast analog to digital converter should be increased to improve the single photon signal to noise ratio. Therefore, a new powerful computer for the LIDAR control and data processing is necessary.

All intended changes have to comply with the technical specifications of the currently used LIDAR dome as well as the size and weight limitations of the mount which are even more critical.

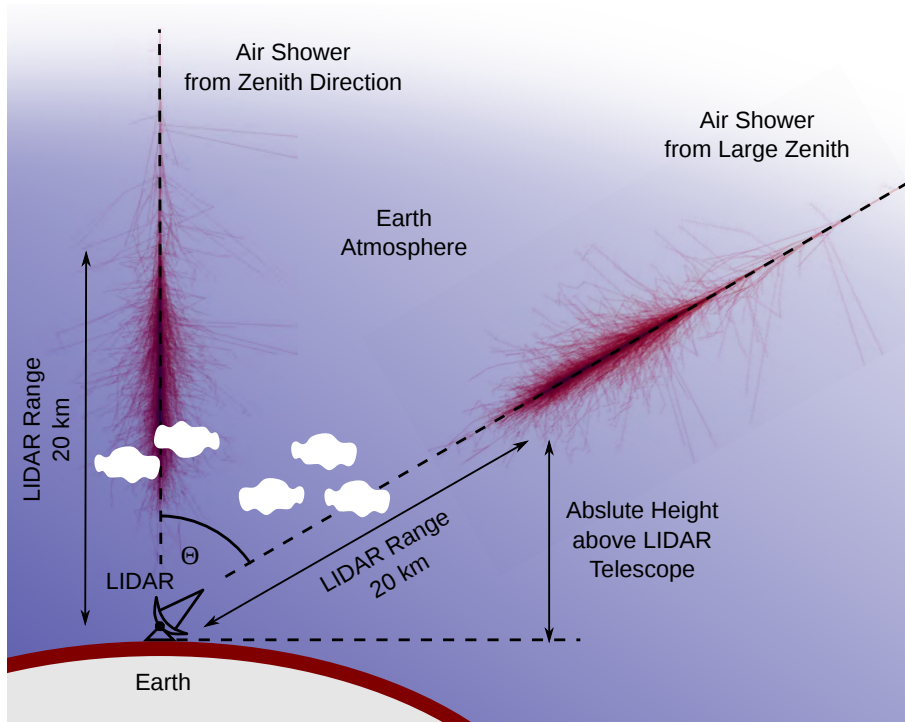


Figure 3.9.: LIDAR geometry for different zenith angle observations. The range of the LIDAR instrument is constant for all observation directions. This results in a lower absolute height range for large zenith angle observations because the shower maximum is shifted away from the detector.

3.5. Developing a new LIDAR Detector

The goals of the LIDAR upgrade were defined in the prior section. In the following subsections we will have a closer look to the technical realization of the LIDAR upgrade. Most of the components are custom designed and optimized for the operation of our LIDAR instrument. Prior to their installation on La Palma they were tested and characterized in our laboratory. The selection, development and testing of all components for an improved system performance was the second important part of this thesis.

3.5.1. High Voltage Module

The detector unit uses a hybrid photodiode for light detection (a detailed description is provided in Sec. 3.5.3). This kind of detector requires a two separate high voltage (HV) supplies providing voltages up to 500 V and -8 kV. Both voltages should be adjustable to adapt the gain of the detector according to the specifications of the readout electronics. Additionally, a real-time voltage monitoring is an attractive future for a precise gain adjustment.

For this purpose a computer controlled HV module was custom designed. It consists of two DC/DC converters which provide the HV. They are controlled by two 12-bit analog-digital-converters (ADC) and monitored by a eight channel 12-bit digital-analog-converter (DAC).

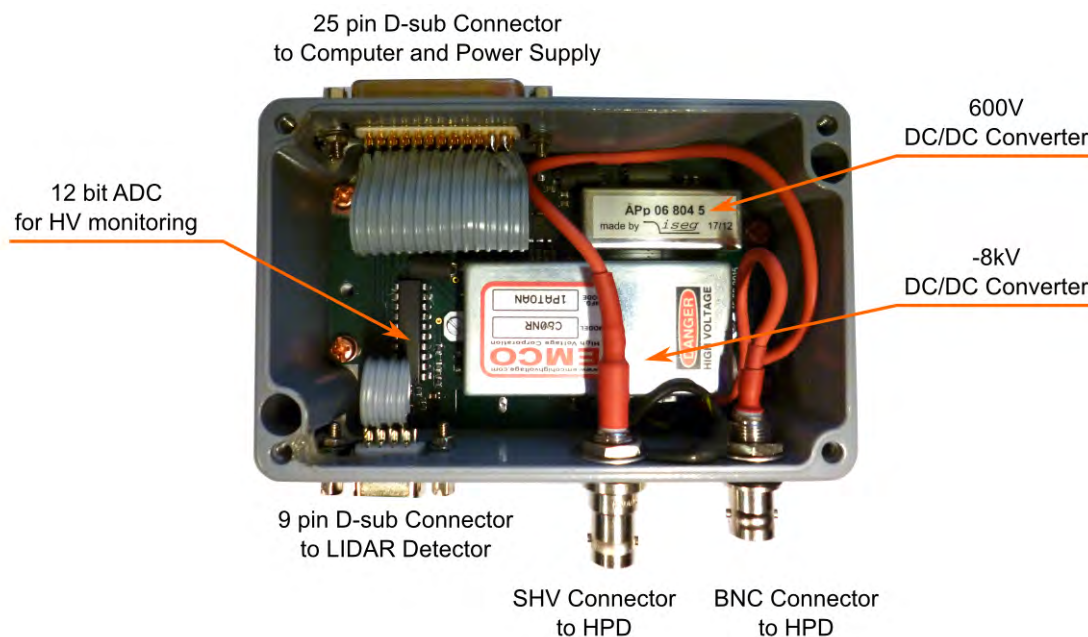


Figure 3.10.: Photograph of the high voltage module mounted in a IP66 rated box. The upper side shows the connector to the computer and power supply. On the bottom side the HV output connected to the detector is visible. All HV connections are covered with HV durable heat shrinking tubes.

A picture of the HV board mounted in a IP66 rated aluminum box is shown in Fig. 3.10. DC/DC converters are electronic devices which convert a low supply voltage into an adjustable HV output. For our relatively low voltage application up to 600 V an *iseg* DC/DC converter is used with low ripple and noise at the output. The supply voltage between 4.5 V and 5.5 V is directly provided by a computer [49]. The output voltage is controllable with an analog control voltage between 0 V and 2.5 V set by an ADC. The -8 kV are provided by an EMCO C series DC/DC converter [50]. It needs 12 V supply voltage which is provided by a NIM crate. It is controlled in a similar way as the relatively low voltage supply.

The analog control voltage for both devices is set by two Microchip DACs from MCP of the 4822 and 4922 series with 12-bit resolution. They are controlled via a serial peripheral interface (SPI) protocol. It is based on a master-slave architecture with four logic signals: serial clock (SCLK), serial data out (SDO), serial data in (SDI) and channel select (CS). The SCLK provides a periodically switching high and low signals and defines the speed of the data transmission. Via SDO the bits are sent to the device and received at the falling edge of the clock. Information send from the device are received via the SDI line. SCLK, SDO and SDI are common lines for all devices. In contrast the channel select (CS) is an individual line connected to each device. In our case, we have three CS lines for each microchip. These lines activates the device which is supposed to receive or send data setting the logic level to "low" during operation. A typical 16-bit signal transmission monitored with an oscilloscope is shown in Fig. 3.11.

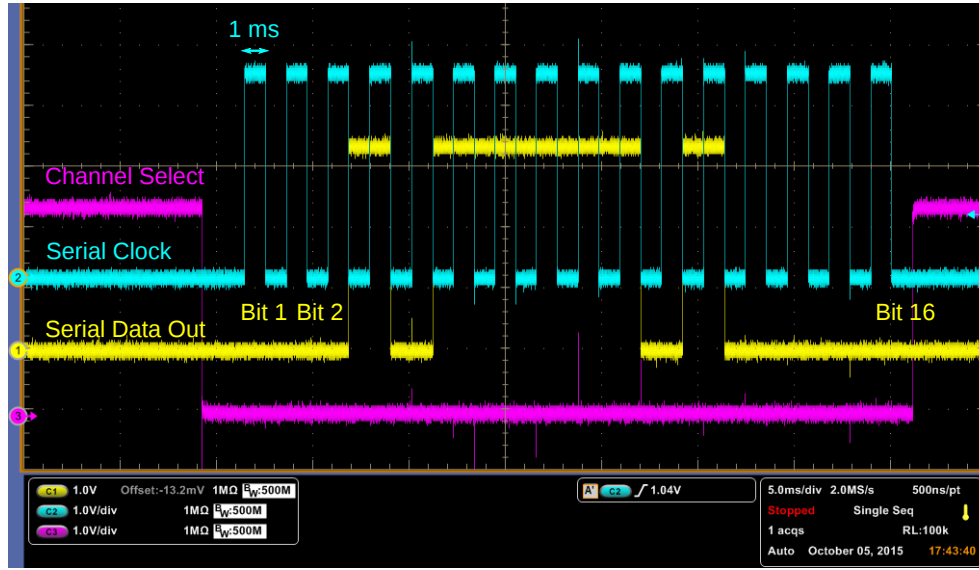


Figure 3.11.: Screen shot of the oscilloscope showing the signal scheme of the SPI protocol. The pink curve shows the channel select line which selects the device to be controlled. Setting the channel select line to zero activates the device. The bluish line is the serial clock and is switched with a frequency of 1 kHz. It defines the speed of signal transmission. The yellow curve shows the 16 bit command which is sent to control the device.

3.5.2. Detector Optics

The back reflected light from the atmosphere is collected by 60 cm spherical Aluminum mirror with an F/D ratio of 2.5 and focused onto the detector module. The module itself has some additional optics in front of the detector for background reduction and wavelength selection. At first, the light passes through an adjustable diaphragm with an aperture between 1.2 mm to 20.0 mm [51]. The diaphragm is used to limit the field of view to the size of the back reflected focused beam of the laser and thereby limits the received background light to a minimum. For further reducing the rate of background photons in the LIDAR signal, the contribution from the light of night sky has to be reduced. For this purpose an interference filter is added behind the aperture, which is only transparent for the laser light and blocks all other wavelengths of the visible light spectrum. In contrast to the prior optical module no additional optics for a parallel light alignment onto the interference filter are included in order to avoid light losses from Fresnel back reflection. Thus, the total photon detection efficiency is increased. For the choice of the interference filter one has to take into account the shift of the transmission band caused by inclined light reflected from the mirror dish. In Fig. 3.12 the optical path from the mirror through the detector optics is illustrated and the important dimensions for the following estimation of the wavelength shift are shown. The maximum shift is determined by the largest possible incident angle α

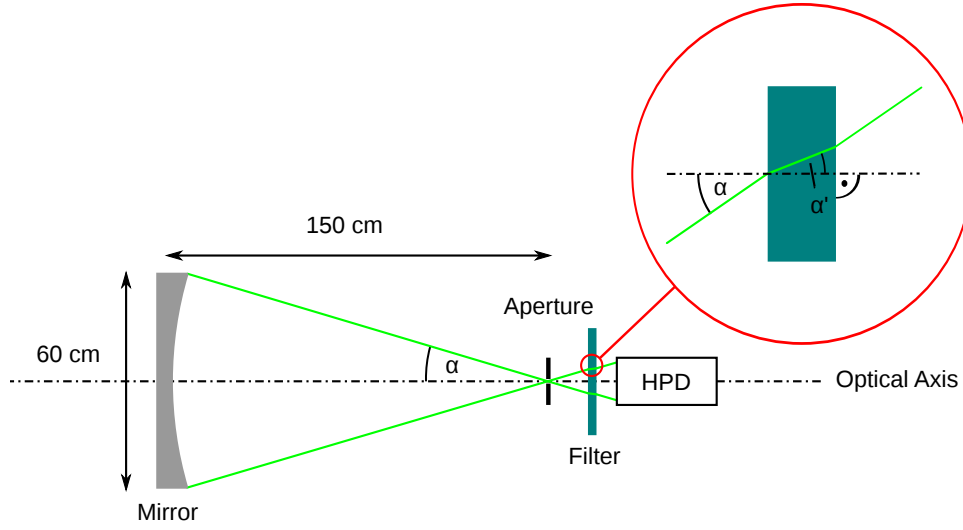


Figure 3.12.: Optical path through the LIDAR optics for parallel incident light. The spherical mirror centers the parallel light to a spot in the focal plane where the aperture is located. Right behind the aperture there is an interference filter for selecting the photons emitted from the laser and suppressing additional photons from the light of night sky. The optical path within the interference filter is depicted enlarged because it is important for the estimation of the wavelength shift.

which is specified by the radius r and focal length f of the mirror:

$$\alpha = \arctan\left(\frac{r}{f}\right) = \arctan\left(\frac{30 \text{ cm}}{150 \text{ cm}}\right) \approx 11.31^\circ \quad (3.11)$$

The angle of refraction α' inside the interference filter can be calculated by Snell's law:

$$n \cdot \sin(\alpha) = n' \cdot \sin(\alpha') \quad (3.12)$$

both angles α and α' are measured from the normal of the boundary and n is the refractive index of the respective medium. Assuming a refractive index for air of $n = 1.0$ and an index for the filter of $n' = 1.5$ which corresponds to glass, one can calculate the angle of refraction as:

$$\alpha' = \arcsin\left(\frac{n}{n'} \cdot \sin(\alpha)\right) = \arcsin\left(\frac{1.0}{1.5} \cdot \sin(11.31^\circ)\right) = 7.45^\circ \quad (3.13)$$

Assuming a layer thickness of the cavities in the interference filter of 532 nm corresponding to the laser wavelength one can calculate the maximum transmission wavelength expected under the incident angle of 7.45°:

$$\lambda' = \frac{\lambda}{\cos(\alpha')} = \frac{532 \text{ nm}}{\cos(7.45^\circ)} = 536.5 \text{ nm} \quad (3.14)$$

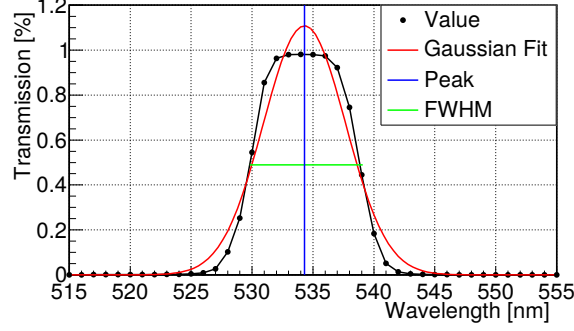


Figure 3.13.: Transmission curve of the interference filter used for background reduction. The central wavelength is 534.3 nm and the FWHM is 10.7 nm.

Now, we can calculate the maximal possible wavelength shift for the interference filter for the laser wavelength of 532 nm:

$$\Delta\lambda = \lambda' - \lambda = 536.5 \text{ nm} - 532.0 \text{ nm} = 4.5 \text{ nm} \quad (3.15)$$

This leads to following conclusion on the specifications of the interference filter: in the ideal case the filter has a central wavelength of 534.3 nm and a FWHM of 4.5 nm. The commercially available product which fitted best to our requirements is an interference filter from Edmund Optics #65-165 series [52]. It has a central wavelength of 535 nm and a FWHM of 10 nm. The large bandpass had to be chosen because the wavelength tolerance was specified with ± 2 nm. The minimum transmission is specified with 85 % and the blocking range from 200 nm to 1200 nm. We verified the specification recording a transmission curve in the lab using the quantum efficiency measurement device described in Sec. 2.4. The result is shown in Fig. 3.13. The measured results are in good agreement with the specifications provided by the manufacturer. The transmission for our range of interest is above 95 %.

Beside the suppression of background photons, the final spot size on the detector is very important. The photocathode size of the HPD is specified with 18 mm and limits the maximum spot size. The expected spot size s from the optical path is determined for a distance between diaphragm and detector of 20 mm as follows:

$$s = \frac{60 \text{ m}}{150 \text{ m}} \cdot 20 \text{ mm} = 8 \text{ mm} \quad (3.16)$$

Assuming an aperture of 5 mm of the diaphragm we end up with an expected total spot size of 13 mm at the detector. This leaves some scope for misalignment of the detector module in the telescope frame without losing light.

3.5.3. Detector Module

The LIDAR detector is based on a hybrid photodiode (HPD). We use a Hamamatsu R9792-40 HPD of compact hexagonal design. Its photograph is shown in Fig. 3.14 (a). It was developed with Hamamatsu and tested as a possible future detector for the MAGIC camera upgrade [53]. The light detection mechanism for a HPD is similar to a PMT

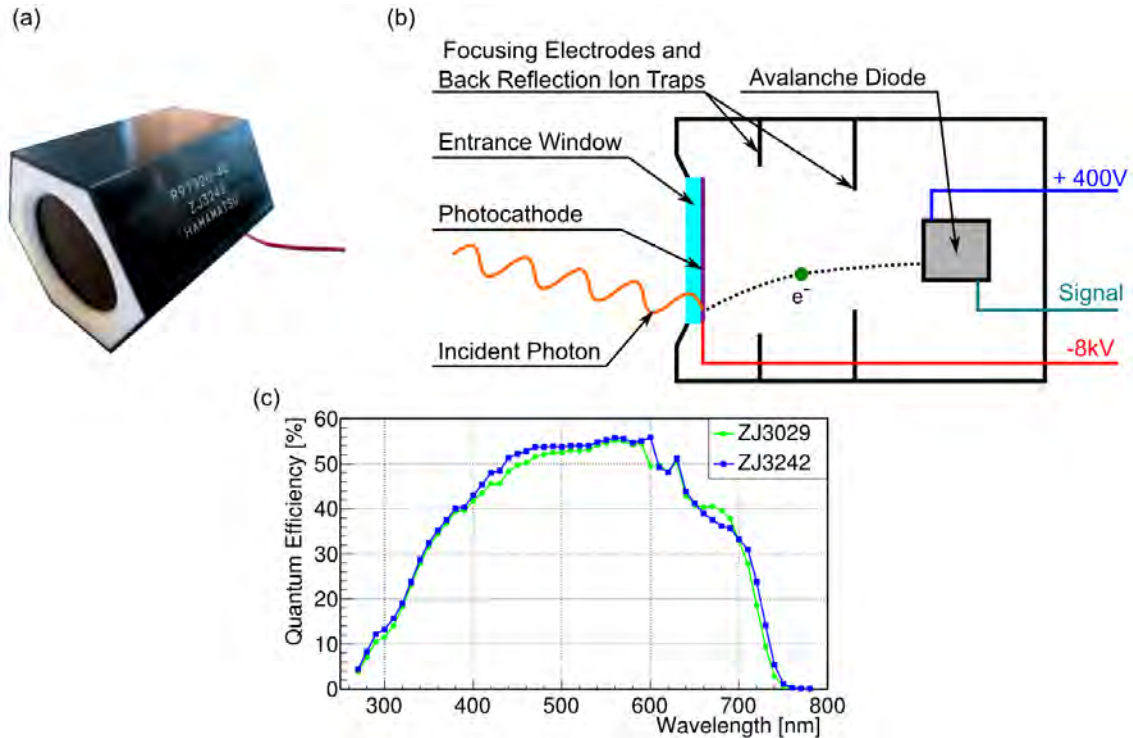


Figure 3.14.: (a) Photograph of the Hamamatsu HPD R9792-40 used for light detection. (b) Working Principle of a HPD introducing the most important components. (c) Quantum efficiency curves of two selected HPDs for the LIDAR detector with a QE above 53% at 532 nm wavelength

described in the previous chapter. A photon passes through the entrance window and releases a photoelectron (ph.e) from the photocathode (see Fig. 3.14 (b)). The Hamamatsu HPD has a GaAsP photocathode of a round shape with a diameter of 18 mm. Its peak QE reaches values up to 54%. The QE curves provided by the manufacturer of the two selected HPDs for the LIDAR detector are shown in Fig. 3.14 (c).

The main difference to a PMT is the charge amplification which is based on a two stage process in a HPD. In the first stage, the released photoelectrons are accelerated towards the anode by a high intensity electric field of a few kilovolts applied to the photocathode. The avalanche diode (AD) has a cylindrical shape with a diameter of 3 mm. Thus, additional focusing electrodes are needed to guide the photoelectrons to the right position. The photoelectrons bombard the AD and produce electron-hole pairs in the Si depleted layer according to their initial energy. This gain is dependent on the accelerating high voltage applied to the photocathode and called electron bombardment gain [54]. It reaches a maximum value for a voltage of -8 kV of around 1500. In the second stage, the secondary electrons inside the AD are subsequently accelerated in the high electric field of the pn-structure and create an avalanche by impact ionization. The AD is operated in a reverse bias mode and the so-called avalanche gain is in the order of 30 to 100 depending on the applied voltage [55]. This results in a total operational gain of up to 150 000.

In contrast to the PMTs discussed in the previous chapter, the HPDs do not use a



Figure 3.15.: Screenshot of the oscilloscope showing the HPD signal after amplification with a differential amplifier. For the measurement the gain of the HPD was set to the maximum by applying a high voltage of 8 kV and a bias voltage of 428 V to the diode. The tested HPD can resolve six different photoelectron peaks. Right after the signal there is a small undershoot visible which is caused by the amplifier. The pulse width is about 2.3 ns at FWHM for each pulse, independent from the intensity. The arrival time of both amplifier is in good coincidence.

multiple dynode system for charge amplification. Thus, the statistical error of the charge amplification is reduced because of the very high gain of 1500 of the first acceleration stage. As a rule of thumb one expects a relative fluctuation of $\sqrt{1500}/1500 \approx 2.5\%$. This is much smaller compared to fluctuations of about 35% for PMTs. This results in significantly reduced gain fluctuations and produces a pulse height distribution with separate multi photoelectron peaks. A screenshot of such a measurement is shown in Fig. 3.15. Six separate peaks are visible and light flashes between one and six photoelectrons are distinguishable. For the measurement the HPD is illuminated with weak laser shots of approximately 1ph.e per pulse and runs with the maximum gain of around 150 000. Despite the high internal gain of the HPD, further amplification is needed to transport the signal over larger distances and for processing. The detector in the LIDAR telescope is connected to the readout electronics via a 10 m SMA cable. In order to decrease the pickup noise we decided to use a differential amplifier. In order to design the amplifier we need to estimate the current produced by the HPD. We can assume a maximum charge amplification for 1ph.e of 150 000 and a typical pulse width of 2.3 ns from the HPD. This results in the following current produced by the HPD:

$$I = \frac{Q}{t} = \frac{e \cdot gain}{t} = \frac{1.6022 \cdot 10^{-19} C \cdot 150\,000}{2.3\,ns} \approx 10,4\,\mu A \quad (3.17)$$

For a typical 50 Ω termination this results in a voltage of 520 μV . To reach an adequate signal to noise ratio after the amplifier, we need a gain of at least four to reach a signal of

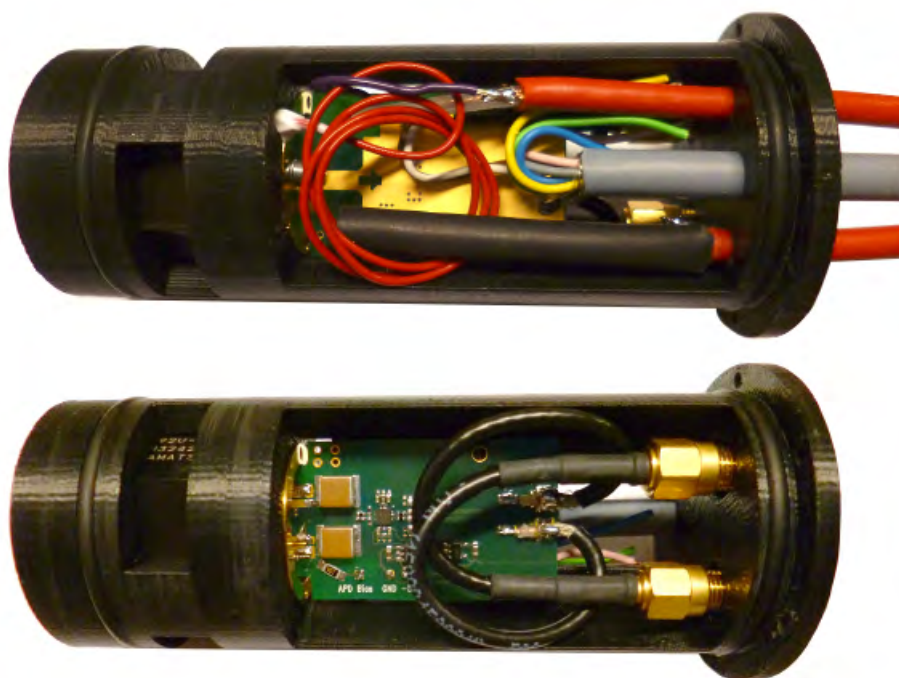


Figure 3.16.: Photograph of the LIDAR detector module showing the amplifier board.

about 2 mV. For this purpose a Texas Instruments LMH6554 differential amplifier is used. The feedback resistor is set to $390\ \Omega$ for the required gain [56]. It provides the necessary signal bandwidth for up to 16-bit high-speed signal acquisition. The circuit diagram of the amplifier is shown in the appendix. The measurements of the final signal shape is shown in Fig. 3.15. The amplifier causes a small undershoot right after the signal but does not degrade the pulse width of 2.3 ns.

The whole detector module is placed inside a 5.0 cm diameter aluminum tube. An additional support structure is needed to fix all components in the right place. A 3D printed plastic module was designed to hold the HPD and the amplifier board behind. It also includes an end cover for the aluminum tube with feed throughs for the HV cables. A photograph of the detector module is shown in Fig. 3.16.

3.5.4. Transmitter Unit

The LIDAR transmitter module consists of a 532 nm laser and a $20\times$ beam expander mounted onto a custom designed bench which is adjustable around two axis. A photograph of the module is shown in Fig. 3.17.

The light source is a diode pumped, passively Q-switched, frequency doubled Nd:YAG laser with a pulse duration of 600 ps provided by the company Horus Laser [57]. The repetition rate is up to 1 kHz and the pulse energy is specified with $25\ \mu\text{J}$. The laser head is connected to a laser controller which is hosted in a separate box. The control electronics handle the active temperature stabilization of the laser crystal as well as the trigger logic.



Figure 3.17.: Photograph of the transmitter unit of the LIDAR system. It consist of a 532 nm laser and a 20× beam expander mounted onto a custom made bench revolvable around two axis for the light beam adjustment.

For our application we initialize the pulse generation with an external 3.8 V TTL pulse generated by the TTL I/O card of the LIDAR computer. The laser has an embedded photodiode creating a second trigger signal simultaneously to the light emission which is used to activate the data acquisition of the FADC card. The laser is combined with a 20× beam expander from ThorLabs in order to decrease the beam divergence and to reduce the light flux density in the near field for the reason of eye safety.

We tested the performance of the laser in the lab. During the first evaluation of the spot size and divergence we recognized a strange behavior of the emitted light. The laser was pointed to a diffuse reflecting wall in a distance of 5,8 m. The spot shape was recorded with a commercial digital camera for three different laser firing frequencies. The results are shown in Fig. 3.18 (b). In all photographs an additional artifact is visible right below the main spot. It seems to be a second light mode generated by some reflection in the laser cavity. The light intensity of the artifact was measured using a PIN photodiode which roughly makes 3% of the total light flux.

An important parameter of the laser is the beam divergence. It can be estimated measuring the beam diameter at two different distances as shown in Fig. 3.18 (a). Now, we can calculate the beam divergence ϕ from simple geometrical considerations:

$$\phi = \arctan \left(\frac{d_2 - d_1}{2 \cdot l} \right) \quad (3.18)$$

where d_1 and d_2 are the spot diameters at two different positions separated by the distance l . The beam divergence without any expander optics is determined with $\phi = 0.32^\circ$ for a pulse frequency of 300 Hz and is confirmed by the measurements of the manufacturer.

Besides the beam shape we also verified the beam energy. For the measurement, we use a calibrated PIN diode with a quantum efficiency of 68% at the laser wavelength of 532 nm. Despite the high sensitivity range of a PIN diode the light flux from the laser is to high for a direct measurement. Thus, a neutral density filter with an optical density of 4.0 which corresponds to a transmission of 0.01% is placed in the beam line between laser and PIN diode. The measured current on the PIN diode for different frequencies is shown in

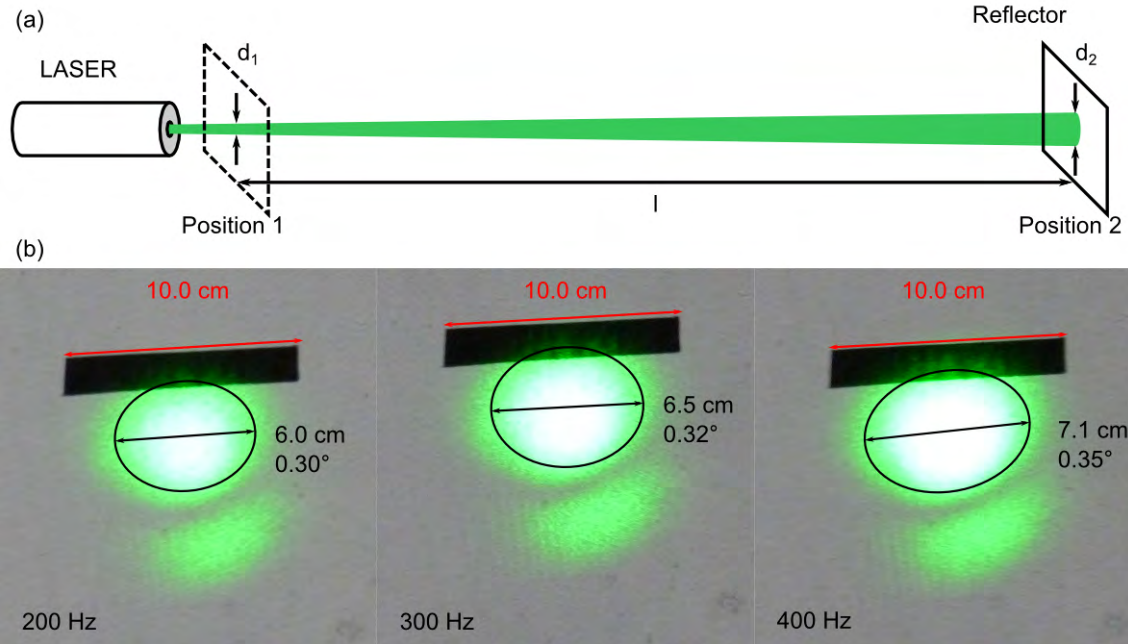


Figure 3.18.: (a) Measurement setup for the laser beam divergence. The visible spot size is measured at two different distances on a diffuse reflector with respect to the laser position. (b) Diffuse reflected laser spot at a distance of 5,8 m recorded with a digital camera.

Fig. 3.19 (a). Starting from the current I we can calculate the number of electrons N_{phe} released in the diode per laser pulse :

$$N_{phe} = \frac{I}{\nu \cdot e} \quad (3.19)$$

where ν is the laser frequency and e the elementary charge. Now we can calculate the pulse energy E per shot from the number of photons N_{phot} and their energy E_{phot} :

$$E = N_{phot} \cdot E_{phot} = \frac{N_{phe}}{QE} \cdot \frac{h \cdot c}{\lambda} \quad (3.20)$$

QE is the quantum efficiency of the PIN diode, h is the Planck constant, c is the speed of light and λ is the wavelength of the lase. The results for a frequency range between 100 Hz and 700 Hz are shown in Fig. 3.19 (b). Unfortunately, the beam energy fluctuates quite a lot between 29 μ J and 34 μ J with different laser firing frequencies. The energy measured with the 20 \times beam expander in the optical path is not corrected for light losses in the beam expander. Thus, the calculated pulse energy is lower. To correct for this effect, the transmission of the beam expander has to be evaluated in more detail.

Due to the poor spot size the laser will be sent back to the manufacturer for a new calibration. Thus, the transmitter unit could not be tested yet under real operation conditions at La Palma.

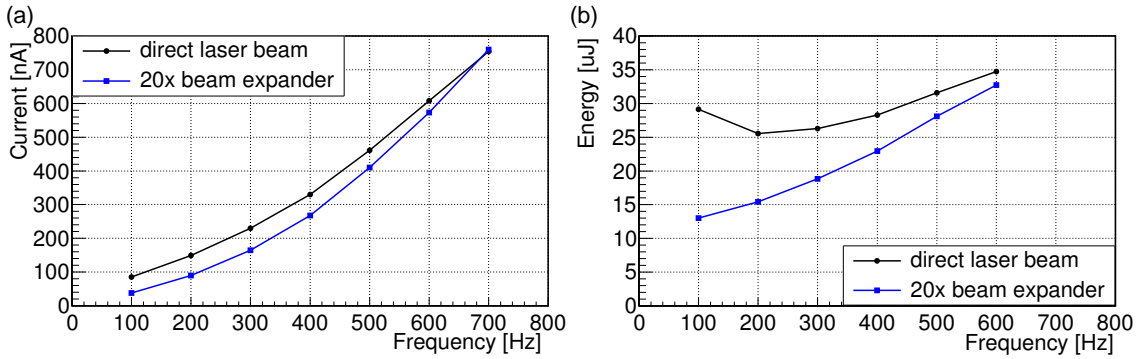


Figure 3.19.: Laser pulse energy. (a) Current measured on the PIN diode for different pulse frequencies. (b) Corresponding pulse energy. The pulse energy with the 20× beam expander is lower because losses caused by the expander optics are not taken into account.

3.5.5. LIDAR Computer

The whole LIDAR system is controlled from a computer in the LIDAR control room in the tower of the MAGIC control house. The LIDAR computer is a standard PC equipped with some additional hardware components for communication and controlling of all the subsystems. The data are recorded by a fast analog to digital converter (FADC) and temporarily stored in the computer memory for analysis. Thus, the requirements on the hardware are quite demanding. The most important components are shown in the following.

CPU: The computer is run by a IntelCore i5-4460 processor with four 3.2 GHz cores. The high computation power is needed to analyze the recorded data in a reasonable time of around 60 s.

Random Access Memory (RAM): For a temporary storage of the recorded data around 14 GB of memory has to be allocated. Thus, a reasonable amount of RAM has to be provided. At the moment, a 16 GB Crucial Ballistix 1600 MHz RAM kit is installed. For the future, it is possible to extend the RAM to 32 GB in order to analyze a larger amount of data.

Hard Drives: The PC is equipped with two separate hard drives. A 250 GB solid state drive from Samsung 850 EVO series is used for a fast boot and hosts all programs for the LIDAR control. The analyzed LIDAR data are stored on a classical 4 TB Western Digital hard disc drive.

FADC card: The data acquisition is handled by a Spectrum M4i.4450-x8 FADC card [58]. The card is based on a PCI Express x8 platform and directly connected to the main board. The FADC has two active channels with 14-bit resolution and a sampling rate of 500 MS/sec. The voltage range for each channel is ± 500 mV. The card is externally triggered by the photodiode of the laser. The FADC is operated in a so-called FIFO (first in first out) mode for a continuous data transfer to PC memory. More than 14 GB of data are recorded in less than 60 sec

TTL I/O card: For the hardware communication to the subsystems the computer hosts a Quacom PCITTL32IO card. It provides 32 TTL I/O channels which can be operated in read or write mode in blocks of eight channels. Communication with the LIDAR dome, the HV box and the trigger of the laser are managed using this card.

Serial Interface: A LogiLink PC0031 serial interface with two serial connectors is used for communication with the laser controller and the NIM crate.

Ethernet card: For communication with the mount controller an additional Ethernet module is needed in order to provide two separate network connections.

At the beginning of this work the attempt to use Linux as operating system was made to adapt to the MAGIC control systems. This was not possible, due to reduced availability of Linux drivers for several subsystems like the telescope mount. Finally, we decided to use Microsoft Windows 7 as operating system for the LIDAR computer. This update was necessary because the support for the old Windows XP system ended 2014. The new operating system made several smaller and larger changes of the control software necessary in order to get the whole system operational again.

3.5.6. LIDAR Control Software and LabVIEW Programm

Major parts of the LIDAR control and analysis software were developed in the scope of a previous PhD thesis [45]. The main work of this thesis was to adapt this software to the new hardware, like the HV module and especially the dual channel data acquisition ¹ The software can be divided into two parts.

The first one handles the data acquisition and analysis and consists of several C++ programs. There are several small peaces of software which handle the communication via the TTL I/O card in order to open the dome, to set the voltage in the HV module or to readout data from subsystems. The main data acquisition program communicates with the FADC card. It sets the card's specific setup parameters and fires the selected number of laser shots. After each shot the program waits for the trigger of the laser diode and starts the data transfer from the FADC to memory. Afterwards, the individual signals are analyzed and by a photon counting algorithm. Finally, the number of photon counts per range bin is saved to hard disc together with some additional information of the measurement.

The second part of the software is the LIDAR control and monitoring which is implemented using LabView. It provides a user interface for a quick and intuitive LIDAR operation (a screenshot is shown in Fig. 3.20). Several safety checks and automatic routines are added to simplify the operation. The software consists of several subprograms which are responsible for dome, mount, HV and laser control.

During this thesis the HV module was integrated into the system allowing to set and monitor the detector supply voltages. The goal of the new subprogram was to adjust the HV supply in a way to keep the 1ph.e charge of the HPD constant. For this purpose a constant monitoring of the dark count rate is implemented which gives the feedback for the HV adjustment.

¹The software development was done together with Dr. Christian Fruck who is in charge of the MAGIC telescope's LIDAR system.

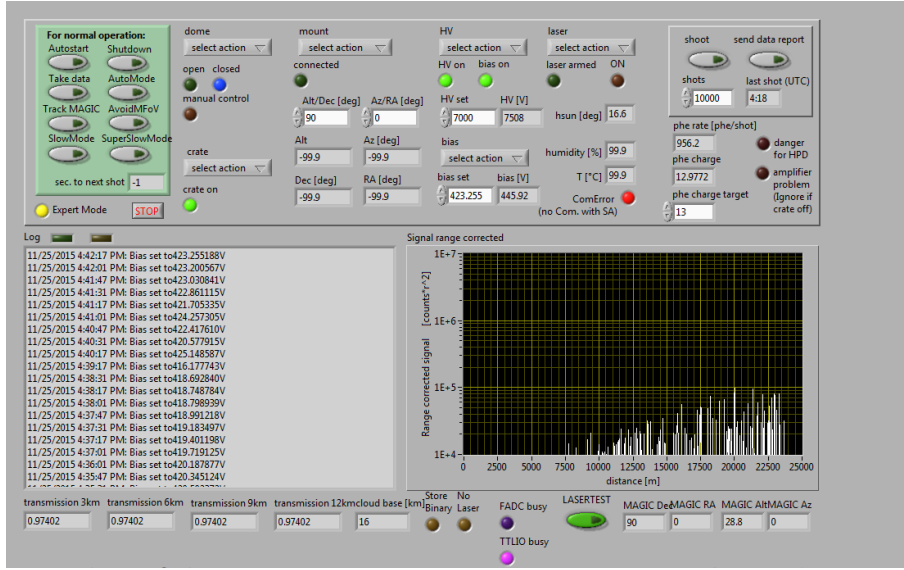


Figure 3.20.: Screenshot of the LIDAR LabView control panel as it is used for daily operation of the LIDAR system.

3.6. Examining the Transmission of the Earth’s Atmosphere

The new detector module and the readout electronics were sent to La Palma in the second half of November 2015. They were installed in the LIDAR telescope and the LIDAR control room during the moon break of the MAGIC observations. Thus, the observations of the telescopes were not affected. After the successful installation test operations started. This section will present the first measurement results under real conditions on the MAGIC site at the Roque de los Muchachos.

3.6.1. Single Photoelectron Distribution

One of the goals of the new HV module is to provide a precise voltage adjustment. Thereby, the 1ph.e charge of the impinging photons can be set and monitored. This allows to adapt the voltage to temperature and humidity changes and to keep the 1ph.e charge constant during all measurements. The 1ph.e monitoring is controlled by a C++ program called ”background” (for the source code see A.2.1). For data acquisition we set the FADC card to a software-trigger mode and acquire 500 waveforms with background photons. In the data we search for 1ph.e events using following criterion:

$$V_i > 2\text{ mV} \quad \cap \quad V_{i+1} < V_i \quad (3.21)$$

Here we set a threshold voltage of 2 mV for 1ph.e events and check if the next data point is smaller than the previous one in order to identify the peak. Afterwards, the charge ² of

²The charge is again specified in units of Vs and includes the transimpedance gain of the amplifier. Using this definition the 1ph.e charge corresponds to the area under the voltage signal peak. One would need to divide through the transimpedance gain to obtain the physical charge.

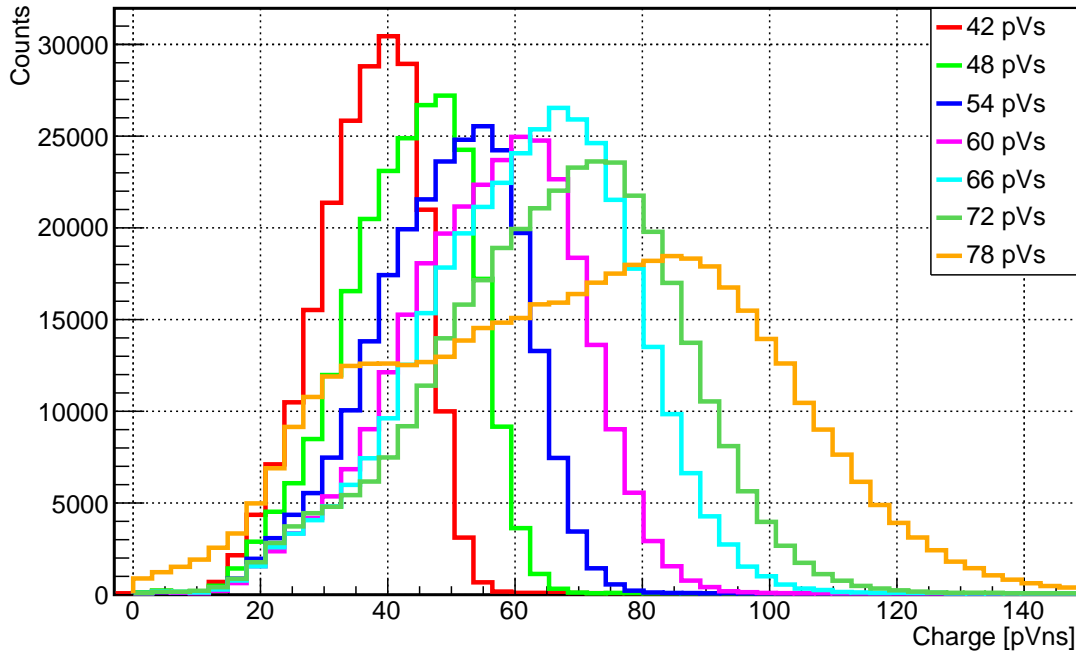


Figure 3.21.: 1ph.e charge distribution of the HPD with different preselected 1ph.e charges. A higher 1ph.e charge corresponds to a higher internal amplification of the photoelectrons in the HPD. At a charge of 78 pVs the HPD breaks through.

1ph.e is determined by integration:

$$Q_{\text{ph.e}} = (V_{i-1} + V_i + V_{i+1}) \cdot 6 \text{ ns} \quad (3.22)$$

Afterwards the 1ph.e charge of the HPD is stored in a histogram and the average 1ph.e charge is calculated. To select the optimal 1ph.e charge for operation we recorded histograms for different preselected 1ph.e charges shown in Fig. 3.21. A higher 1ph.e charge corresponds to a higher internal amplification of the photoelectrons in the HPD which is preferable for 1ph.e detection. The HPD shows a breakthrough at 78 pVs. Thus, we choose an average 1ph.e charge of 66 pVs for operation.

After selecting the 1ph.e charge, the LIDAR LabView control adjusts the voltage until the selected value has stabilized. It is followed by a continuous monitoring of the 1ph.e charge every 5 s as long as no other data acquisition is running.

The average 1ph.e charge is used in the pile-up region of the signal for calculating the number of 1ph.e events. This is described in more detail in the next section.

3.6.2. LIDAR Detector Raw Data

One of the first tests on La Palma for evaluation the performance of the new detector was to acquire a single LIDAR shot. It is the basis for all further measurements. We record data for 164 μs including 5 μs of pre-trigger data. This results in a maximum distance of about 24 km above the telescope for atmospheric monitoring. The raw data of a single LIDAR shot after subtraction of both amplifier channels are shown in Fig. 3.22. The whole

signal range can be divided into three regions: the pre-trigger region, a near and a far field region. The pre-trigger region before the laser pulse contains background photoelectrons from the light of night sky. It is used to determine the background photoelectron counts that are subtracted from the signal. The backscattered light is completely contained in the post-trigger region. The near field region extends from $5 \mu\text{s}$ to $25 \mu\text{s}$ and is characterized by a high signal amplitude. In this region 1ph.e are detected with high rates at which pile-up of the 1ph.e pulses occurs. Thus, 1ph.e counting is not possible in this region and we need to use a charge integration method (see Fig. 3.22(b)). In the far field region 1ph.e events are resolved separately (see Fig. 3.22(c)) and have a typical size of about 6 mV . Compared to the noise level of around 0.3 mV root mean square and a ripple of 100 MHz this is large enough to ensure a reliable detection. A 1ph.e counting algorithm is used which provides a better background rejection. For 1phe events after $130 \mu\text{s}$ which corresponds to a range of 20 km the detector reaches the noise limit of the system. This has slight improvement compared to the old detector system. The noise limit is mainly determined by the low-power laser used for this test. Using a stronger laser will shift this limit to a higher range.

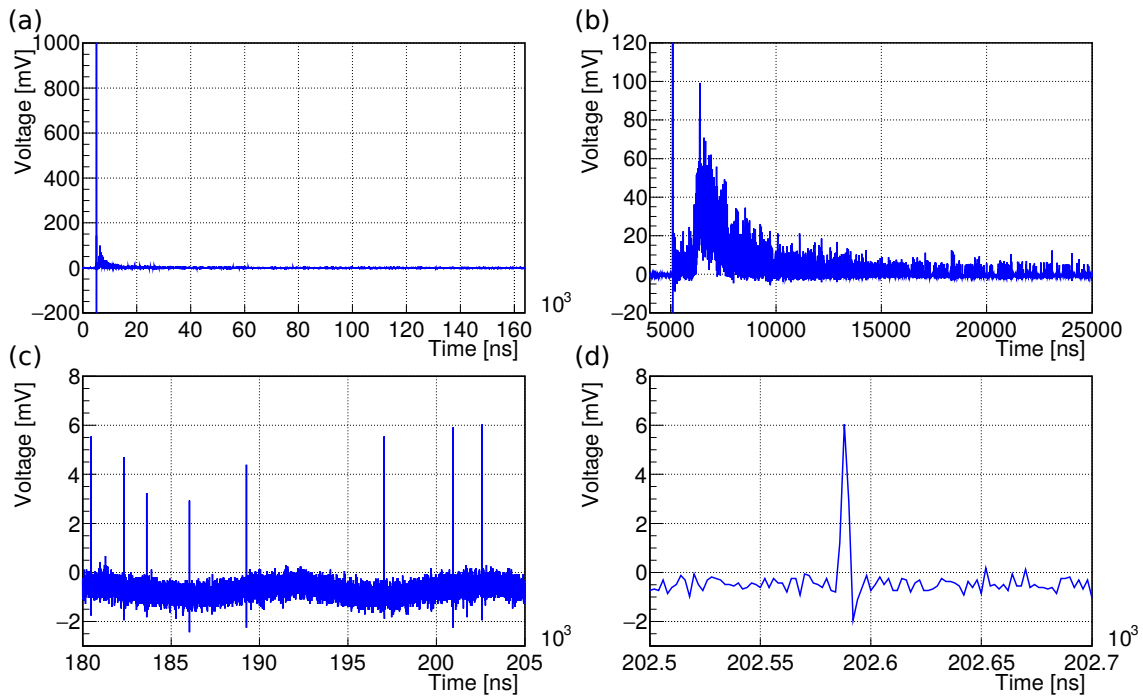


Figure 3.22.: LIDAR raw data of a single LIDAR shot acquired with the FADC card. (a) Full waveform of a single measurement. (b) Near field region with charge pile-up where a charge integration analysis needs to be applied. (c) Sample of the far field region with several 1ph.e events where the photon counting algorithm is applied. (d) Close up of a 1ph.e event showing the signal shape.

3.6.3. Typical LIDAR Return Signal

The LIDAR return signal is already described in Sec. 3.1 introducing the single scattering LIDAR equation (Eq. 3.7). In this form, the formula shows a strong dependence on the square of the distance from the detector, which does not carry any physical information. Therefore, it is convenient to introduce the so called range corrected LIDAR return:

$$S(r) = \frac{dN(r)}{dr} \cdot r^2 = N_0 \cdot \eta \cdot A \cdot O(r) \cdot \beta(r) \cdot \exp\left(-2 \int_0^r \alpha(r') dr'\right) \quad (3.23)$$

This number is calculated from the raw data in form of photon counts per bins of 48 m distance. Interpretation of the LIDAR return becomes easier with logarithmic scaling on the y-axis. Data examples of two different clouds acquired during the test on the MAGIC site on La Palma in November 2015 are shown in Fig. 3.23. The error bars of the data sets show that up to a range of 20 km the LIDAR signal is very reliable. Above 20 km the noise limit of the detector is reached and the error bars become large.

Already from the range corrected LIDAR return a qualitative analysis of the atmosphere is possible. Both plots in Fig. 3.23 show the presence of different cloud layers above the telescope. Determining the position of the maximum of the LIDAR return gives a first information about the distance of the cloud layer. Knowing the zenith angle of the observation one can calculate the height of the cloud layer above ground.

For a more quantitative analysis a closer look to the range corrected LIDAR return is necessary. The LIDAR equation can be transformed into a mathematically more elegant form if the exponential dependence is absorbed into a signal function $\Sigma(r)$:

$$\begin{aligned} \Sigma(r) &= \ln\left(\frac{N(r)}{dr} \cdot r^2\right) = \\ &= \ln(N_0 \cdot \eta \cdot A \cdot O(r)) + \ln(\beta(r)) - 2 \int_0^r \alpha(r') dr' \end{aligned} \quad (3.24)$$

In a final step, the constants and the integral can be removed by differentiation with r

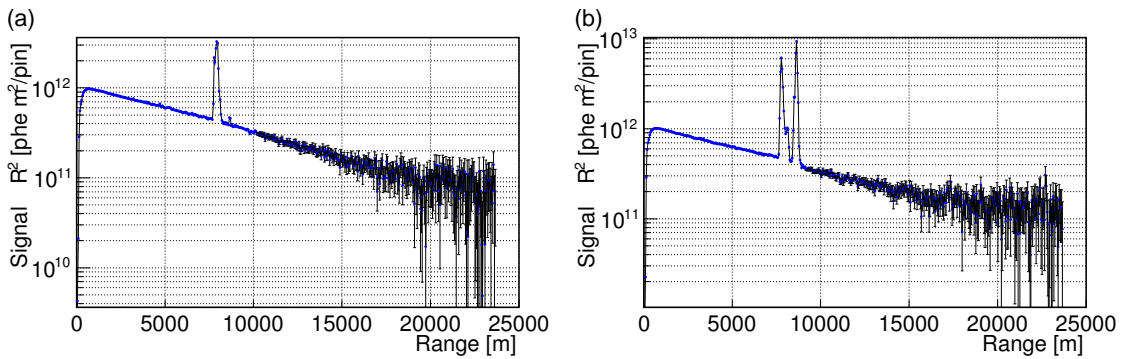


Figure 3.23.: Range corrected LIDAR return. (a) Single cloud layer at the distance of about 8000 m. (b) Larger cloud structure with to layer in the range between 7000 m and 8800 m from the LIDAR instrument.

what reveals the basic structure of the differential equation:

$$\frac{d\Sigma(r)}{dr} = \frac{1}{\beta(r)} \frac{d\beta(r)}{dr} - 2 \cdot \alpha \quad (3.25)$$

Now, the main problem of the signal analysis becomes clear. In the most general case the backscattering coefficient $\beta(r)$ and the extinction coefficient $\alpha(r)$ are independent from each other, which makes it impossible to invert the LIDAR return analytically. Therefore, additional informations are necessary which are based on assumptions for special cases described in the next section.

3.6.4. Analyzing the Transmission of Clouds

For analyzing the signals recorded with the MAGIC telescope's LIDAR system a specialized algorithm has to be used. All established signal inversion algorithms like the Klett method [59] can not be used without additional assumptions. A specialized method for the MAGIC LIDAR system was developed in prior works by C. Fruck [38], [45]. It uses a clear air model and has only one free parameter. The detailed procedure and the assumptions are described in the following.

In regions with clear air, Rayleigh scattering is dominant at a wavelength of 532 nm which leads to a very close to exponentially decreasing value of the LIDAR return $S(r)$. This is based on two effects. The first and most important one, is due to the density profile of the atmosphere described by the barometric formula in Eq. 3.8. The altitude dependence of the temperature in the atmosphere results in a larger scale height for lower temperatures. The second effect is based on the light attenuation by the total Rayleigh scattering cross-section, which results in an exponential decay of the light intensity, too. Due to the high transparency of air at the wavelength of 532 nm this effects and multiple scattering can be neglected. As a result clear air regions appear as straight lines in the semi-logarithmic scaled plot of the range corrected LIDAR signal (see Fig. 3.24(a)). These assumptions are used to fit a clear air Rayleigh barometric density model S_{mol} with a sliding window to selected regions:

$$S_{\text{mol}}(r) = C \cdot \exp\left(\frac{r}{r_c}\right) = C \cdot \exp\left(\frac{r \cdot \cos(\theta_z)}{h_c}\right) \quad (3.26)$$

C is the scaling factor and r_c is the exponential scaling factor. The range dependence can be converted into a real altitude $h = r \cdot \cos(\theta_z)$ taking into account the zenith angle θ_z of the observation. In this case, h_c is the scale height of the barometric height formula (see Eq. 3.8).

In a low altitude region in between 3.5 km and 6.0 km distance from the detector we search for a best fit. The minimum value of χ^2/N_{df} is used to identify the best fit with N_{df} being the number of points included into the fit. The best results are obtained using a sliding window with the size of 500 m. From this clear air fit, the exponential scaling factor r_c is fixed for the further analysis.

The detection of cloud layers is based on two fits before and after the cloud layer. The fit functions used for this have only one free parameter, the scaling factor C of the molecular model. The beginning of the cloud layer is detected if the value χ^2/N_{df} exceeds 2.0. The

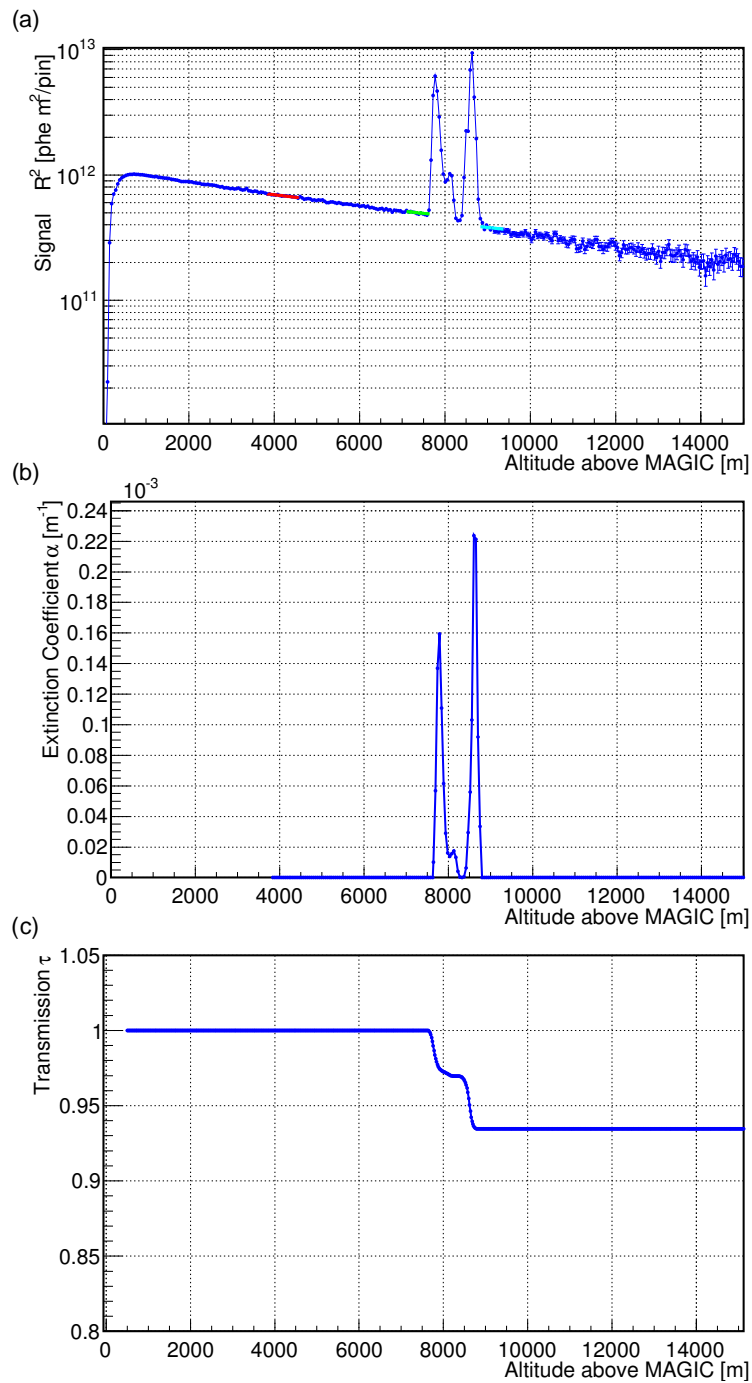


Figure 3.24.: Analyzing the cloud transmission from LIDAR measurements. (a) Clouds are detected fitting a clear air Rayleigh model to the range corrected LIDAR return signal. (b) The extinction coefficient is estimated by normalizing the backscattering access of the cloud to the total extinction. (c) The altitude dependent transmission is calculated by integrating the extinction coefficient.

end of the cloud layer is defined by: $\chi^2/N_{df} < 1.0$. As a result, the algorithm provides two constants: the scaling factor of the pre-cloud fit C_1 and the one of the post-cloud fit C_2 (see Fig. 3.24 (a)). The pre-cloud value C_1 should always be higher than the post-cloud one C_2 . The decrease reflects the light attenuation inside the cloud layer. Additionally, one can assume that laser light which is Rayleigh scattered behind the cloud layer is attenuated with the square of the layer's transmission:

$$C_2 = C_1 \cdot \tau_{\text{aer}}^2 \quad (3.27)$$

Now the transmission of any cloud can be calculated using the scaling constant of two clean-air fits before and after the cloud layer:

$$\tau_{\text{aer}} = \sqrt{\frac{C_2}{C_1}} \quad (3.28)$$

For more detailed information about the cloud layer, the extinction coefficient α_{cloud} has to be extracted from the LIDAR return. For this purpose, the contribution from clear-air Rayleigh scattering has to be subtracted. In the cloud layer, the mean Rayleigh contribution can be estimated from the clear-air fit before and after the cloud layer:

$$\bar{S}_{\text{mol}}(h) = \frac{C_1 + C_2}{2} \cdot \exp\left(\frac{h}{h_c}\right) \quad (3.29)$$

The extinction coefficient is calculated from the LIDAR return $S(h)$ by distributing the total extinction to the magnitude of the cloud backscattering excess:

$$\alpha_{\text{aer}}(h) = \sqrt{\frac{C_1}{C_2}} \cdot \frac{S(h) - \bar{S}_{\text{mol}}(h)}{\int_{h_1}^{h_2} (S(h) - \bar{S}_{\text{mol}}(h))} \quad (3.30)$$

The calculation is demonstrated on a real data example with a two layer cloud structure in Fig. 3.24(b).

For finally correcting energy spectra of very high energy gamma ray sources, it is useful to calculate the integral cloud transmission to the ground as a function of the altitude:

$$\tau_{\text{aer}}(h) = \int_{h_0}^h \alpha_{\text{aer}}(h') dh' \quad (3.31)$$

The integral transmission curve of a two layer cloud structure is shown in Fig. 3.24(c). It provides a quantitative analysis of the atmospheric transmission in the field of view of the MAGIC telescopes and contains useful information about the influence on the data quality.

4. Conclusion and Outlook

During this Master's thesis three different samples of PMTs were evaluated for studying their performance and for the decision concerning the CTA camera system. The PMTs are produced by the companies Hamamatsu Photonis K.K. and ET Enterprises that started about six years ago a special development program for PMT candidates for the CTA project. Now, PMTs with exceptional good parameters became available.

We measured a very high QE of up to 38 % for the latest PMTs with a super bialkali photocathode. This is an improvement of around 10 % compared to the generation of PMTs ten years ago. Together with a collection efficiency of > 95 % for wavelengths above 400 nm this results in a photon detection efficiency of up to 36 %.

For the evaluation of PMTs the sensitivity for single photoelectrons is a real advantage. For this purpose, a special low-noise setup was optimized. With several measurements, the gain dependence was tested and the excess noise factor was evaluated. All tested PMTs show an exceptional good noise performance.

In the terms of time resolution the latest ET Enterprises PMTs fulfill the CTA specifications with a pulse width of 2.5 ns and a TTS of 1.5 ns. The Hamamatsu PMTs, that meanwhile became a commercial product, have slightly higher values with a pulse width of 3.2 ns and a TTS of 2.3 ns. Concerning the afterpulse probability, the Hamamatsu PMTs show a very low afterpulsing ≤ 0.02 % for a threshold of 4ph.e. The ET Enterprises PMTs have a ten times higher afterpulse probability. This issue will be solved by ET Enterprises in the next iteration of PMTs where all the best features of their development will be merged. It is planned to evaluate a batch of test PMTs next year. If ET Enterprises will succeed, their PMTs will be the best worldwide.

The second part of this thesis was dedicated to the upgrade of the MAGIC telescope's LIDAR system. For this purpose, a new detector together with a separate HV supply and faster readout electronics were custom designed. The installation on the MAGIC site on La Palma followed in late November 2015. During first test operations the system was working accurately. Also during bad weather conditions with high humidity, the detector and HV supply showed a stable performance. This increases the total availability of the LIDAR system and ensures a more stable operation.

Also the analysis software was adapted to the new hardware components and transmission profiles of cloud layers have been analyzed successfully. These first data were recorded during moon time and are affected by a high dark rate. Anyhow, they show results with reasonable accuracy. The performance of the new system will increase for operations during dark nights with lower background illumination. For this case the analysis software still has to prove its reliability. Thus, there is some space for further optimizations.

Besides the detector upgrade also a new transmitter module was designed. It consists of a biaxial adjustable base plate with a $20\times$ beam expander and a 532 nm frequency doubled

4. Conclusion and Outlook

Nd:YAG laser with a pulse energy of 25 μJ . The new laser is five times stronger than the current one. During first tests in the laboratory, the spot profile of the laser showed an additional artifact, which is detrimental for our measurements. Thus, the laser was sent back to the manufacturer for a new calibration and is not yet installed on La Palma. The new transmitter module is designed to extend the range of the LIDAR system to maintain the necessary altitude range for high zenith angle observations. After the successful tests of the new detector during moon time it is also supposed to handle the higher light intensities of the stronger laser. Further tests on La Palma are scheduled for spring 2016.

A. Appendix

A.1. CCD Camera Calibration

Low level light emission can be measured using high sensitive CCD cameras. During this thesis a Andor Clara series interline CCD camera was used together with a Navitar DO-1795 lens system. For a quantitative analysis of the recorded images a calibration of the camera is necessary. As a reference detector for the calibration a PMT was used.

At the beginning the transmission of the used camera optics was measured with the quantum efficiency measurement device (see Sec. 2.4). The light flux was measured with a PIN diode. Afterwards the camera optics was inserted in the setup and the light flux after the lens system was measured again. The results and the calculated transmission of the lens is shown in Fig. A.1. The transmission was evaluated in the range between 200 nm and 800 nm. For the first 100 nm of the measurement the PIN current was very small and causes large uncertainties. Thus, the calculated transmission is not very reliable in the range between 200 nm and 300 nm and it can be assumed that the lens transmission has a cutoff at about 350 nm.

The readout noise of a CCD camera is determined by three values: the dark current, the base level and the readout noise. The dark current of the Clara CCD camera is specified with less than 1 electron per pixel per second and neglected in our measurements. The base level is a constant value caused by a electronic DC offset in the CCD readout. The readout noise is dependent on the readout rate and the cooling of the CCD chip. For a very low noise we use a readout rate of 1 MHz and a temperature of -45°C for all our measurements. To evaluate the noise performance the Clara camera was put into a dark box and pictures with exposure times between 1 min and 60 min were taken. To obtain the noise characteristics the number of counts in each picture was plotted against the time in

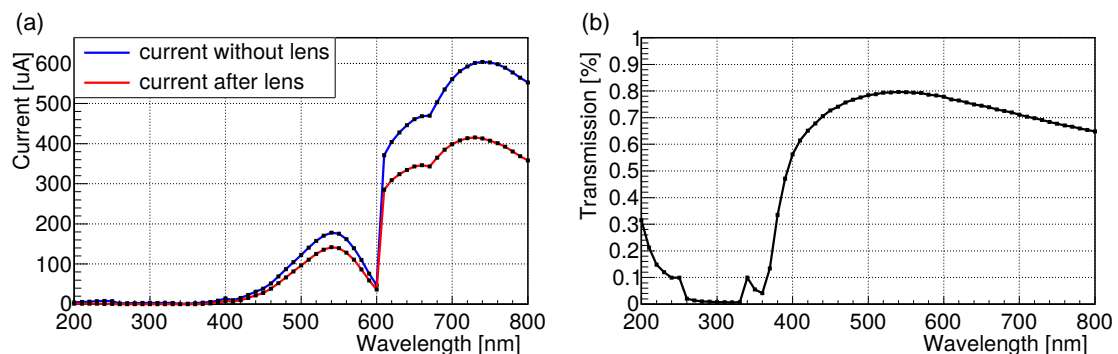


Figure A.1.: (a) Current measured with the PIN diode directly and after the lens. (b) Calculated transmission of the lens.

Parameter	Data Sheet	Measurement
Base Level [ADCounts/pixel]	520	531 ± 20
Readout Noise [ADCounts/pixel]	5.6	23.3 ± 0.7

Table A.1.: Results of the Clara calibration. The second column shows the specifications provided by the manufacturer on the user manual. The third column contains the results of our own measurements.

Fig. A.2(a) the extracted parameters are shown in Tab. A.1. For the base level a good agreement with the value data sheet is obtained. The readout noise of our measurement is a factor 4.1 larger than expected.

Another important number is the conversion factor from A/D Counts of the CCD chip to photoelectrons. To measure this factor we used a 405 nm pulsed laser source with a frequency of 10 kHz. The light intensity was calibrated to an average of 10 ph.e. per pulse using the Hamamatsu PMT ZQ 9652 described in Sec. 2.3. The number of photoelectrons depending on the exposure time is determined by the following equation:

$$N_{\text{ph.e}} = 10 \text{ ph.e.} \cdot 10 \text{ kHz} \cdot t \quad (\text{A.1})$$

Now we can calculate the number of expected AD Counts measured by the Clara CCD camera during the exposure time t :

$$N_{\text{CCD}}(t) = \alpha \cdot \frac{d_{\text{PMT}}}{d_{\text{Lens}}} \cdot \tau_{\text{Lens}} \cdot \frac{\text{QE}_{\text{CCD}}}{\text{QE}_{\text{PMT}}} \cdot N_{\text{ph.e}}(t) \quad (\text{A.2})$$

α is the CCD conversion factor, d_{PMT} is the photocathode diameter of the PMT, d_{Lens} is the diameter of the lens, τ_{Lens} is the lens transmission, QE_{CCD} is the quantum efficiency of the CCD and QE_{PMT} is the quantum efficiency of the PMT. If we compare this calculation to our measured values (shown in Fig. A.2(b)) we obtain a factor of 1.4 difference. This deviation can be caused by a difference in the CCD conversion factor or the stated quantum efficiency in the data sheet.

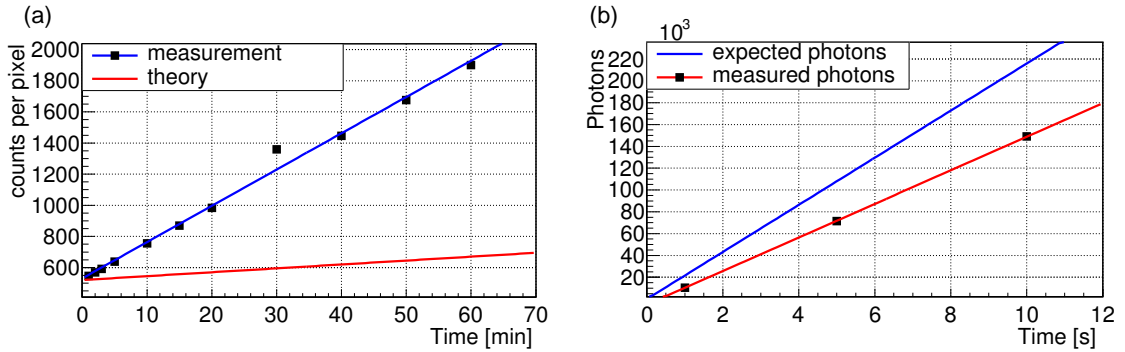


Figure A.2.: Calibration of the Clara CCD Camera. (a) Number of counts in the CCD image acquired in a dark box. (b) Detected and expected number of photons using a calibrated light source.

A.2. Source Code C++

A.2.1. LIDAR Background

```

0 // -----
1 // -----  L I D A R  m e a s u r e m e n t  p r o c e d u r e
   // -----
2 //
3 // -----  Background Rate and Single ph.e Charge  -----
4 // -----
5 /*
6 -----
7 based on: 4450 series software driver example (c) Spectrum GmbH,10/2008
8 -----
9 */
10 // ----- standard c include files -----
11
12 #include <stdio.h>
13 #include <stdlib.h>
14 #include <conio.h>
15 #include <time.h>
16 #include <math.h>
17 #include <string>
18 #include <fstream>
19 #include <iomanip>
20 #include <iostream>
21 #include <windows.h>
22 using namespace std;
23
24 // ----- include standard driver header from libraries -----
25
26 #include "../c_header/dlltyp.h"
27 #include "../c_header/regs.h"
28 #include "../c_header/spcerr.h"
29 #include "../c_header/spcm_drv.h"
30
31 // ----- include of common libraries -----
32
33 #include "../common/ostools/spcm_oswrap.h"
34 #include "../common/ostools/spcm_ostools.h"
35
36 // ----- set defaults for the measurement -----
37
38 #define shots_d 500 // Nr. of LASER shots
39 #define range_d 500 // measurement range in +- mV
40 #define memsize_d 196608 // memory depth for FADC
41 #define pretrig_d 1024 // memory depth before trigger
42
43 // -----
44 // ----- M A I N  D A T A  A C C U I S I T I O N  P R O C E S S -----
45 // -----

```

A. Appendix

```
46
47 int main()
48 {
49     // -----
50     // -----  P R E P A R I N G   T H E   V A R I A B L E S   -----
51     // -----
52     drv_handle  hCard;
53     int32       lCardType, lSerialNumber, lFncType;
54     char        szErrorTextBuffer[ERRORTXTLEN];
55     uint32      dwError;
56     int32       lStatus, lAvailUser, lPCPos;
57     uint64      qwTotalMem = 0;
58     uint64      qwToTransfer = MEGAB(64);
59
60     // ----- settings for the standard single recording mode -----
61
62     int32 shots = shots_d;
63     int32 range = range_d;
64     int32 memsize_aq = 2 * memsize_d;
65     int32 memsize = memsize_d;
66     int32 pretrig = pretrig_d;
67     int32 posttrig = memsize_d - pretrig_d;
68
69     // ----- variables for the conversion to voltage values -----
70
71     double per_bit = -range / (pow(2, 13)); // mV per ADC bit
72
73     // ----- allocate memory for temporary data storage -----
74
75     int16* DataTemp = new int16[memsize_aq];
76
77     // ----- allocate memory for subtracted data storage -----
78
79     ptr16*   DataRaw;
80     DataRaw = (ptr16*) malloc(shots * sizeof(ptr16));
81     for (int s = 0; s < shots; s++)
82     {
83         DataRaw[s] = (ptr16) malloc(memsize * sizeof(int16));
84     }
85
86     // -----
87     // -----  P R E P A R I N G   T H E   F A D C   C A R D   -----
88     // -----
89
90     // ----- open card -----
91
92     hCard = spcm_hOpen("/dev/spcm0");
93     if (!hCard)
94     {
95         printf("no card found...\n");
96         return 1;
97     }
98 }
```

```
97     }
98
99     // ----- read type, sn, function and check for A/D card -----
100
101     spcm_dwGetParam_i32(hCard, SPC_PCITYP, &lCardType);
102     spcm_dwGetParam_i32(hCard, SPC_PCISERIALNO, &lSerialNumber);
103     spcm_dwGetParam_i32(hCard, SPC_FNCTYPE, &lFncType);
104
105     // ----- setup FADC card for recording -----
106
107     spcm_dwSetParam_i32(hCard, SPC_CARDMODE, SPC_REC_STD_SINGLE);
108         // set the standard single recording mode
109     spcm_dwSetParam_i32(hCard, SPC_CHENABLE, 1 | 2);
110         // 2 channels enabled
111     spcm_dwSetParam_i32(hCard, SPC_PATH0, 0);
112         // set up channel0 to input path 0 (50 Ohm termination)
113     spcm_dwSetParam_i32(hCard, SPC_PATH1, 0);
114         // set up channel1 to input path 0 (50 Ohm termination)
115     spcm_dwSetParam_i64(hCard, SPC_SAMPLERATE, MEGA(500));
116         // set the samplerate to 500 MHz
117     spcm_dwSetParam_i32(hCard, SPC_50OHM0, 1);
118         // set up channel0 to 50 Ohm termination
119     spcm_dwSetParam_i32(hCard, SPC_50OHM1, 1);
120         // set up channel1 to 50 Ohm termination
121     spcm_dwSetParam_i32(hCard, SPC_MEMSIZE, memsize_aq);
122         // set up the recording length
123     spcm_dwSetParam_i32(hCard, SPC_PRETRIGGER, pretrig);
124         // events recorded before trigger
125     spcm_dwSetParam_i32(hCard, SPC_POSTTRIGGER, posttrig);
126         // events recorded after trigger
127     spcm_dwSetParam_i32(hCard, SPC_TIMEOUT, 5000);
128         // timeout 5s
129     spcm_dwSetParam_i32(hCard, SPC_TRIG_ORMASK, SPC_TMASK_SOFTWARE);
130         // trigger set to software
131     spcm_dwSetParam_i32(hCard, SPC_TRIG_ANDMASK, 0);
132         // no trigger mask
133     spcm_dwSetParam_i32(hCard, SPC_CLOCKMODE, SPC_CM_INTPLL);
134         // clock mode internal
135     spcm_dwSetParam_i32(hCard, SPC_CLOCKOUT, 0);
136         // no clock output
137
138     // ----- start looping through the laser shots -----
139
140     for (int s = 0; s < shots; s++)
141     {
142         // start everything
143
144         dwError = spcm_dwSetParam_i32(hCard, SPC_M2CMD, M2CMD_CARD_START
145             | M2CMD_CARD_ENABLETRIGGER | M2CMD_CARD_WAITREADY);
146
147         // check for errors
```

A. Appendix

```
132     if (dwError != ERR_OK)
133     {
134         spcm_dwGetErrorInfo_i32(hCard, NULL, NULL, szErrorTextBuffer);
135         printf("%s\n", szErrorTextBuffer);
136         spcm_vClose(hCard);
137         getchar();
138         return 0;
139     }
140
141     // readout the data
142     spcm_dwDefTransfer_i64(hCard, SPCM.BUF_DATA, SPCM.DIR_CARDTOPC,
143         0, DataTemp, 0, 2 * memsize_aq);
144
145     spcm_dwSetParam_i32(hCard, SPC.M2CMD, M2CMD.DATA.STARTDMA |
146         M2CMD.DATA.WAITDMA);
147
148     // subtract data from CH1 and CH2 of the differential amplifier
149     for (int i = 0; i < memsize_aq; i += 2)
150     {
151         DataRaw[s][i / 2] = DataTemp[i+1] - DataTemp[i];
152     }
153     spcm_vClose(hCard);
154
155     // -----
156     // -----          P R O C E S S I N G   D A T A          -----
157     // -----
158     // ----- photon histogramm -----
159
160     int photons =0;           // total number of detected
161     photons                                     photons
162     int phe_sample_size = 0; // number of photons in sample
163     for charge calculation
164     double pedestal = 0;     // pedestal before every single
165     photon
166     double phe_treshold = 2.0; // treshold for phe mV
167     double phe_charge_treshold = 3.0; // treshold for phe counting and
168     phe charge measurement in mV
169     double phe_charge = 0;   // for storing single phe charge
170     double phe_charge_avg = 0; // for storing average single
171     phe charge
172
173     const int phe_histogram_bins = 200;
174     double phe_histogram[phe_histogram_bins] = { 0 }; // for storing
175     charge histogram
176     double phe_charge_max = 100.0;
177     double phe_charge_bin = phe_charge_max/phe_histogram_bins;
178     double Vxp;
179     double V;
180     double Vpx;
```

```

175
176 int ped_offset [2] = {25, 5};           // defining the region before
      single photon for pedestal
177 double charge_limits [2] = {5, 100};   // defining the limits for
      charge calculation
178
179 // ----- determining single phe charge (histogram) -----
180
181 for (int s = 0; s < shots; s++)
182 {
183     for (int i = ped_offset [0] + 100; i < memsize - 100; i++)
184     {
185         V = (double(DataRaw[s][i])) * per_bit;
      // convert measured value to mV
186         Vpx = (double(DataRaw[s][i + 1])) * per_bit;
187         if (V >= phe_treshold && Vpx < V)
188         {
189             Vxp = (double(DataRaw[s][i - 1])) * per_bit;
190             for (int j = i - ped_offset [0]; j < i - ped_offset [1]; j++)
      // calculate pedestal before single phe event
191             {
192                 pedestal += (double(DataRaw[s][j])) * per_bit;
193             }
194             pedestal /= ( ped_offset [0] - ped_offset [1] );
195             phe_charge = Vxp + V + Vpx - (pedestal * 3);
196             if (phe_charge > phe_charge_treshold)
197             {
198                 photons++; // increase number of photons
199             }
200             if (phe_charge > charge_limits [0] && phe_charge <
      charge_limits [1])
201             {
202                 phe_charge_avg += phe_charge;
203                 phe_sample_size++;
204             }
205             if (phe_charge >= 0 && phe_charge < phe_charge_max)
206             {
207                 phe_histogram [int(phe_charge/phe_charge_bin)]++;
      // fill charge histogram
208             }
209         }
210     }
211 }
212
213 // ----- calculate average single phe charge -----
214
215 if (phe_sample_size > 0)
216 {
217     phe_charge_avg /= phe_sample_size;
218 }
219

```

A. Appendix

```
220 // ----- writing photon rate to file -----
221
222 ofstream f_photon_rate;
223 f_photon_rate.open("L:\photon_rate.dat", ios::trunc);
224 f_photon_rate << photons << endl;
225 f_photon_rate.close();
226
227 // ----- writing single photon charge to file -----
228
229 ofstream f_phe_charge;
230 f_phe_charge.open("L:\phe_charge.dat", ios::trunc);
231 f_phe_charge << phe_charge_avg << endl;
232 f_phe_charge.close();
233
234 // ----- writing to phe charge log file -----
235
236 ofstream phe_charge_log;
237 phe_charge_log.open("L:\phe_charge_log.dat", ios::trunc);
238 if (phe_charge_log.is_open()) {
239     for (int i = 0; i < phe_charge_max; ++i)
240     {
241         phe_charge_log << i*phe_charge_bin << "\t" << phe_histogram[i]
242             << endl;
243     }
244     phe_charge_log.close();
245 }
246
247 // ----- commandline output -----
248
249 printf("%f%f\n", double(photons) / double(shots), phe_charge_avg);
250 return 0;
251 }
```

A.2.2. High Voltage Control

```

0 // -----
1 // ----- L I D A R   m e a s u r e m e n t   p r o c e d u r e -----
2 // -----
3 //
4 // -----   High Voltage Control   -----
5 // -----
6
7 // ----- standard c include files -----
8
9 #include <stdio.h>
10 #include <stdlib.h>
11 #include <conio.h>
12 #include <time.h>
13 #include <math.h>
14 #include <string>
15 #include <fstream>
16 #include <iomanip>
17 #include <iostream>
18 #include <windows.h>
19 using namespace std;
20
21 // ----- include standard driver header from QLIB library -----
22
23 #include "../Header/qlib.h"
24
25 // ----- pin configuration of the TTL I/O channels -----
26
27 int DOUT = 7;           // output channel
28 int Channel1 = 24;     // DAC MCP4822
29 int Channel2 = 25;     // DAC MCP4922
30 int Channel3 = 26;     // ADC MAX186
31 int SerialClock = 27;  // clock line
32 int SDI = 28;          // data channel
33 int Switch1 = 29;      // iseg 600 V
34 int Switch2 = 30;      // EMC0 8kV
35
36
37 // ----- command for selecting each TTL I/O channel -----
38
39 int readCH0 [] = { 1, 0, 0, 0, 1, 1, 1, 0 };
40 int readCH1 [] = { 1, 1, 0, 0, 1, 1, 1, 0 };
41 int readCH2 [] = { 1, 0, 0, 1, 1, 1, 1, 0 };
42 int readCH3 [] = { 1, 1, 0, 1, 1, 1, 1, 0 };
43 int readCH4 [] = { 1, 1, 0, 1, 1, 1, 1, 0 };
44 int readCH5 [] = { 1, 0, 1, 0, 1, 1, 1, 0 };
45 int readCH6 [] = { 1, 1, 1, 0, 1, 1, 1, 0 };
46 int readCH7 [] = { 1, 0, 1, 1, 1, 1, 1, 0 };
47 int readCH8 [] = { 1, 1, 1, 1, 1, 1, 1, 0 };
48

```

A. Appendix

```
49
50 // ----- define a function to send a SPI commend to set a voltage -----
51
52 void writeSPI(ULONG Handle, int select, int length, int *data)
53 {
54     // set clock line to 0
55     QAPIExtWriteDO1(Handle, SerialClock, 0, 0);
56     // activate device via channel select line
57     QAPIExtWriteDO1(Handle, select, 0, 0);
58
59     // send command
60     for (int i = 0; i < length; ++i)
61     {
62         // transmit data via SDI line
63         QAPIExtWriteDO1(Handle, SDI, data[i], 0);
64         Sleep(1);
65         // switch serial clock to 1
66         QAPIExtWriteDO1(Handle, SerialClock, 1, 0);
67         Sleep(1);
68         // switch serial clock to 0
69         QAPIExtWriteDO1(Handle, SerialClock, 0, 0);
70     }
71     Sleep(100);
72     // deactivate device after transmission
73     QAPIExtWriteDO1(Handle, select, 1, 0);
74 }
75
76 // ----- define function to transform integer voltage into binary
77 // format -----
78
79 void setVoltage(int value, int* data)
80 {
81     for (int i = 0; i < 12; i++)
82     {
83         data[15 - i] = value & (1 << i) ? 1 : 0;
84     }
85 }
86
87 // ----- define function to calculate the control voltage for selected
88 // high voltage -----
89
90 void setVoltage8kV(double value, int* data)
91 {
92     double voltage;
93     voltage = ((value / 8000.0) * 4096) + 0.5; //mV
94     int V_set = (int)voltage;
95
96     for (int i = 0; i < 12; i++)
97     {
98         data[15 - i] = V_set & (1 << i) ? 1 : 0;
99     }
100 }
```

```

98 }
99
100 // -----
101 // -----   S T A R T   M A I N   C O N T R O L   P R O C E S S   -----
102 // -----
103
104 int main(int argc, char* argv[])
105 {
106     // -----
107     // -----   P R E P A R I N G   T H E   V A R I A B L E S   -----
108     // -----
109
110     int on = atoi(argv[1]);
111     double Voltage = atof(argv[2]);
112     ULONG nHandle;
113     ULONG nResult;
114
115     // -----
116     // -----   P R E P A R I N G   T H E   T T L   I/O   C A R D   -----
117     // -----
118
119     // ----- open card and error handling -----
120
121     if ((nHandle = QAPIExtOpenCard(56, 0L)) == 0L)
122     {
123         printf("Card not open");
124     }
125
126     // ----- define input channels 0-15 -----
127
128     nResult = QAPIExtSpecial(nHandle, JOB_PCITTL32_IOMODE0_7, 0, 0);
129     nResult = QAPIExtSpecial(nHandle, JOB_PCITTL32_IOMODE8_15, 0, 0);
130
131     // ----- define output channels 24-31 -----
132
133     nResult = QAPIExtSpecial(nHandle, JOB_PCITTL32_IOMODE24_31, 1, 0);
134
135     // ----- switch of the channel select lines -----
136
137     QAPIExtWriteDO1(nHandle, Channel1, 1, 0);
138     QAPIExtWriteDO1(nHandle, Channel2, 1, 0);
139     QAPIExtWriteDO1(nHandle, Channel3, 1, 0);
140
141
142     // ----- set reference voltage via MCP4822 -----
143
144     int Ref2[] = { 1, 0, 0, 1, 0, 1, 1, 1, 0, 0, 0, 0, 0, 0, 0, 0 }; // DAC B
145     setVoltage(2500, Ref2); // DAC B 2500mV
146
147
148     // ----- switch on reference voltage -----

```

A. Appendix

```
149
150 writeSPI(nHandle, Channel1, 16, Ref2);
151
152 // ----- set controll voltage for DC/DC converter via MCP4822 -----
153
154 int voltage2 [] = { 1, 0, 0, 1, 0,0,0,0, 0,0,0,0, 0,0,0,0 };
155 // DAC B
156 setVoltage8kV(Voltage, voltage2); // DAC B 4000V
157
158 // ----- switch on control voltage -----
159
160 writeSPI(nHandle, Channel2, 16, voltage2);
161
162 // ----- safety check to make sure communication is switched off
163 // -----
164
165 if (on == 1) QAPIExtWriteDO1(nHandle, Switch2, 1, 0);
166 else QAPIExtWriteDO1(nHandle, Switch2, 0, 0);
167 }
```

A.2.3. Voltage Monitoring

```

1 //-----
2 //-----  L I D A R  m e a s u r e m e n t  p r o c e d u r e  -----
3 //
4 // -----  Voltage Monitoring  -----
5 //-----
6
7 // ----- standard c include files -----
8
9 #include <stdio.h>
10 #include <stdlib.h>
11 #include <conio.h>
12 #include <time.h>
13 #include <math.h>
14 #include <string>
15 #include <fstream>
16 #include <iomanip>
17 #include <iostream>
18 #include <windows.h>
19 using namespace std;
20
21 // ----- include standard driver header from QLIB library -----
22
23 #include "../Header/qlib.h"
24
25
26 // ----- pin configuration of the TTL I/O channels -----
27
28 int DOUT = 7;      // output channel
29 int Channel1 = 24; // DAC MCP4822
30 int Channel2 = 25; // DAC MCP4922
31 int Channel3 = 26; // ADC MAX186
32 int SerialClock = 27; // clock line
33 int SDI = 28;      // data channel
34 int Switch1 = 29;  // iseg 600 V
35 int Switch2 = 30; // EMC0 8kV
36
37 // ----- command for selecting each TTL I/O channel -----
38
39 int readCH0 [] = { 1, 0, 0, 0, 1, 1, 1, 0 };
40 int readCH1 [] = { 1, 1, 0, 0, 1, 1, 1, 0 };
41 int readCH2 [] = { 1, 0, 0, 1, 1, 1, 1, 0 };
42 int readCH3 [] = { 1, 1, 0, 1, 1, 1, 1, 0 };
43 int readCH4 [] = { 1, 1, 0, 1, 1, 1, 1, 0 };
44 int readCH5 [] = { 1, 0, 1, 0, 1, 1, 1, 0 };
45 int readCH6 [] = { 1, 1, 1, 0, 1, 1, 1, 0 };
46 int readCH7 [] = { 1, 0, 1, 1, 1, 1, 1, 0 };
47 int readCH8 [] = { 1, 1, 1, 1, 1, 1, 1, 0 };
48
49 // ----- define a function to read the SPI signal send from device

```

```

50
51 void readSPI(ULONG Handle, int *read, int length, int *data)
52 {
53     // activate ADC via channel select line
54     QAPIExtWriteDO1(Handle, Channel3, 0, 0);
55     // set clock line to 0
56     QAPIExtWriteDO1(Handle, SerialClock, 0, 0);
57     Sleep(10);
58
59     // select channel of the ADC for readout
60     for (int i = 0; i < 8; i++)
61     {
62         // transmit data via SDI line
63         QAPIExtWriteDO1(Handle, SDI, read[i], 0);
64         Sleep(1)
65         // switch serial clock to 1
66         QAPIExtWriteDO1(Handle, SerialClock, 1, 0);
67         Sleep(1)
68         // switch serial clock to 0
69         QAPIExtWriteDO1(Handle, SerialClock, 0, 0);
70     }
71     Sleep(2);
72
73     // read data transmitted from ADC
74     for (int i = 0; i < 12; i++)
75     {
76         // switch serial clock to 1
77         QAPIExtWriteDO1(Handle, SerialClock, 1, 0);
78         Sleep(1);
79         // switch serial clock to
80         QAPIExtWriteDO1(Handle, SerialClock, 0, 0);
81         // read data from DOUT line
82         data[i] = QAPIExtReadDI1(Handle, DOUT, 0);
83         Sleep(1);
84     }
85
86     // deactivate device after communication
87     QAPIExtWriteDO1(Handle, Channel3, 1, 0);
88     Sleep(10);
89 }
90
91 // ----- define function to transform binary data to integer value
92     -----
93 double getVoltage(int* data)
94 {
95     int value = 0;
96     for (int i = 0; i < 12; i++)
97     {
98         value += data[i] * (1 << (11 - i));

```

```
99     }
100     return value;
101 }
102
103 // ----- define function to calculate bias voltage output -----
104
105 double getVoltage600V(int* data)
106 {
107     int value = 0;
108     for (int i = 0; i < 12; i++)
109     {
110         value += data[i] * (1 << (11 - i));
111     }
112     double voltage;
113     voltage = (value / 2500.0) * 600.0;
114     return voltage;
115 }
116
117
118 // ----- define function to calculate high voltage output -----
119
120 double getVoltage8kVin(int* data)
121 {
122     int value = 0;
123     for (int i = 0; i < 12; i++)
124     {
125         value += data[i] * (1 << (11 - i));
126     }
127     double voltage;
128     voltage = (value / 4000.0) * 8000.0;
129     return voltage;
130 }
131
132 // -----
133 // -----   S T A R T   M A I N   C O N T R O L   P R O C E S S   -----
134 // -----
135
136 int main()
137 {
138     // -----
139     // -----   P R E P A R I N G   T H E   V A R I A B L E S   -----
140     // -----
141
142     ULONG nHandle;
143     ULONG nResult;
144
145     // -----
146     // -----   P R E P A R I N G   T H E   T T L   I/O   C A R D   -----
147     // -----
148
149     // ----- open card and error handling -----
```

```

150
151     if ((nHandle = QAPIExtOpenCard(56, 0L)) == 0L)
152     {
153         printf("Karte_konnte_nicht_geoeffnet_werden");
154         return 0;
155     }
156
157     // ----- define input channels 0-15 -----
158
159     nResult = QAPIExtSpecial(nHandle, JOB_PCITTL32_IOMODE0_7, 0, 0);
160     nResult = QAPIExtSpecial(nHandle, JOB_PCITTL32_IOMODE8_15, 0, 0);
161
162     // ----- define output channels 24-31 -----
163
164     nResult = QAPIExtSpecial(nHandle, JOB_PCITTL32_IOMODE24_31, 1, 0);
165
166     // ----- readout the voltage of all eight ADC channels -----
167
168     int read1 [] = { 0, 0, 0, 0, 0, 0, 0, 0, 0, 0, 0, 0, 0, 0 };
169     int read2 [] = { 0, 0, 0, 0, 0, 0, 0, 0, 0, 0, 0, 0, 0, 0 };
170     int read3 [] = { 0, 0, 0, 0, 0, 0, 0, 0, 0, 0, 0, 0, 0, 0 };
171     int read4 [] = { 0, 0, 0, 0, 0, 0, 0, 0, 0, 0, 0, 0, 0, 0 };
172     int read5 [] = { 0, 0, 0, 0, 0, 0, 0, 0, 0, 0, 0, 0, 0, 0 };
173     int read6 [] = { 0, 0, 0, 0, 0, 0, 0, 0, 0, 0, 0, 0, 0, 0 };
174     int read7 [] = { 0, 0, 0, 0, 0, 0, 0, 0, 0, 0, 0, 0, 0, 0 };
175     int read8 [] = { 0, 0, 0, 0, 0, 0, 0, 0, 0, 0, 0, 0, 0, 0 };
176
177     readSPI(nHandle, readCH0, 16, read1);
178     readSPI(nHandle, readCH1, 16, read2);
179     readSPI(nHandle, readCH2, 16, read3);
180     readSPI(nHandle, readCH3, 16, read4);
181     readSPI(nHandle, readCH4, 16, read5);
182     readSPI(nHandle, readCH5, 16, read6);
183     readSPI(nHandle, readCH6, 16, read7);
184     readSPI(nHandle, readCH7, 16, read8);
185
186     // ----- convert binary output values of the ADC into integer value
187     // [mV] -----
188
189     int Vout1 = 0;
190     int Vout2 = 0;
191     int Vout3 = 0;
192     int Vout4 = 0;
193     int Vout5 = 0;
194     int Vout6 = 0;
195     int Vout7 = 0;
196     int Vout8 = 0;
197
198     Vout1 = getVoltage(read1);
199     Vout2 = getVoltage(read2);
200     Vout3 = getVoltage(read3);

```

```
200     Vout4 = getVoltage(read4);
201     Vout5 = getVoltage(read5);
202     Vout6 = getVoltage(read6);
203     Vout7 = getVoltage(read7);
204     Vout8 = getVoltage(read8);
205
206     // ----- calculate voltage output of both DC/DC converters [V] -----
207
208     double Value1;
209     double Value2;
210     double Value3;
211
212     Value1 = getVoltage600V(read1);
213     Value2 = getVoltage600V(read2);
214     Value3 = getVoltage8kVin(read3);
215
216     // ----- print the values to command line for further processing
217     -----
218     printf("%f□%f□%f□\n", Value1, Value2, Value3);
219
220 }
```

A.3. Circuit Diagrams and Layouts

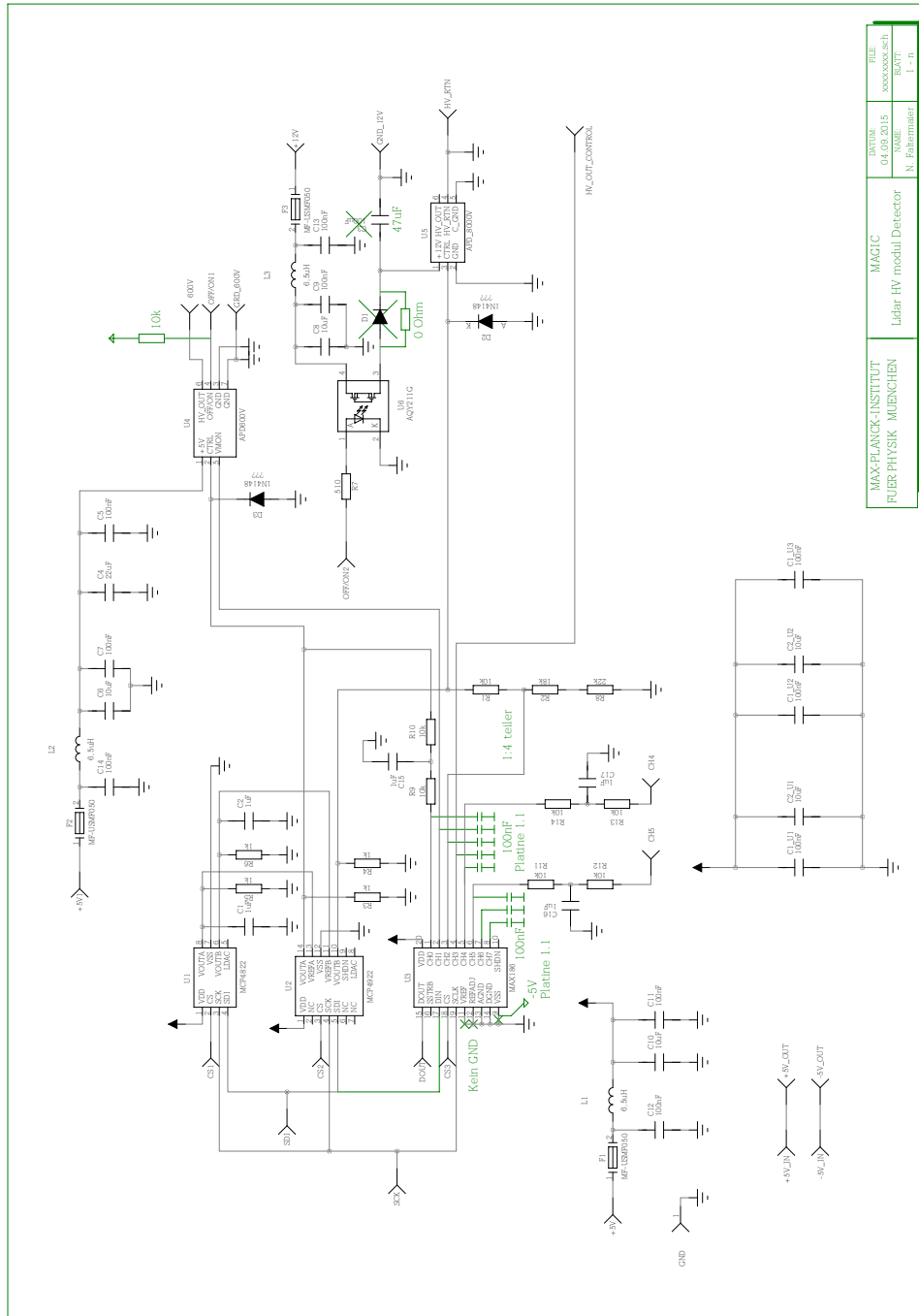


Figure A.3.: Wiring scheme of the HV module provided by Nicole Faltermaier (department of electronic engineering).

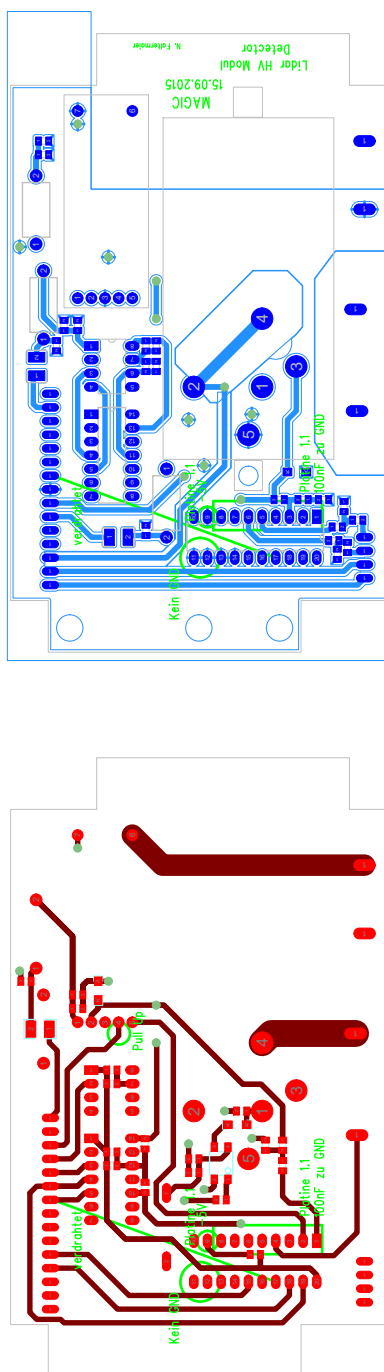


Figure A.4.: Printed circuit board layout of the HV module provided by Nicole Faltermaier (department of electronic engineering).

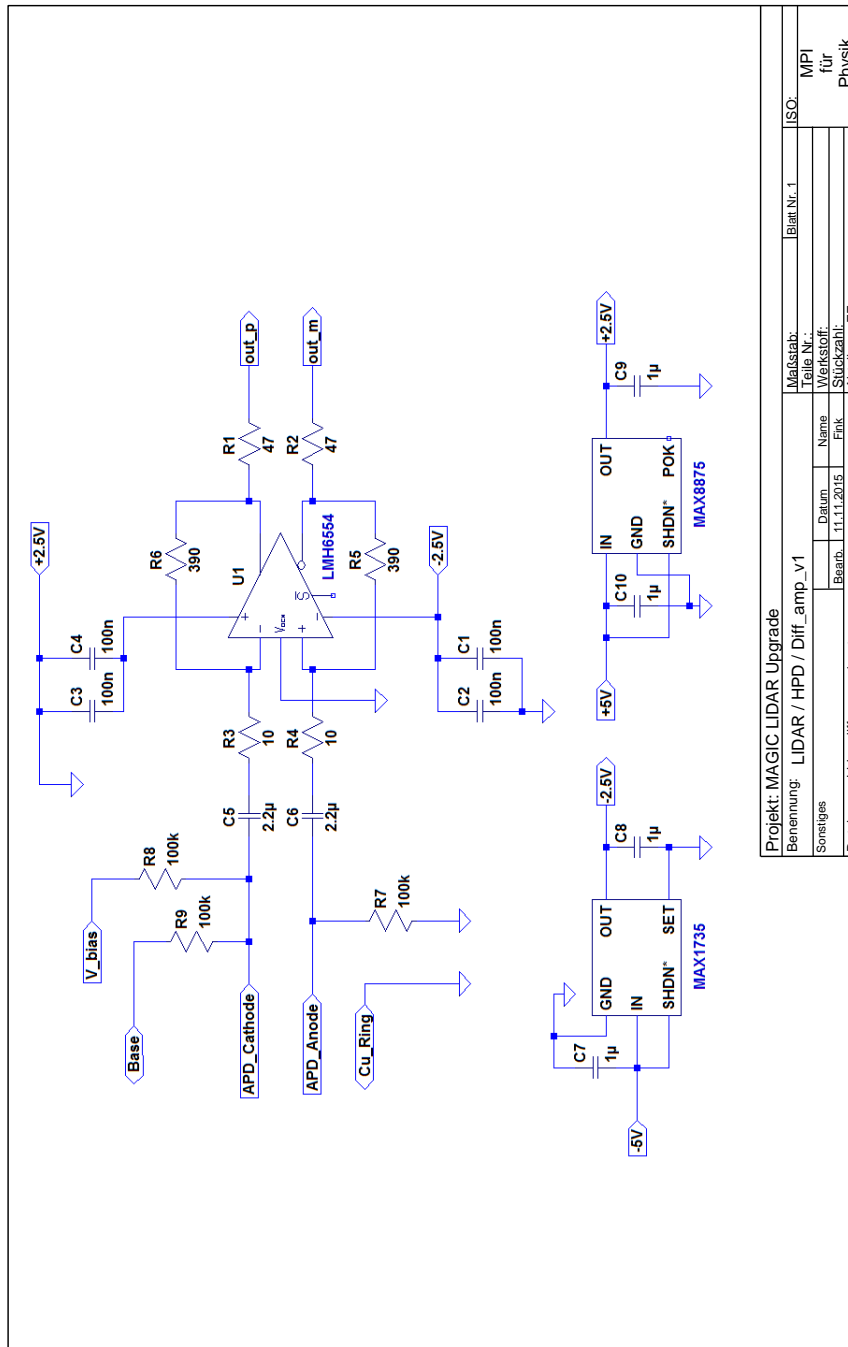


Figure A.5.: Wiring scheme of the differential amplifier provided by David Fink (department of electronic engineering).

B. Bibliography

- [1] H. Bartko, *Observation of Galactic Sources of Very High Energy Gamma-Rays with the MAGIC Telescope*. PhD thesis, Fakultät für Physik der Ludwigs-Maximilians-Universität München, December 2006. https://edoc.ub.uni-muenchen.de/6692/1/Bartko_Hendrik.pdf.
- [2] V. F. Hess, “Über Beobachtungen der durchdringenden Strahlung bei sieben Freibalohnfahrten,” *Physikalische Zeitschrift*, 1912. <http://www.mpi-hd.mpg.de/hfm/HESS/public/HessArticle.pdf>.
- [3] U. Menzel, “Monte Carlo studies of gamma-mimicking hadron background in Imaging Air Cherenkov Telescopes,” Master’s thesis, Max-Planck-Institut für Physik, August 2013.
- [4] W. F. Hanlon, “Spectrum of Cosmic Rays.” <http://www.physics.utah.edu/~whanlon/spectrum.html>.
- [5] “A Giant Hubble Mosaic of the Crab Nebula,” 2005. <http://hubblesite.org/newscenter/archive/releases/2005/37/image/a/>.
- [6] “Space Movie Reveals Shocking Secrets of the Crab Pulsar,” 2002. <http://hubblesite.org/newscenter/archive/releases/2002/24/image/a/>.
- [7] F. Schmidt, “Air Shower Simulation with CORSIKA.” <https://www.ikp.kit.edu/corsika/>.
- [8] P. A. Cherenkov, “Visible Radiation Produced by Electrons Moving on a Medium with Velocities Exceeding that of light,” *Phys. Rev.* 52, 378, June 1937.
- [9] A. M. Hillas, “Evolution of ground-based gamma-ray astronomy from the early days to the Cherenkov Telescope Array,” *Astroparticle Physics* 42, 2013. <http://www.sciencedirect.com/science/article/pii/S0927650512001326>.
- [10] “Picture of the MAGIC telescope,” 2009. https://magicold.mpp.mpg.de/gallery/pictures/tn/IMG_2520.JPG.html.
- [11] “The Gamma-ray Coordinates Network.” <http://gcn.gsfc.nasa.gov/>.
- [12] D. Nakajima *et al.*, “New Imaging Camera for the MAGIC-I Telescope,” *33er International Cosmic Ray Conference*, 2013. <http://www.cbpf.br/~icrc2013/papers/icrc2013-0787.pdf>.
- [13] “Design study of CTA.” <https://portal.cta-observatory.org/Pages/Home.aspx>.

- [14] B. S. Acharya *et al.*, “Introducing the CTA concept,” *Astroparticle Physics*, vol. 43, pp. 3 – 18, 2013. <https://portal.cta-observatory.org/Pages/CTA-Science.aspx>.
- [15] J. Hinton, S. Sarka, D. Torres, and J. Knapp, “Seeing the High-Energy Universe with the Cherenkov Telescope Array. The Science explored with the CTA.,” *Astroparticle Physics* 43, 2013. <https://portal.cta-observatory.org/Pages/CTA-Science.aspx>.
- [16] Particle Physics Research Center. <http://pprc.qmul.ac.uk/~still/wordpress/wp-content/uploads/2012/11/PH20-water-withboat-apr23.jpg>.
- [17] PHYS.ORG. <http://cdn.phys.org/newman/gfx/news/hires/2011/1-underwaterne.jpg>.
- [18] MAGIC coloboration. https://magicold.mpp.mpg.de/gallery/pictures/tn/IMG_9197.jpg.html.
- [19] V. K. Zworykin, G. Morton, and L. Malter, “The Secondary Emission Multiplier-A New Electronic Device ,” *IEEE*, 1936. <http://ieeexplore.ieee.org/stamp/stamp.jsp?tp=&arnumber=1686095>.
- [20] *Understanding Photomultipliers*. <http://www.et-enterprises.com/files/file/Understanding-photomultipliers.pdf>.
- [21] *Photomultiplier Tubes Basics and Application*. https://www.hamamatsu.com/resources/pdf/etd/PMT_handbook_v3aE.pdf.
- [22] S. Hunklinger, *Festkörperphysik*. No. ISBN 978-3-486-59045-6, Oldenbourg Wissenschaftsverlag GmbH, 2. Auflage ed., 2009.
- [23] M. L. Knötig, “Light Sensor Candidates for the Cherenkov Telescope Array,” Master’s thesis, Technische Universität München, April 2012.
- [24] *CM110 Compact 1/8 Meter Monochromator*. <http://www.spectralproducts.com/cm110>.
- [25] *Keithley Model 6487 Picoammeter*. <http://www.testequity.com/documents/pdf/keithley/manuals/6485-6487-m.pdf>.
- [26] PicoQuant, *Picosecond Pulsed Diode Laser Driver PDL 800-D*. <http://www.picoquant.com/images/uploads/downloads/pdl800-d.pdf>.
- [27] T. Toyama *et al.*, “Evaluation of the basic propertied of the novel 1.5 in. size PMTs from Hamamatsu Photonics and Electron Tubes Enterprises,” *Nuclear Instruments and Methods in Physics Research Section A: Accelerators, Spectrometers, Detectors and Associated Equipment*, vol. 787, no. 0, pp. 280 – 283, 2015. <http://www.sciencedirect.com/science/article/pii/S0168900214015265>.
- [28] Thorlabs. http://www.thorlabs.de/newgrouppage9.cfm?objectgroup_id=6271&pn=NE60B-A.

- [29] R. Mirzoyan, D. Müller, *et al.*, “Novel 1.5’ Size Exceptional PMTs for the CTA Project,” *Proceedings of Science*, 2015.
- [30] M. Kurz, “Precision Measurements of Ultra-fast Low Light Level Candidate Sensors for the CTA Project,” Master’s thesis, Technische Universität München, 2011.
- [31] R. Mirzoyan, “On the calibration accuracy of light sensors in atmospheric Cherenkov fluorescence and neutrino experiment,” *25th International Conference on Cosmic Rays, v.1-7*, 1997.
- [32] *Quick Start Guide Agilent 81110A 165/330 MHz*. <http://literature.cdn.keysight.com/litweb/pdf/81110-91020.pdf?id=1000000838-1:epsg:man>.
- [33] R. Mirzoyan *et al.*, “On the influence of afterpulsing in PMTs on the trigger threshold of multichannel light detectors in self-trigger mode,” *Nuclear Instruments and Methods in Physics Research Section A*, 1997. <http://www.sciencedirect.com/science/article/pii/S0168900296009643>.
- [34] Oxford Instruments Company, *ANDOR Ultra Sensitive Imaging Cameras*. http://www.andor.com/pdfs/literature/Andor_Clara_Flyer.pdf.
- [35] T. Maiman, “Stimulated Optical Emission,” *Nature*, 1960. <http://laserfest.org/lasers/history/paper-maiman.pdf>.
- [36] G. Fiocco and G. Grams, “Observation of the Aerosol Layer at 20 km by Optical Radar,” *Journal of the Atmospheric Sciences*, 1964. <http://journals.ametsoc.org/doi/pdf/10.1175/1520-0469%281964%29021%3C0323%3A00TALA%3E2.0.CO%3B2>.
- [37] U. Wandinger, *Introduction to Lidar*, vol. 102 of *Springer Series in Optical Sciences*. Springer New York, 2005.
- [38] C. Fruck, “A new LIDAR system for the MAGIC telescopes and site search instrumentation for CTA,” Master’s thesis, Max-Planck-Institut für Physik, February 2011.
- [39] “U.S Standart Atmosphere 1976,” 1976. <http://ntrs.nasa.gov/archive/nasa/casi.ntrs.nasa.gov/19770009539.pdf>.
- [40] “U.S. Standard Atmosphere Calculator.” <http://www.digitaldutch.com/atmoscalc/table.htm>.
- [41] K. Bernlöher, “Impact of atmospheric parameters on the atmospheric Cherenkov technique,” *Astroparticle Physics*, 1999. <http://arxiv.org/pdf/astro-ph/9908093.pdf>.
- [42] M. Fuchs, “Untersuchung der atmosphärischen Transmission mittels Pyroskop und Lidar zur Gamma-Astronomie mit dem MAGIC Cherenkov Teleskop auf La Palma,” Master’s thesis, Fachhochschule München, 2007.
- [43] P. Laven, “Mie Plot,” 2015. <http://www.philiplaven.com/mieplot.htm>.

B. Bibliography

- [44] “Instituto de Astrofísica de Canarias.” <http://www.iac.es/en.php?op1=2&lang=en>.
- [45] C. Fruck, *The Galactic Center resolved with MAGIC and a new technique for Atmospheric Calibration*. PhD thesis, Technische Universität München Fakultät für Physik, 2015. <http://mediatum.ub.tum.de/node?id=1237928>.
- [46] G. Lombardi, “El Roque de Los Muchachos Site characteristics III.” *Astronomy & Astrophysics*, 2013. <http://arxiv.org/abs/astro-ph/0702570>.
- [47] B. A. Laken, “Sahara dust over the Northern Atlantic,” 2013. <http://4.bp.blogspot.com/-zj0BW2VjWXE/UlvdjWwKKpI/AAAAAAAAAKo/kb9fNthlsRg/>.
- [48] “New Technology Mount NTM-500.” <http://www.astelco.com/html/products/ntm/ntm.htm>.
- [49] “iseg High Voltage.” <http://iseg-hv.com/en/products/detail/APS>.
- [50] “emco High Voltage Corporation.” <http://www.emcohighvoltage.com/regulated/cseries.php>.
- [51] Edmund Optics GmbH, *30mm Outer Diameter Burnished Steel Leaves Iris Diaphragm*. <http://www.edmundoptics.de/optomechanics/irises-apertures/iris-diaphragms/high-performance-standard-series-iris-diaphragms/64508/?site=DE&countryid=84s>.
- [52] Edmund Optics GmbH, *535nm Bandpassfilter*. <http://www.edmundoptics.de/optics/optical-filters/bandpass-filters/hard-coated-od4-10nm-bandpass-filters/65156/>.
- [53] Orito *et al.*, “Development of HPD Clusters for MAGIC-II,” *Proceedings of the 31st ICRC, Lodz*, 2009. <http://arxiv.org/pdf/0907.0865v1.pdf>.
- [54] Hamamatsu Photonics K.K., *PMT Handbook Chapter 11*. https://www.hamamatsu.com/resources/pdf/etd/PMT_handbook_v3aE-Chapter11.pdf.
- [55] Hamamatsu Photonics K.K., *Hamamatsu Final Test Sheet R9792-40*, 2009.
- [56] Texas Instruments, *LMH6554 2.8-GHz Ultra Linear Fully Differential Amplifier*, 2015. <http://www.ti.com/lit/ds/symlink/lmh6554.pdf>.
- [57] HORUS Laser, *532 nm sub-ns microchip lasers (HLX-G series)*, 2015. <http://www.horuslaser.com/products/hlx-g-series>.
- [58] Spectrum Systementwicklung Microelectronic GmbH, *Hardware Manual M4i.44xx-x8 A/D converter board for PCI Express bus*. http://spectrum-instrumentation.com/sites/default/files/download/m4i44_manual_english.pdf.
- [59] J. D. Klett, “Stable analytical inversion solution for processing lidar returns,” *Optical Society of America*, 1981.

C. Acknowledgment

This Master's thesis would not been possible without the support and help of many colleagues at the Max-Planck-Institute for Physics and the TU München. These last lines are dedicated to everyone who supported me during the time working on this thesis.

At first, I want to thank **Prof. Dr. Elisa Resconi** for accepting the responsibility for my thesis at the TU München. Her lectures about cosmic rays and neutrino astronomy gave a broad insight into current research on this topics and enlarged my understanding of neutrino oscillations.

My thanks go to **Prof. Masahiro Teshima** as head of the MAGIC Munich group for accepting me as Master student.

A special thank goes to my supervisor **Dr. Razmik Mirzoyan** who accepted the responsibility for my thesis at the Max-Planck-Institute for Physics. His impressive expertise on low-level light measurements was of great use during this work. He always had time for questions and to discuss technical issues of the LIDAR upgrade. Furthermore, he enabled a lot of travels to present my work on meetings and conferences like the MAGIC Software School in Lodz, the DPG 2015 in Wuppertal and the PISA conference on advanced detectors in Elba.

Many thanks go to **Dr. Christian Fruck** who is the responsible for the MAGIC LIDAR system. He spend a lot of time explaining many topics of atmospheric monitoring to me and guided me through the whole LIDAR upgrade. Finally, he helped me with the installation and tests of the new detector on La Palma.

Additionally, I want to thank my colleagues **Takeshi Toyama** for the introduction to PMT measurements and **Uta Menzel** who always had time to solve any computer and programming problems.

Lots of thanks go to the colleagues of the mechanical and electrical workshops who produced all hardware components upon our request. Many thanks go to **Nicole Faltermaier** for her patience designing and assembling the high voltage box. Also **David Fink** has to be mentioned who designed the amplifier of the detector and gave helpful advice for selecting electronic components.

I want to thank all other **members** of the MAGIC Munich group for their help with big and small issues, lots of interesting conversations and for creating such a nice working atmosphere.

Finally, many thanks go to my **family** and **friends** who believed in me during my whole studies and provided everything I needed.